Chapter 3
Modeling Mechanical Micro-instabilities in Biophysics and Materials Science

Andrea Cannizzo, Manon Benedito, Fabio Manca, and Stefano Giordano

Contents

A. Cannizzo · M. Benedito · S. Giordano (✉)
University of Lille, CNRS, Centrale Lille, University Polytechnique Hauts-de-France, UMR 8520 - IEMN - Institut d'Electronique de Microélectronique et de Nanotechnologie, Lille, France
e-mail: andreacannizzo1992@gmail.com; manon.benedito@junia.com; stefano.giordano@univ-lille.fr

F. Manca
Aix Marseille Université, CNRS, INSERM, Laboratoire Adhesion & Inflammation, Turing Centre for Living Systems, Marseille, France

R. Pisano (ed.), *Nanoscience & Nanotechnologies*, Nanotechnology in the Life Sciences, https://doi.org/10.1007/978-3-031-85122-3_3

Abstract From biophysics to materials science, mechanical micro-instabilities play a central role in a multitude of materials and structures (where we observe phenomena such as adhesion, fracture, friction, phase transformations, and so on). Although these systems are very different in length-scale, time-scale, and morphology, they are all composed of a number of units (subsystems) that exhibit two or more equilibrium states and can switch from one to another depending on operating conditions. Schematically, we can identify two main classes of micro-instabilities in these multistable systems. On the one hand, we may observe a bistable behavior between one ground state and one metastable state, being these two states different, yet mechanically resistant conformations. For instance, in this class can be inscribed conformational (folded to unfolded) transitions in polymers or macromolecules (mostly proteins) and martensitic phase transformations in metallic alloys and nanowires (pseudo-elasticity). On the other hand, the second class corresponds to transitions between unbroken and broken states of breakable units of the system. This process can be reversible, partly reversible, or irreversible according to the specific physical phenomenon investigated. Examples of this scheme include unzipping of DNA or RNA hairpins, denaturation of macromolecules, biological adhesion, peeling of films in nanotechnology, and fracture phenomena in mechanics of materials. In this review, we offer a description of phenomena related to these mechanical micro-instabilities, ranging from biophysics to materials science. After presenting an overview of typical examples in both contexts, physical-mathematical approaches suitable for modeling and predicting the behavior of these systems will be introduced. In order to consider both thermal and mechanical effects, they are based on the combination of statistical mechanics and micromechanics.

Keywords Statistical mechanics · Micromechanics · Adhesion · Friction · Force spectroscopy · Fracture mechanics · Spin variables · Phase transitions · Critical temperature · DNA · RNA · Proteins · Polymers · Macromolecules · Nanowires · Pseudo-elasticity

1 Introduction

Micro-instabilities play a very important role in several artificial and biological mechanical systems. The possibility of having transitions between different states of the system, induced by mechanical actions or thermal fluctuations, generates considerable complexity in system responses, characterized by thermomechanical coupling and strongly nonlinear behavior. On the one hand, concerning artificial systems, we can mention the peeling of a film from a substrate (Cortet et al. 2007; Xia et al. 2012; Dalbe et al. 2015; Maddalena et al. 2009; Puglisi et al. 2013; Das et al. 2013; Qian et al. 2017), the waves propagation in bistable lattices (Rafsanjani et al. 2015; Nadkarni et al. 2016; Frazier et al. 2017; Katz et al. 2018, 2019), the energy harvesting through multistable chains (Hwang et al. 2018; Harne et al. 2014a,b), the plasticity and hysteresis in phase transitions and martensitic

transformations of solids (Ericksen 1975; Müller et al. 1977; Fedelich et al. 1992; Truskinovsky et al. 2004; Puglisi et al. 2005; Puglisi 2006; Efendiev et al. 2010; Mielke et al. 2012; Benichou et al. 2013; Caruel et al. 2015, 2017), the cracks and dislocations nucleation and propagation in materials and alloys (Blumberg Selinger et al. 1991; Borja da Rocha et al. 2019, 2020; Brenner 1962; George et al. 2019; Miracle et al. 2017; Cantor et al. 2004; Otto et al. 2013; Gali et al. 2013), and the friction at the nanoscale (Gao et al. 2004; Urbakh et al. 2004; Vanossi et al. 2013; Vakis et al. 2018; Ternes et al. 2008; Szlufarska et al. 2008; Mo et al. 2009; Krylov et al. 2014; Manini et al. 2017; Popov 2010). On the other hand, micro-mechanical biological phenomena include the conformational transitions in polymeric and biopolymeric chains (Storm et al. 2003; Hoffmann et al. 2012; Dudko 2016; Hughes et al. 2016; Prados et al. 2013; Bonilla et al. 2015; De Tommasi et al. 2013; Manca et al. 2013a; Bleha et al. 2022, 2018), the attached and detached states of fibrils in cell adhesion (Bell 1978; Bell et al. 1984; Gumbiner 1996; Erdmann et al. 2007; Gao et al. 2011; Schwarz et al. 2013), the unzipping of macromolecular hairpins (Liphardt et al. 2001; Dudko et al. 2007; Mathé et al. 2004; Woodside et al. 2008; Manosas et al. 2017), the sarcomeres behavior in skeletal muscles (Huxley et al. 1971; Hill 1973; Epstein et al. 1998; Caruel et al. 2013, 2016, 2018, 2019), the denaturation or degradation of nucleic acids, polypeptide chains, or other polymers (Peyrard et al. 1989; Theodorakopoulos et al. 2004; Grinza et al. 2004; Peyrard 2004; Ivanov et al. 2004; Palmeri et al. 2008; Pupo et al. 2013; Perret et al. 2016, 2017; Buche et al. 2021), and the macromolecular or soft matter friction (Bormuth et al. 2009; Sahli et al. 2018; Sens 2020; Liamas et al. 2020). Moreover, it is also interesting to remark that friction is also at the basis of understanding the evolution of geophysical systems (Scholz 1998; Marone 1998; Daub et al. 2010; Amitrano et al. 1999) and plastic phenomena in solid materials, being able to control the nucleation of dislocations and fractures and to regulate the shear transformations and the ductile-to-brittle failure transition (Gerde et al. 2001; Kresse et al. 2004; Gimbert et al. 2013; Biscari et al. 2016; Karimi et al. 2019; Gorbushin et al. 2020).

In all these physical situations, we eventually find a multi-basin energy landscape, and the state of the system can be in stable or metastable configurations, identified by the wells of the energy function. As a matter of fact, these systems are constituted by a large number of units characterized by well-defined physical states. The transitions between these states or, equivalently, the explorations of the energy landscape govern the macroscopic behavior of the whole system and, in particular, its static and dynamic features. There are two important different classes of microinstabilities. In the first case, the intrinsic micro-instabilities may describe bistable (or multistable) units with transitions between one ground state and one (or more) metastable state(s) (e.g., for the conformational folded-to-unfolded transitions in macromolecules or martensitic phase changes in metallic alloys or also friction). These states represent different, yet mechanically resistant conformations. This case can be represented in a one-dimensional setting by introducing an effective double-well potential energy U, as shown in Fig. 3.1 (first panel). We observe that the choice of a simple one-dimensional system is aimed at a simple presentation of the idea. In other words, x represents an effective order parameter adopted to

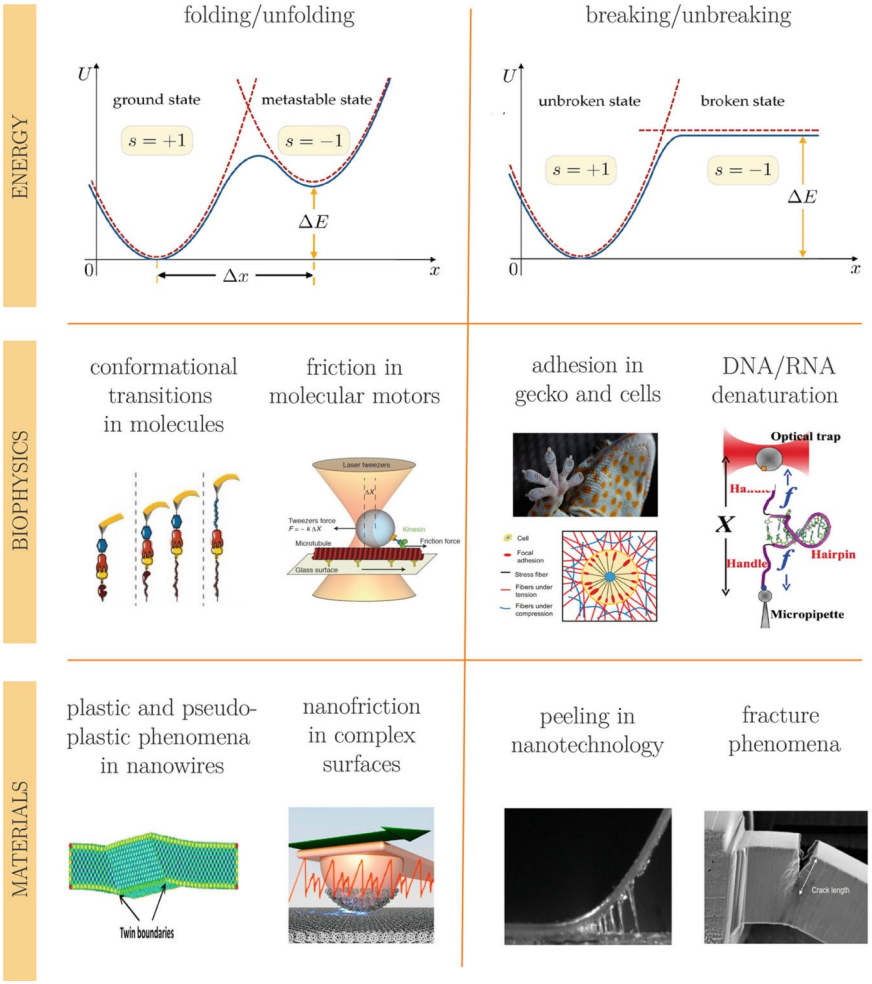

Fig. 3.1 In the first row one can find two different energy landscapes representing two classes of micro-instabilities: bistability between a folded (ground) state and an unfolded (metastable) state in the left panel, and transition between attached (unbroken) and detached (broken) states in the right panel. In the second and third rows, one finds some examples of microinstabilities in biophysics and materials science, corresponding to conformational transitions (bistability or multistability) in the first column, or rupture phenomena (deadhesion and decohesion) in the second one

describe the transition between the different wells, whereas all other variables can be considered to be minimized out. In the second case, the micro-instabilities can explain transitions between unbroken and broken states of the breakable units of the system (e.g., in the unzipping of hairpins, denaturation of macromolecules, fibrillar biological adhesion, peeling of films, and cracks propagation). This process can be reversible, partly reversible, or irreversible according to the specific physical

phenomenon. The one-dimensional energy considered in this second case is shown in Fig. 3.1 (second panel). Here, the unbroken configuration corresponds to a potential well, and the broken configuration corresponds to constant energy and zero force.

In the second and third rows of Fig. 3.1, one can find the most of previously mentioned examples following the classification between folding/unfolding or breaking/unbreaking energies (see the first row). The different situations have been subdivided between biophysics (second row) and materials science (third row), for the sake of clarity. It is interesting to note that there is a parallel between all the problems in biophysics and materials science. This similarity is at the basis of the development of mathematical models that are applicable indistinctly to both areas of research, as discussed in the following. In fact, the main goal is to develop models between physics and mechanics that are able to study state transitions (micro-instabilities) in all these biological and artificial systems in order to better understand the effects of temperature and external mechanical actions on their behavior.

Being the characteristic length Δx separating two stable positions of the order of few nanometers and the energies involved in chemical bonds of the order of tens of $K_B T$, the effect of temperature on these systems is non-negligible. As a matter of fact, the transitions between the states in all previous systems are strongly influenced by the thermal fluctuations, which can modify the probability of being in a given state or the transition rate between the neighboring energy wells. Therefore, the correct framework in which we can develop the theoretical modeling of these phenomena is the classical statistical mechanics. In particular, the systems exhibiting switching mechanisms between different energy basins and the systems characterized by breaking phenomena can be studied by means of the spin variables approach. This approach is based on the introduction of a series of discrete variables (similar to the spins used to deal with magnetic systems), which are able to identify the state associated with a given system unit (see the variable s in Fig. 3.1, first row). For example, the bistable potential energy of Fig. 3.1 (first panel) (continuous line) can be approximated by a biparabolic function (dashed lines) with the switching among the wells described by the spin variable. It means that, depending on the value of these discrete variables, the energy function may change its shape and, in particular, the position and the depth of its wells. The same approach can be observed in the broken/unbroken potential energy of Fig. 3.1 (second panel).

The first theoretical approaches based on this method have been developed to model the biomechanical response of skeletal muscles (Huxley et al. 1971; Hill 1973). Since these pioneering investigations, this technique has been generalized to study different multistable systems including the folding of macromolecules (Giordano 2017; Benedito et al. 2018a,b, 2019; Florio et al. 2019; Bellino et al. 2019; Benedito et al. 2020a,b; Jorge Do Marco et al. 2022), the adhesion/deadhesion processes (Florio et al. 2020; Cannizzo et al. 2021), the phase transformations in solids (Bellino et al. 2020; Cannizzo et al. 2022), the stick-slip on rigid and soft substrates (Giordano 2022, 2023), and the fracture mechanics (Cannizzo et al. 2023). The introduction of the spin variables frequently simplifies the calculation of

the partition function and, consequently, the analysis of the corresponding averaged thermodynamic quantities. This theoretical device is able to give mathematical results in closed form, very useful to advance the understanding of the underlying mechanics and physics. It is important to remark that, as discussed in detail in Refs. (Giordano 2017), the evaluation of the partition function based on the spin approach assumes that for both configurations all possible deformations (values of x in Fig. 3.1, first row) can be attained by the system. This corresponds to the assumption of a multivalued energy function (see superposition of dashed lines in Fig. 3.1, first row). As shown numerically in Refs. (Giordano 2017), with typical experimental temperatures, the effect of this approximation can be considered (statistically) negligible since these artificial configurations (superposition of dashed curves) have an energy sensibly higher than real configurations (continuous lines). This technique has been largely exploited to investigate bistable systems from biophysics and materials science, as mentioned above.

The stretching of macromolecular chain or, more in general, the mechanical perturbation of small systems with micro-instabilities can be typically performed following two different experimental protocols (Giordano 2017; Benedito et al. 2018a; Florio et al. 2020). In particular, experiments performed at constant applied forces (realized through extremely soft devices) correspond to the Gibbs statistical ensemble, and experiments performed at prescribed displacements (conducted with extremely hard devices) are a realization of the Helmholtz statistical ensemble. In general, these two boundary conditions lead to different force-extension responses since in each of the two cases we explore a different phase space. Actually, depending on the equivalent stiffness of the device, the stretching experiment corresponds to a situation placed in between the Gibbs and Helmholtz ensembles of the statistical mechanics (Florio et al. 2019; Bellino et al. 2019).

The introduction of different boundary conditions leads to the notion of thermodynamic limit. In particular, it is possible to prove under precise hypotheses that the two different experimental strategies give the same results in terms of force-extension curve when the number of system units or domains (monomers for a polymeric structure) is large enough (thermodynamic limit) (Weiner 2002; Winkler 2010; Manca et al. 2012, 2013a, 2014a; Giordano 2018; Manca et al. 2013b; Buche et al. 2020). Therefore, it is important to remark that the differences between the force-extension curves measured under Gibbs or Helmholtz conditions can be noticed only for a moderately small number of units or domains of the system under consideration (small systems thermodynamics). Indeed, for a large number of units or domains, i.e., in the thermodynamic limits, the different Gibbs and Helmholtz statistical ensembles are equivalent, and they are described by the same constitutive force-extension response (Weiner 2002; Winkler 2010; Manca et al. 2012, 2013a, 2014a; Giordano 2018; Manca et al. 2013b; Buche et al. 2020). However, it is important to mention the fact that in some cases the ensemble equivalence is not verified, and also in the thermodynamic limit we can have different macroscopic response of the system (Skvortsov et al. 2007; Dimitrov et al. 2009; Skvortsov et al. 2012; Dutta et al. 2018, 2019; Noh et al. 2021).

To conclude this introduction, we present here the structure of this review. In Sect. 2, we introduce the statistical mechanics and the thermodynamics of a system with conformational transitions, described by the spin variable method. In particular we prove the coherence between this technique and the main results of the macroscopic thermodynamics. In Sect. 3, we describe the results obtained with the force spectroscopy methods on macromolecules, and we discuss their interpretation through models based on the spin variable technique. In Sect. 4, we introduce the phase transformations in solid materials, and we show a method able to take into consideration the energy of the domain walls between different phases. This is applied to describe the tensile behavior of nanowires. Then, in Sect. 5 we develop the statistical mechanics of the adhesion/deadhesion processes and present an application to the interpretation of the DNA and RNA hairpins unzipping. Finally, in Sect. 6, we generalize the theory for adhesion/deadhesion processes by taking into account the possible softening mechanism before the complete detachment. This approach can be used to model the particular behavior of the fracture process of metal, metal oxides, or alloy micro- or nanowires.

2 Thermodynamics of Small Systems with Micro-instabilities

We present here a general methodology to study the thermodynamics of a system composed of two-state units and subjected to different boundary conditions. As discussed in the introduction, the main idea consists in associating with each unit a discrete variable (or spin variable), able to define the state of the unit itself. Such a variable represents a sort of "bit," assuming the values 0 and 1 for the folded and the unfolded states, respectively. The spin variables are considered as dynamic variables, thus belonging to the extended phase space of the system. The introduction of the spin variables allows to strongly facilitate the calculation of the partition functions, preserving at the same time a good accuracy of results (Giordano 2017). With this approach, an arbitrary potential function composed of two minima can be substituted by two quadratic potentials, and the switching between them is governed by the corresponding spin variable (see Fig. 3.1, first panel). Similarly, the method can also be applied to the case of rupture phenomena (see Fig. 3.1, second panel). This methodology works for both Gibbs and Helmholtz ensembles, allowing to draw direct comparisons between isotensional and isometric conditions (see Fig. 3.2). We remark that the spin variables approach can be only adopted for systems at thermodynamic equilibrium. As a matter of fact, the quadratic potentials and the associated spin variables are not sufficient to describe the dynamics, since the characteristic relaxation times strongly depend on the energy barriers between the potential wells. This is a well-known result, encoded within the Kramers rate formula, originally formulated to study chemical reactions (Kramers 1940), and recently generalized for arbitrary systems with non-convex energy landscapes (Benichou et al. 2015, 2016). Here, we use the spin variable approach in both Helmholtz and Gibbs ensembles, and we show how it

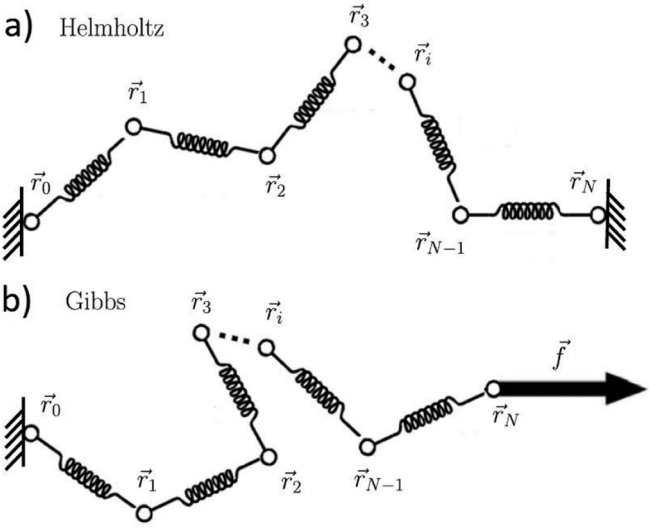

Fig. 3.2 Representation of a system under isotensional condition corresponding to the Gibbs ensemble (**a**) and a system under isometric condition corresponding to the Helmholtz ensemble (**b**)

allows obtaining well-known general results of the thermodynamics. We therefore introduce a general methodology to describe the problem of the conformational transitions in complex systems composed of N units. The more general form of the corresponding Hamiltonian can be written as

$$H = \sum_{i=1}^{N} \frac{\mathbf{p}_i \cdot \mathbf{p}_i}{2M} + U\left(\mathbf{r}_1, \ldots, \mathbf{r}_N, S_1, \ldots, S_N\right) - \sum_{i=1}^{N} \mu_i S_i, \tag{3.1}$$

where $S_i \in \{0, 1\}$ are the spin variables $\forall i = 1, \ldots, N$ introduced in the potential energy U. A domain is said *folded* (i.e., it is in the first energy well) when $S_i = 0$ and *unfolded* (i.e., it is in the second energy well) when $S_i = 1$. It is important to remark that in this review sometimes we use the values $\{0, 1\}$ for the spin and sometimes the values $\{-1, +1\}$. Conceptually there is no difference, but values $\{-1, +1\}$ are more convenient for implementing Ising's model.

The first term represents the kinetic energy ($\mathbf{p}_i$ are the linear momenta of the units and M is their mass), and the second term represents the potential energy depending on the units positions $\mathbf{r}_i$ and on the spins S_i. Finally, the third term mimics the effect of the external chemical environment on the state of the domains: If $\mu_i > 0$, the unfolded state is favored, and conversely, if $\mu_i < 0$, the folded state is favored. The chemical potentials μ_i may describe the effect of some chemical process, able to induce or to hinder the units unfolding.

The folding/unfolding of the units, here described by the spin variables, is controlled by the mechanical boundary conditions applied to the chain and by the chemical potentials of the external environment. We consider here a chain with the first extremity tethered at the origin of the reference frame. In general, an arbitrary chain described by Eq. (3.1) can be studied within the Helmholtz ensemble or within the Gibbs ensemble of the statistical mechanics (see Fig. 3.2). In the first situation, we fix the second extremity at a given point of the space, while, in the second situation, we apply an external force to the last unit. In the following, we briefly describe the statistical mechanics of both ensembles, eventually verifying that the proposed approach yields results, which are coherent with standard thermodynamics (Gibbs 1902; Weiner 2002).

Within the Helmholtz ensemble (see Fig. 3.2a), we have a specific Hamiltonian given by

$$H_H = H(\mathbf{q}, \mathbf{p}, \mathbf{S}; \mathbf{r}, \boldsymbol{\mu}), \tag{3.2}$$

where we introduced $\mathbf{q} = (\mathbf{r}_1, \ldots, \mathbf{r}_{N-1})$ (we fixed $\mathbf{r}_N = \mathbf{r}$), $\mathbf{p} = (\mathbf{p}_1, \ldots, \mathbf{p}_{N-1})$ (we fixed $\mathbf{p}_N = 0$), $\mathbf{S} = (S_1, \ldots, S_N)$, and $\boldsymbol{\mu} = (\mu_1, \ldots, \mu_N)$. In this scheme, $\mathbf{r}$ and $\boldsymbol{\mu}$ are externally controlled variables, and $\mathbf{q}$, $\mathbf{p}$, and $\mathbf{S}$ are the dynamical variables of the phase space. Therefore, the density probability of the canonical ensemble is given by (Gibbs 1902; Weiner 2002)

$$\rho_H(\mathbf{q}, \mathbf{p}, \mathbf{S}) = \frac{1}{Z_H(\mathbf{r}, \boldsymbol{\mu}, T)} \exp\left[-\frac{H_H(\mathbf{q}, \mathbf{p}, \mathbf{S}; \mathbf{r}, \boldsymbol{\mu})}{k_B T}\right], \tag{3.3}$$

where the Helmholtz partition function reads

$$Z_H(\mathbf{r}, \boldsymbol{\mu}, T) = \sum_{\mathbf{S} \in \{0,1\}^N} \int_Q \int_Q \exp\left[-\frac{H_H(\mathbf{q}, \mathbf{p}, \mathbf{S}; \mathbf{r}, \boldsymbol{\mu})}{k_B T}\right] \mathrm{d}\mathbf{q}\mathrm{d}\mathbf{p}, \tag{3.4}$$

where $Q = \mathbb{R}^{3(N-1)}$. By means of this probability density, one can determine the average value of any macroscopic variable. This is the reason why calculating the partition function is of vital importance in statistical mechanics. In particular, the average value of the force $\mathbf{f} = \frac{\partial H_H}{\partial \mathbf{r}}$ needed to fix $\mathbf{r}_N = \mathbf{r}$ and the average value of each spin variable S_i can be easily obtained through the introduction of the Helmholtz free energy $\mathcal{F} = -k_B T \log Z_H$. Indeed, straightforward calculations yield $\langle \mathbf{f} \rangle = \frac{\partial \mathcal{F}}{\partial \mathbf{r}}$ and $\langle \mathbf{S} \rangle = -\frac{\partial \mathcal{F}}{\partial \boldsymbol{\mu}}$, which represent two macroscopic or thermodynamic relations. Moreover, the first and second principles for quasi-static transformations can be derived as follows from previous statements. First of all, we define a quasi-static transformation through the time evolution of $\mathbf{r}(t)$, $\boldsymbol{\mu}(t)$, and $T(t)$, which are considered as externally controlled "slow-varying" variables. Under these hypotheses, we can assume that the canonical distribution in Eq. (3.3) remains valid also in this "weak" out-of-equilibrium regime. Therefore, we can evaluate

the rate of change of the internal energy $\mathcal{U}$, defined as the average value of the Helmholtz Hamiltonian

$$\begin{aligned}\frac{\mathrm{d}\mathcal{U}}{\mathrm{d}t} &= \sum_{\mathbf{S}} \int_Q \int_Q \frac{\mathrm{d}}{\mathrm{d}t} \left(H_H \rho_H\right) \mathrm{d}\mathbf{q}\mathrm{d}\mathbf{p} \\ &= \sum_{\mathbf{S}} \int_Q \int_Q \left(\frac{\partial H_H}{\partial \boldsymbol{\mu}} \cdot \frac{\mathrm{d}\boldsymbol{\mu}}{\mathrm{d}t} + \frac{\partial H_H}{\partial \mathbf{r}} \cdot \frac{\mathrm{d}\mathbf{r}}{\mathrm{d}t} \right) \rho_H \mathrm{d}\mathbf{q}\mathrm{d}\mathbf{p} + \sum_{\mathbf{S}} \int_Q \int_Q H_H \frac{\mathrm{d}\rho_H}{\mathrm{d}t} \mathrm{d}\mathbf{q}\mathrm{d}\mathbf{p} \\ &= -\langle \mathbf{S} \rangle \cdot \frac{\mathrm{d}\boldsymbol{\mu}}{\mathrm{d}t} + \langle \mathbf{f} \rangle \cdot \frac{\mathrm{d}\mathbf{r}}{\mathrm{d}t} + \sum_{\mathbf{S}} \int_Q \int_Q H_H \frac{\mathrm{d}\rho_H}{\mathrm{d}t} \mathrm{d}\mathbf{q}\mathrm{d}\mathbf{p}, \end{aligned} \tag{3.5}$$

where all the sums on $\mathbf{S}$ are performed over $\{0, 1\}^N$. The first two terms represent the chemical and the mechanical work per unit of time, respectively, done on the system, while the third one describes the rate of heat entering the system. The latter can be further elaborated by defining $\eta = \frac{\mathcal{F} - H_H}{k_B T}$ and $\rho_H = e^{\eta}$. Since $\sum_{\mathbf{S}} \int_Q \int_Q e^{\eta} \mathrm{d}\mathbf{q}\mathrm{d}\mathbf{p} = 1$, the derivative with respect to the time gives $\sum_{\mathbf{S}} \int_Q \int_Q e^{\eta} \dot{\eta} \mathrm{d}\mathbf{q}\mathrm{d}\mathbf{p} = 0$, and since $\mathcal{F}$ is independent of $\mathbf{S}$, $\mathbf{q}$, and $\mathbf{p}$, we can also write that $\sum_{\mathbf{S}} \int_Q \int_Q \mathcal{F} e^{\eta} \dot{\eta} \mathrm{d}\mathbf{q}\mathrm{d}\mathbf{p} = 0$. The last term in Eq. (3.5) can therefore be rewritten as

$$\begin{aligned}\sum_{\mathbf{S}} \int_Q \int_Q H_H \frac{\mathrm{d}\rho_H}{\mathrm{d}t} \mathrm{d}\mathbf{q}\mathrm{d}\mathbf{p} &= \sum_{\mathbf{S}} \int_Q \int_Q H_H e^{\eta} \dot{\eta} \mathrm{d}\mathbf{q}\mathrm{d}\mathbf{p} \\ &= \sum_{\mathbf{S}} \int_Q \int_Q \left(H_H - \mathcal{F}\right) e^{\eta} \dot{\eta} \mathrm{d}\mathbf{q}\mathrm{d}\mathbf{p}. \end{aligned} \tag{3.6}$$

Now, since $H_H - \mathcal{F} = -k_B T \eta$, we also have

$$\sum_{\mathbf{S}} \int_Q \int_Q H_H \frac{\mathrm{d}\rho_H}{\mathrm{d}t} \mathrm{d}\mathbf{q}\mathrm{d}\mathbf{p} = -k_B T \sum_{\mathbf{S}} \int_Q \int_Q e^{\eta} \eta \dot{\eta} \mathrm{d}\mathbf{q}\mathrm{d}\mathbf{p}. \tag{3.7}$$

This expression can be easily interpreted by considering the average value of the variable η given by $\langle \eta \rangle = \sum_{\mathbf{S}} \int_Q \int_Q e^{\eta} \eta \mathrm{d}\mathbf{q}\mathrm{d}\mathbf{p}$ and its time derivatives

$$\frac{\mathrm{d}\langle \eta \rangle}{\mathrm{d}t} = \sum_{\mathbf{S}} \int_Q \int_Q e^{\eta} \dot{\eta} \mathrm{d}\mathbf{q}\mathrm{d}\mathbf{p} + \sum_{\mathbf{S}} \int_Q \int_Q e^{\eta} \eta \dot{\eta} \mathrm{d}\mathbf{q}\mathrm{d}\mathbf{p}. \tag{3.8}$$

Since the first integral is zero for previous calculations, we eventually obtain

$$\sum_{\mathbf{S}} \int_Q \int_Q H_H \frac{\mathrm{d}\rho_H}{\mathrm{d}t} \mathrm{d}\mathbf{q}\mathrm{d}\mathbf{p} = -k_B T \frac{\mathrm{d}\langle \eta \rangle}{\mathrm{d}t} = T \frac{\mathrm{d}\mathcal{S}}{\mathrm{d}t}, \tag{3.9}$$

where we introduced the entropy of the system as

$$\mathcal{S} = -k_B \langle \log \rho_H \rangle = -k_B \sum_{\mathbf{S}} \int_Q \int_Q \rho_H \log \rho_H \mathrm{d}\mathbf{q}\mathrm{d}\mathbf{p}. \tag{3.10}$$

The first and the second principles of the thermodynamics for quasi-static transformations can be finally summed up through the balance equation

$$\frac{\mathrm{d}\mathcal{U}}{\mathrm{d}t} = -\langle \mathbf{S} \rangle \cdot \frac{\mathrm{d}\boldsymbol{\mu}}{\mathrm{d}t} + \langle \mathbf{f} \rangle \cdot \frac{\mathrm{d}\mathbf{r}}{\mathrm{d}t} + T\frac{\mathrm{d}\mathcal{S}}{\mathrm{d}t}. \tag{3.11}$$

Hence, we proved that the macroscopic thermodynamics is perfectly coherent with the approach based on the spin variables, introduced to analyze systems with conformational transitions. In addition, the average value of the relation $H_H - \mathcal{F} = -k_B T \eta$ yields $\mathcal{F} = \mathcal{U} - T\mathcal{S}$, which corresponds to the macroscopic definition of Helmholtz free energy. By differentiating with respect to the time, we also have

$$\frac{\mathrm{d}\mathcal{F}}{\mathrm{d}t} = -\langle \mathbf{S} \rangle \cdot \frac{\mathrm{d}\boldsymbol{\mu}}{\mathrm{d}t} + \langle \mathbf{f} \rangle \cdot \frac{\mathrm{d}\mathbf{r}}{\mathrm{d}t} - \mathcal{S}\frac{\mathrm{d}T}{\mathrm{d}t}, \tag{3.12}$$

from which we can deduce the two already introduced equations $\langle \mathbf{f} \rangle = \frac{\partial \mathcal{F}}{\partial \mathbf{r}}$ and $\langle \mathbf{S} \rangle = -\frac{\partial \mathcal{F}}{\partial \boldsymbol{\mu}}$ and the important relation $\mathcal{S} = -\frac{\partial \mathcal{F}}{\partial T}$, giving the entropy in terms of the Helmholtz free energy.

Concerning the Gibbs ensemble (see Fig. 3.2b), we can introduce the following extended Hamiltonian:

$$H_G = H(\mathbf{q}, \mathbf{p}, \mathbf{S}; \boldsymbol{\mu}) - \mathbf{f} \cdot \mathbf{r}_N, \tag{3.13}$$

where the second term represents the energy associated with the external force applied to the last unit of the chain. Here, we introduced $\mathbf{q} = (\mathbf{r}_1, \ldots, \mathbf{r}_N)$, $\mathbf{p} = (\mathbf{p}_1, \ldots, \mathbf{p}_N)$, $\mathbf{S} = (S_1, \ldots, S_N)$, and $\boldsymbol{\mu} = (\mu_1, \ldots, \mu_N)$. In this scheme, $\mathbf{f}$ and $\boldsymbol{\mu}$ are externally controlled variables, and $\mathbf{q}$, $\mathbf{p}$, and $\mathbf{S}$ are the dynamical variables of the phase space. Therefore, the density probability of the canonical ensemble is given by (Gibbs 1902; Weiner 2002)

$$\rho_G(\mathbf{q}, \mathbf{p}, \mathbf{S}) = \frac{1}{Z_G(\mathbf{f}, \boldsymbol{\mu}, T)} \exp\left[-\frac{H_G(\mathbf{q}, \mathbf{p}, \mathbf{S}; \mathbf{f}, \boldsymbol{\mu})}{k_B T}\right], \tag{3.14}$$

where the Gibbs partition function reads

$$Z_G(\mathbf{f}, \boldsymbol{\mu}, T) = \sum_{\mathbf{S} \in \{0,1\}^N} \int_{\mathcal{P}} \int_{\mathcal{P}} \exp\left[-\frac{H_G(\mathbf{q}, \mathbf{p}, \mathbf{S}; \mathbf{f}, \boldsymbol{\mu})}{k_B T}\right] \mathrm{d}\mathbf{q}\mathrm{d}\mathbf{p}, \tag{3.15}$$

where $\mathcal{P} = \mathbb{R}^{3N}$. As before, the most important expected values can be evaluated through the introduction of the Gibbs free energy $\mathcal{G} = -k_B T \log Z_G$. Simple calculations yield indeed $\langle \mathbf{r} \rangle = -\frac{\partial \mathcal{G}}{\partial \mathbf{f}}$ (where $\mathbf{r} = \mathbf{r}_N$) and $\langle \mathbf{S} \rangle = -\frac{\partial \mathcal{G}}{\partial \boldsymbol{\mu}}$, which represent two classical thermodynamic relations. Also in this isotensional case, we can introduce a quasi-static transformation through the time evolution of $\mathbf{f}(t)$, $\boldsymbol{\mu}(t)$, and $T(t)$, which are, as before, externally controlled "slow-varying" variables. We can assume that the canonical distribution in Eq. (3.14) remains valid, and we can evaluate the rate of change of the average value of the Gibbs Hamiltonian, which is the so-called enthalpy $\mathcal{H}$

$$\begin{aligned}\frac{\mathrm{d}\mathcal{H}}{\mathrm{d}t} &= \sum_{\mathbf{S}} \int_{\mathcal{P}} \int_{\mathcal{P}} \frac{\mathrm{d}}{\mathrm{d}t} \left(H_G \rho_G\right) \mathrm{d}\mathbf{q}\mathrm{d}\mathbf{p} \\ &= \sum_{\mathbf{S}} \int_{\mathcal{P}} \int_{\mathcal{P}} \left(\frac{\partial H_G}{\partial \boldsymbol{\mu}} \cdot \frac{\mathrm{d}\boldsymbol{\mu}}{\mathrm{d}t} + \frac{\partial H_G}{\partial \mathbf{f}} \cdot \frac{\mathrm{d}\mathbf{f}}{\mathrm{d}t} \right) \rho_G \mathrm{d}\mathbf{q}\mathrm{d}\mathbf{p} + \sum_{\mathbf{S}} \int_{\mathcal{P}} \int_{\mathcal{P}} H_G \frac{\mathrm{d}\rho_G}{\mathrm{d}t} \mathrm{d}\mathbf{q}\mathrm{d}\mathbf{p} \\ &= -\langle \mathbf{S} \rangle \cdot \frac{\mathrm{d}\boldsymbol{\mu}}{\mathrm{d}t} - \langle \mathbf{r} \rangle \cdot \frac{\mathrm{d}\mathbf{f}}{\mathrm{d}t} + \sum_{\mathbf{S}} \int_{\mathcal{P}} \int_{\mathcal{P}} H_G \frac{\mathrm{d}\rho_G}{\mathrm{d}t} \mathrm{d}\mathbf{q}\mathrm{d}\mathbf{p}. \end{aligned} \tag{3.16}$$

While the first two terms represent the power (chemical and mechanical) supplied to the system, the third term is the rate of heat transferred to the system. A calculation similar to the one developed for the Helmholtz ensemble allows us to rewrite this last term as follows:

$$\frac{\mathrm{d}\mathcal{H}}{\mathrm{d}t} = -\langle \mathbf{S} \rangle \cdot \frac{\mathrm{d}\boldsymbol{\mu}}{\mathrm{d}t} - \langle \mathbf{r} \rangle \cdot \frac{\mathrm{d}\mathbf{f}}{\mathrm{d}t} + T \frac{\mathrm{d}\mathcal{S}}{\mathrm{d}t}, \tag{3.17}$$

where the entropy for the Gibbs ensemble is given by

$$\mathcal{S} = -k_B \langle \log \rho_G \rangle = -k_B \sum_{\mathbf{S}} \int_{\mathcal{P}} \int_{\mathcal{P}} \rho_G \log \rho_G \mathrm{d}\mathbf{q}\mathrm{d}\mathbf{p}. \tag{3.18}$$

We can straightforwardly prove the thermodynamic relation $\mathcal{G} = \mathcal{H} - T\mathcal{S}$, and we obtain the rate of change of the Gibbs free energy as

$$\frac{\mathrm{d}\mathcal{G}}{\mathrm{d}t} = -\langle \mathbf{S} \rangle \cdot \frac{\mathrm{d}\boldsymbol{\mu}}{\mathrm{d}t} - \langle \mathbf{r} \rangle \cdot \frac{\mathrm{d}\mathbf{f}}{\mathrm{d}t} - \mathcal{S} \frac{\mathrm{d}T}{\mathrm{d}t}. \tag{3.19}$$

The last energy balance immediately delivers the relations $\langle \mathbf{r} \rangle = -\frac{\partial \mathcal{G}}{\partial \mathbf{f}}$ and $\langle \mathbf{S} \rangle = -\frac{\partial \mathcal{G}}{\partial \boldsymbol{\mu}}$, previously demonstrated, and the result $\mathcal{S} = -\frac{\partial \mathcal{G}}{\partial T}$, corresponding to the macroscopic definition of entropy.

The two approaches outlined represent complete procedures able to deliver thermomechanical response of a small system undergoing conformational transitions under isometric or isotensional boundary conditions. We proved that the introduction of additional spin variables to describe the change of state of the units leaves unaltered the general results of the thermodynamics, thus being

well-grounded and promising for applications. It is important to remark that the thermoelastic response may be different for the two introduced ensembles if we consider chains composed of a small number N of units (Weiner 2002). On the other hand, when the thermodynamic limit is attained (ideally for $N \to \infty$), the two ensembles become equivalent, and they exhibit the same physical response (Winkler 2010; Manca et al. 2012, 2013a, 2014a; Giordano 2018). This equivalence property is valid for non-branched single chains without confinements, i.e., freely fluctuating in the whole space. Therefore, in our analysis, the only constraints consist in the punctual boundary conditions defining the Helmholtz and the Gibbs ensembles. However, as discussed in the introduction, it is noteworthy to mention that some particular cases on nonequivalence between dual canonical ensembles have been recently discussed for confined polymer chains (Skvortsov et al. 2007; Dimitrov et al. 2009; Skvortsov et al. 2012; Dutta et al. 2018, 2019; Noh et al. 2021). In any case, having demonstrated the consistency of the spin method with thermodynamics allows us to use it freely in the study of systems with conformational transformations described, for example, by bistability, multistability, and deadhesion or fracture processes. In the remainder of this review, we show some applications of it.

3 Single-Molecule Force-Spectroscopy Measurements and Their Interpretation

It is well known that the biological functions of several macromolecules (for instance, nucleic acids, polysaccharides, and proteins) are strongly related to their three-dimensional conformations. It is therefore important to study the possible rearrangements induced by external actions (which can be entropic, purely mechanical, or chemical). For example, the tertiary structure of proteins completely controls the relation between structure and function. Under the action of some factors, the configuration of proteins can be modified, leading to some changes in the physical and chemical properties and, eventually, to the removal of their biological activity. For instance, the capacity of these macromolecules to keep their spatial configuration stable against mechanical factors must be tested to evaluate their ability to conserve their original biological behavior. Indeed, if a macromolecule is pulled with a large force, it can lose or change its biological function since the force reduces the structural stability and induces rearrangements. For an enzyme, this can represent the loss of its catalytic capacity, and for an antibody, this can produce the loss of its ability to bind to an antigen. Hence, the mechanical actions on biological macromolecules can lead to alterations in their functions, with crucial physiological consequences.

Studying the relation between the three-dimensional conformation of a macromolecule and its function can be directly done by using force spectroscopy methods, which can be applied to unfold, through a mechanical stretching, the native folded structure of a macromolecule. The controlled unfolding leads to

the estimate of the involved forces (it is indeed possible to measure the force-extension relation), the energy landscape, and many other dynamic properties of the system under investigation. We remark that the energy landscape of most biological macromolecules shows a multistable shape, characterized by several metastable states corresponding to different conformations. Therefore, the paths followed by the system to switch among these substates are specified by characteristic times that depend on the energy barriers between the states and on the external actions applied to the system. The mechanical experiments on single molecule are extremely useful to study intra- and intermolecular forces and to obtain information about the thermodynamics and kinetics of several molecular processes. Different force spectroscopy techniques allow the investigation of these macromolecular features. Single-molecule experiments are indeed based on laser optical tweezers (LOTs), magnetic tweezers (MTs), atomic force microscopes (AFMs), and micro-electromechanical systems (MEMS) (Strick et al. 2002; Ritort 2006; Cleri 2008; Neuman et al. 2008; Kumar et al. 2010; Mandal 2020). These approaches are important not only for probing the response of a single macromolecule but also for testing the validity of thermodynamics and statistical mechanics at the scale of atoms and molecules.

3.1 Optical Tweezers

Optical tweezers are devices able to exploit one or more focused laser beams to hold and move micro- or nanoparticles or beads. The first detection of forces on microparticles was performed by Arthur Ashkin in 1970, paving the way for the use of this new technology (Ashkin 1970a,b). Several years later, Ashkin and colleagues developed real single-beam gradient force traps, able to control the position of microscopic particles in the three-dimensional space (Ashkin et al. 1986). In 2018, Ashkin was awarded the Nobel Prize in Physics for the introduction of these devices, which was eventually used to manipulate atoms, molecules, and biological structures. This technique is able to generate an actual energy well in the space, and the force applied to the particle is proportional to the displacement from the equilibrium position. Hence, the optical tweezers act like a linear spring (in a given range) (Zaltron et al. 2020). These devices are able to apply forces in the range 0.1–100 pN with an intrinsic stiffness of 0.01–1 pN/nm and to measure the particle position with sub-nanometer resolution. Because of the rather limited force range, they have been mainly used in experiments on DNA and RNA and also with proteins or other molecules. However, the high-intensity laser used for the optical trapping generates a local heating, causing degradation or denaturation of biological structures and an alteration of the viscosity of the solution. A comprehensive tutorial on laser optical tweezers can be found in the literature (Gieseler et al. 2021).

3.2 Magnetic Tweezers

The second force spectroscopy technique mentioned is based on magnetic tweezers, which use magnets or electromagnets to create a magnetic field gradient able to generate force acting on a paramagnetic bead. The force is applied in the direction of the field gradient. Typically, the investigated macromolecule is attached to the bead, and it is therefore stretched. The second end-terminal of the molecule is tethered to the base or substrate, where the experiment is performed. The magnets' position and velocity are controlled in order to apply the desired molecular unfolding. The real-time detection of the bead position is realized with an optical system and a CCD camera. From the historical point of view, Francis Crick and Arthur Hughes firstly introduced a method based on magnetic particles to measure the physical properties of the cytoplasm in 1955 (Crick et al. 1950). This technique was later improved with the idea of studying the rheology of the cell (Valberg et al. 1985, 1987). Only in the 1990s this methodology was applied to single molecules, in particular to study the elasticity of DNA (Smith et al. 1992; Strick et al. 1996). In modern magnetic devices, the force applied can reach the value of 200 pN, and the magnetic trap stiffness is very low, around 10^{-4} pN/nm. The damage by heating and photodamage in biological structures is considerably reduced with magnetic tweezers based on permanent magnets. However, in some setups with electromagnets, high electric current may generate a large amount of heat, which requires the use of cooling systems. Importantly, magnetic tweezers, in addition to applying a longitudinal pull on the macromolecule, can be used to generate a chain twist. This is useful to study conformational transitions induced by twist mechanisms. In addition, magnetic tweezers have the advantage to be able to really exert a constant force, while in atomic force microscopes and optical tweezers the constant force mode can be achieved only by feedback-control systems, which are quite complex.

3.3 Atomic Force Microscope

The force spectroscopy based on the atomic force microscope is a well-established technique for studying strong covalent bonds and stiff intermolecular and intramolecular interactions. The original AFM is a device useful to investigate the morphological features of a material surface, capable of reaching the atomic resolution. This is typically done by monitoring the force between the surface under study and the tip of a silicon (or silicon nitride) cantilever. The position of the tip is measured by observing the deflection of the cantilever through a standard optical method. A piezoelectric system allows scanning the whole surface, eventually producing an image corresponding to the topographical structure of the surface. This classical atomic force microscope has been invented in 1985 by Gerd Binnig, Calvin Quate, and Christoph Gerber and commercialized for the first time in 1989 (Binnig et al. 1986). The AFM technique has been further generalized in order

to apply force on a single molecule and to measure force-extension curves of macromolecules. In this application, the chain is stretched between the tip of the cantilever and the substrate with forces ranging in the interval 20 pN–10 nN, with stiffness values of 10–10,000 pN/nm. The spatial resolution is around 0.2 nm. These data allow us to state that this method is useful for large macromolecules such as proteins. While the classical pulling speeds used in single molecule experiments vary in the range of a few nm/s to about 10 μm/s, the recently introduced high-speed AFM (HS-AFM) allowed to reach pulling speeds of the order of 4000 μm/s (Rico et al. 2013; Eghiaian et al. 2014; Valotteau et al. 2019; Rico et al. 2019). This is a significant development since it permits to compare the results of experiments with those obtained by molecular dynamics simulations, which offer atomic-level descriptions of the forced unfolding within the out-of-equilibrium statistical mechanics (Gräter et al. 2005; Lee et al. 2009).

3.4 MEMS Devices

A last class of devices used to perform single-molecule experiments is represented by the micro-electromechanical systems or MEMS devices. The development of MEMS devices started in the 1960s by means of the same technologies used for microelectronics. In fact, they are often based on silicon substrates suitably adapted and enriched with various components (Rai-Choudhury 2000). In general they are based on the combination of microelectronic systems with partially mobile mechanical systems. The moving components can be plates useful to change the capacitance of the structure or electrostatically controlled cantilevers. Typically, these systems are used to obtain sensors and captors of several physical quantities. MEMS for biological or biomedical applications are named Bio-MEMS and may integrate microfluidic chambers, biosensors, microarrays, microelectrodes, or microreactors (Folch 2013). Force spectroscopy techniques, based on optical or magnetic tweezers and AFM, are able to make precise measurements at the single-molecule level. However, their implementation and use is quite complex, and therefore they cannot be adopted for intensive and systematic biosensing. The application of MEMS devices in this context is promising. For instance, a micromachined DNA manipulation MEMS platform has been developed to stretch and rotate a single DNA molecule (Chiou et al. 2005). This device exploits the combination of micromachined magnetic tweezers and microfluidic channels. Another example concerns a new hybrid field microfluidic approach, employing both hydrodynamic forces and an electric field to regulate the DNA initial conformations (Ren et al. 2012). Moreover, micro-electromechanical systems have been developed for monitoring bio/chemical interactions of bio-macromolecules, by controlling their mechanical properties (Tarhan et al. 2016). To conclude, a specific MEMS device, referred to as silicon nanotweezers (SNTs), has been introduced to mechanically characterize a DNA bundle exposed to ionizing radiations, delivered by a therapeutic linear particle accelerator (LINAC) (Yamahata et al. 2008; Perret et al. 2016, 2017). The

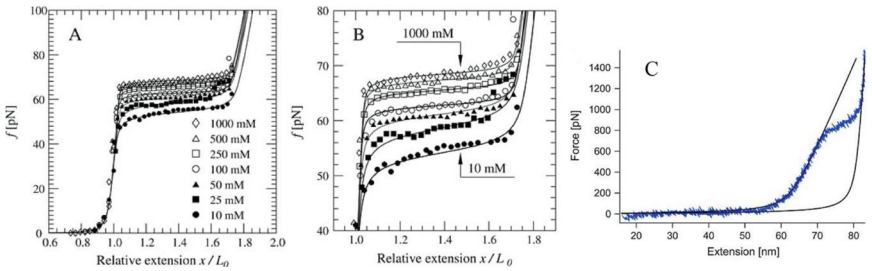

Fig. 3.3 Panel **a**: room temperature force-extension curves for a single dsDNA molecule in different salt concentrations. The solid lines correspond to theoretical curves calculated using the global coupling theory developed by Punkkinen et al. (2005). Experimental data are taken from Wenner et al. (2002). Panel **b**: the same data of panel **a** showing only the overstretching portion. Panels **a** and **b** are reproduced with permission from Punkkinen et al. (2005). Panel **c**: force-extension curve (blue) from one dextran molecule obtained through AFM force spectroscopy and its fit in the low-force (before the transition) and high-force (after the transition) regime obtained by the extensible FJC model. Panel **c** is reproduced with permission from Walther et al. (2006)

radiation induces a mechanical degradation i.e., a population of breaks in a DNA bundle, which can be quantified by measuring the elastic properties of the bundle itself (Manca et al. 2014b, 2015). Hence, one could provide a direct relationship between radiation dose and its damaging effects. The real-time observation of the DNA degradation under ionizing radiation is useful to develop better techniques for the treatment of tumors.

3.5 Experimental Results on Force-Extension Curves

After this quick review of the technologies used to develop single-molecule force spectroscopy methods, we briefly describe the typical force-extension responses observed in these experiments. While the structure of DNA was first elucidated in 1953 by Watson and Crick (Watson et al. 1953), who obtained the Nobel Prize in Physiology or Medicine 1962, its mechanical behavior has been tested by magnetic tweezers force spectroscopy only in 1992 (Smith et al. 1992), eventually obtaining the force-extension relation. These results, for individual DNA molecules, were obtained at three different salt concentrations and with forces in the range from 10^{-14} to 10^{-11} N (Smith et al. 1992). These experimental achievements have been completely understood from the theoretical point of view by means of the statistical mechanics thanks to the works of Marko and Siggia (Marko et al. 1995; Bustamante et al. 1994). They proved that the DNA mechanics is well reproduced by the worm-like chain (WLC) model rather than by the freely jointed chain (FJC) model. The ideal FJC model schematizes the macromolecule as a sequence of N non-deformable segments of length b (referred to as Kuhn length). The contour length L_C is the total length of the macromolecule at the maximum physically possible

extension, and then we have $L_C = Nb$ for a chain with N units. The FJC model does not take physical interactions among segments into account. Hence, there is no preferred angle between two adjacent segments. The force-extension response for the FJC model is given by

$$\frac{x}{Nb} = \coth\left(\frac{fb}{k_B T}\right) - \frac{k_B T}{fb} = \mathcal{L}\left(\frac{fb}{k_B T}\right), \tag{3.20}$$

where x is the extension of the chain, N is the number of units, b is the segment length, f is the applied force, k_B is the Boltzmann constant, T is the temperature, and $\mathcal{L}$ is the Langevin function, defined as $\mathcal{L}(z) = \coth(z) - \frac{1}{z}$. This model is useful to describe simple polymer chains but is not adapted for the DNA. Differently, the WLC model perfectly mimics double-stranded DNA, in the first entropic region of the force-extension curve (Marko et al. 1995; Bustamante et al. 1994). In the ideal FJC model, no forces are necessary to fold or bend the chain. On the contrary, in the WLC model, energy depending on the angles between adjacent segments is introduced. More precisely, the energy is set to zero if all segments are aligned, and therefore a force can be applied to fold or bend the chain. This property is taken into consideration by means of a new parameter called persistence length p, which is defined by the ratio between the mechanical flexibility or bending stiffness and the energy of thermal fluctuations. Hence, it takes into account the balance between enthalpic and entropic contributions (Marko et al. 1995). From the physical point of view, the persistence length p can be defined as the length over which correlations in the direction of the tangent are lost. The behavior of a WLC chain is described by

$$f = \frac{k_B T}{p}\left[\frac{1}{4}\left(1 - \frac{x}{L_C}\right)^2 - \frac{1}{4} + \frac{x}{L_C}\right], \tag{3.21}$$

where the quantities are defined above. The DNA used in the first force spectroscopy experiment corresponds to a contour length $L_C = 32.8\mu\text{m}$ and a persistence length $p = 53.4\,\text{nm}$ (Marko et al. 1995; Bustamante et al. 1994).

Refined experiments have been realized on DNA with magnetic torque tweezers in order to measure the effective torsional stiffness as function of the applied force (Lipfert et al. 2010, 2011). Recently, an alternative, more refined, WLC model was proposed to correctly take account of both bending and torsional stiffness by adding a coupling term between twist and bend deformations (Nomidis et al. 2017, 2019).

In further investigations, the DNA molecule has been pulled with larger forces, and an intriguing overstretching phenomenon has been observed (Smith et al. 1996). In particular, a force plateau at around 65 pN has been measured in the force-extension curve (Smith et al. 1996). In Fig. 3.3a, b, we show recent results proving the dependence of the plateau on the salt concentration. Here, the theoretical results are taken from Punkkinen et al. (2005) whereas the experimental ones from Wenner et al. (2002). The overstretching behavior can be interpreted by means of a bistability of the DNA chain structure. However, the real molecular

origin of this transition has been largely investigated, and a debate exists on the DNA conformation after the overstretching: Many researchers think that there is a simple mechanical denaturation leading to a transformation of the double-stranded DNA into two single-stranded DNA (Rouzina et al. 2001a,b). However, other researchers have proposed the existence of a new DNA conformation (called S-DNA or stretched DNA), which is an intermediate structure between the double-stranded DNA and its denatured structure (Cocco et al. 2004). Finally, other researchers thought that melting or S-DNA was depending on the composition in amino acids of the chain (Bosaeus et al. 2012). A discrete worm-like chain model has been implemented to describe the DNA stretching under force and to investigate dsDNA to ssDNA and dsDNA to S-DNA transitions (Manghi et al. 2012).

The force-extension curve exhibiting a force plateau, corresponding to a conformational transition of the molecule, has been observed also for other macromolecules. An interesting example concerns a polysaccharide called dextran. A dextran filament has been tethered to a gold surface and probed with the atomic force microscope tip by means of a vertical stretching (Rief et al. 1997a). At low forces the deformation of dextran is dominated by entropic forces and can be described by the FJC model with a Kuhn length of around 6 Å. At more elevated forces the dextran filament exhibits a reversible conformational transition characterized by a force plateau (Rief et al. 1997a). This transition has been explained in terms of a two-state model implemented through Monte Carlo simulations (Rief et al. 1998). In Fig. 3.3c we show the force-extension curve for dextran recently obtained with AFM force spectroscopy (Walther et al. 2006). These measurements have been realized with a refined AFM variance analysis able to detect conformational changes at the sub-Angstrom scale (Walther et al. 2006). Also artificial polymers can show conformational transitions characterized by a force plateau. The study of these structures is referred to as covalent polymer mechanochemistry. In this context, chemical transformation is activated by external mechanical forces applied to the polymer chain. An example of interesting molecular architecture is given by the cyclobutane mechanophore operating as a gate to regulate the mechanical activation of a second mechanophore, thus resulting in a mechanochemical cascade reaction (Wang et al. 2016). Single-molecule force spectroscopy shows a force-extension curve characterized by a force plateau in correspondence to the opening/closing transition of the gate (Wang et al. 2016). Also in this case, the underlying bistability is able to generate the conformational transition of the molecular structure.

We have introduced a first class of mechanical responses characterized by a force plateau corresponding to the transition of the units of the chain between two configurational states. This force plateau corresponds to a synchronized transition of all the units, which is induced by the external force applied to stretch the chain. A second class of responses has been observed in different single-molecule experiments, typically concerning multi-domain proteins. The folding and unfolding of these protein systems has been widely observed through the AFM force spectroscopy. Many proteins with important biological mechanical functions are composed of many units having the same chemical composition, i.e., the same amino acid sequence. Moreover, each unit can have one or more stable configuration, and the

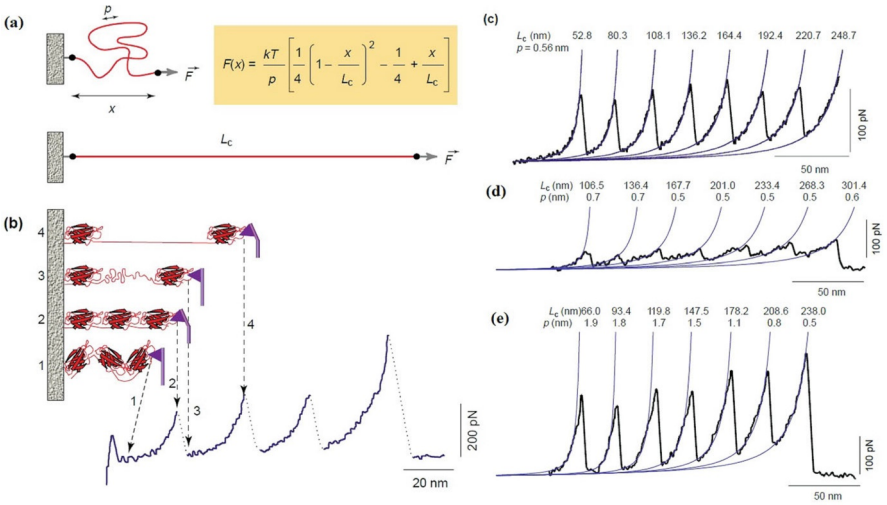

Fig. 3.4 Force spectroscopy measurements on proteins based on the AFM device. Panel (**a**): worm-like chain (WLC) model for a semiflexible chain used to interpret the unfolding on each protein domain. Here, L_c is the contour length of the chain, and p is the persistent length. Panel (**b**): sawtooth force-extension curve describing the sequential unfolding of the protein domains. Panel (**c**): force-extension curve for the recombinant human tenascin-C. Panel (**d**): force-extension curve for the cytoskeletal protein spectrin showing a heterogeneous persistence length. Panel (**e**): force-extension curve for a recombinant fragment of titin consisting of titin Ig domains 27–34. The figure is reproduced with permission from Fisher et al. (1999)

transition between these states can be induced by applied forces. The typical force-extension response observed for these systems is represented by a sawtooth curve, where each force peak represents the unfolding of one unit. Therefore, in this case, the overall unfolding process is sequential and not synchronized as discussed above for other structures (nucleic acids and polysaccharides). The characteristic sawtooth pattern, with the number of peaks equal to the number of domains, has been first observed with titin (Rief et al. 1997b) and later with tenascin (Oberhauser et al. 1998) and spectrin (Rief et al. 1999). The sequential character of the force-extension curve can be found in Fig. 3.4, where we show the WLC model for the unfolding of one unit, the overall chain unfolding under AFM stretching, and some examples of proteins (Fisher et al. 1999).

In order to explain the emergence of two different classes of force-extension responses (with force plateau or sawtooth pattern), we present in the next section a simple model able to introduce the bistability within the classical freely jointed chain scheme. This model will be named the bistable freely jointed chain (BFJC) model. Furthermore, we introduce a generalization taking into account the elasticity of each unit of the chain. The obtained model is referred to as extensible bistable freely jointed chain (EBFJC) model.

3.6 *Bistable Freely Jointed Chain Model*

In this section, we describe a generalization of the classical FJC model able to take into account the two-state behavior or, equivalently, the bistability of the units of the chain (see Fig. 3.5). In this model the units are free to fluctuate in the three-dimensional space, and the potential energy of each unit of the chain is characterized by a bistable behavior (see Fig. 3.6, left panel). The two potential wells can be written as

$$U(\mathbf{r}, s) = v(s) + \frac{1}{2}k(s)\left[\|\mathbf{r}\| - \ell(s)\right]^2, \tag{3.22}$$

where $\mathbf{r}$ is the vector joining the end-terminals of the unit. Here, we adopted the method of the spin variables based on the introduction of a discrete variable s, which is able to distinguish between the two quadratic wells of the system (Giordano 2017). Indeed, the quantity $s \in \{0, 1\}$ allows us to identify the potential well explored by the vector $\mathbf{r}$. The physical parameters $v(s)$, $k(s)$, and $\ell(s)$ represent the basal energy, the elastic stiffness, and the equilibrium length of the two potential wells characterizing the system bistability. We remark that in the classical FJC model, the elastic stiffness tends to infinity, or equivalently, the length of each element is kept constant. Accordingly, the mechanical behavior is fully governed by entropic forces since the elastic or enthalpic contribution is not taken into account. Here, for mathematical convenience, it is better to proceed from Eq. (3.22), with finite elastic constants, and to analyze the limiting cases in the following phase. The case with finite extensibility will be treated in the following section. In order to explain the origin of the two classes of mechanical responses observed in single-molecule force spectroscopy experiments, described in the previous section, we analyze the behavior of the system under the two Gibbs and Helmholtz ensembles (see Fig. 3.5). The study of both configurations with an arbitrary number N of units of the chain will be useful to better understand the force-extension curves observed experimentally.

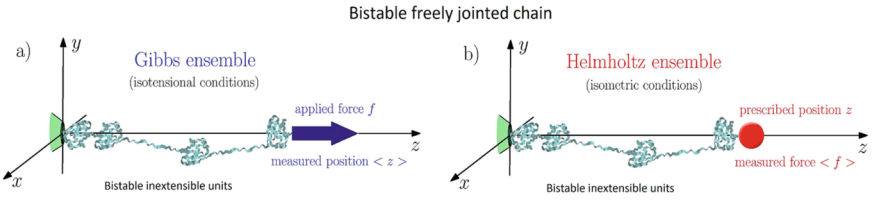

Fig. 3.5 Scheme of the statistical Gibbs (**a**) and Helmholtz (**b**) ensembles, corresponding to the isotensional and isometric conditions applied to a bistable freely jointed chain with N domains. While in the Gibbs ensemble (**a**) we apply the force f and we measure the average position $\langle z \rangle$, in the Helmholtz ensemble (**b**) we impose the position z and we measure the average force $\langle f \rangle$

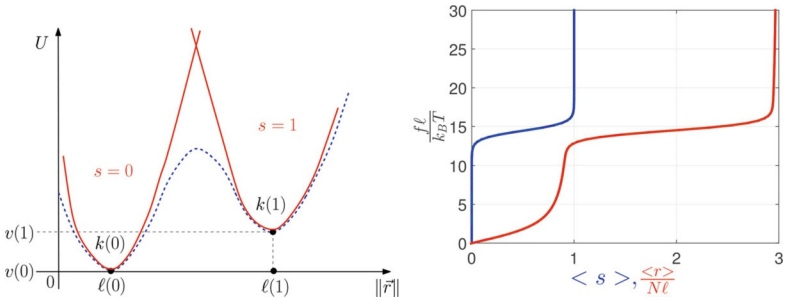

Fig. 3.6 Left panel: potential energy of a single element of the bistable freely jointed chain (BFJC) model (dashed blue curve). The potential wells are approximated through two parabolic profiles identified by $s = 0$ and 1. Right panel: average normalized extension (red line) and normalized spin variable (blue line) versus the dimensionless force for the bistable freely jointed chain under Gibbs conditions. We adopted the parameters $\Delta E = 30 k_B T$ and $\chi = 3$ (at $T = 300$K). The curves are independent of N within the Gibbs ensemble (with normalized extension)

3.6.1 The Gibbs Ensemble for the BFJC Model

Now, we consider a chain of N units described by Eq. (3.22), with an external force applied to the last one (see Fig. 3.5a). In this condition, the total potential energy of the system can be written as

$$U_{tot}(\mathbf{q}, \mathbf{s}; \mathbf{f}) = \sum_{i=1}^{N} U(\mathbf{r}_i - \mathbf{r}_{i-1}, s_i) - \mathbf{f} \cdot \mathbf{r}_N, \tag{3.23}$$

where $\mathbf{q} = (\mathbf{r}_1, \ldots, \mathbf{r}_N)$ is the vector containing all the coordinates $\mathbf{r}_1, \ldots, \mathbf{r}_N$, $\mathbf{s} = (s_1, \ldots, s_N)$ is the vector with all spin variables, and $\mathbf{f}$ is the force applied to the last unit of the chain. The last term in the expression of the total energy represents the effect of the force $\mathbf{f}$. Of course, we consider the system embedded in a thermal bath at temperature T, and we examine its thermomechanical response at thermodynamic equilibrium. Therefore, the system is governed by the canonical distribution of the statistical mechanics. The partition function within the Gibbs ensemble can be determined by summing the discrete spin variables and integrating the continuous spatial ones, as follows:

$$Z_G(\mathbf{f}) = \sum_{s_1 \in \{0,1\}} \cdots \sum_{s_N \in \{0,1\}} \int_{\Re^{3N}} e^{-\frac{U_{tot}(\mathbf{q},\mathbf{s};\mathbf{f})}{k_B T}} \, \mathrm{d}\mathbf{q}. \tag{3.24}$$

To fix ideas, the physical properties of the two potential wells of the bistable energy can be defined by $v(0) = 0$, $\ell(0) = \ell$, $k(0) = k$ and $v(1) = \Delta E$, $\ell(1) = \chi \ell$, $k(1) = k$, where ΔE is the energy jump between the folded and unfolded states and χ is the ratio between the unfolded and folded equilibrium lengths. A straightforward integration, described by Giordano (2017), delivers

$$Z_G = c\left\{\int_0^\infty e^{-\frac{k}{2k_BT}[\xi-\ell]^2}\frac{\sinh\left(\frac{f\xi}{k_BT}\right)}{\frac{f\xi}{k_BT}}\xi^2 d\xi + \phi\int_0^\infty e^{-\frac{k}{2k_BT}[\xi-\chi\ell]^2}\frac{\sinh\left(\frac{f\xi}{k_BT}\right)}{\frac{f\xi}{k_BT}}\xi^2 d\xi\right\}^N, \tag{3.25}$$

where c represents a non-influential multiplicative constant and $\phi = \exp\left(-\frac{\Delta E}{k_BT}\right)$ is a Boltzmann factor calculated through the energy jump ΔE. The units of the chain do not interact, and therefore the partition function has been found in the form of a power with exponent N (which is a classical property of noninteracting systems). In order to exactly define the behavior of the BFJC model, we must evaluate the limit for k approaching infinity of the partition function obtained in Eq. (3.25). This allows us to consider units without extensibility. To determine this limiting behavior, we can use the classical Dirac delta function representation $\sqrt{\frac{\alpha}{\pi}}e^{-\alpha(x-x_0)^2} \underset{\alpha\to\infty}{\to} \delta(x-x_0)$, eventually yielding (Giordano 2017)

$$Z_G = c\left[\frac{\sinh y}{y} + \chi\phi\frac{\sinh(\chi y)}{y}\right]^N, \tag{3.26}$$

where we introduced the dimensionless force $y = \frac{\ell f}{k_BT}$. If the system under consideration is not bistable (e.g., obtained with $\Delta E \to \infty$ or, equivalently, with $\phi \to 0$), the second term in Eq. (3.26) vanishes, and we obtain

$$Z_G = c\left(\frac{\sinh y}{y}\right)^N, \tag{3.27}$$

which is the classical partition function of the FJC model (Weiner 2002; Doi 1996; Glatting et al. 1993; Manca et al. 2012). The cases with finite values of the elastic constant will be considered in the next section. Within the Gibbs ensemble, the standard relation $\langle r\rangle = k_BT\frac{\partial \log Z_G}{\partial f}$ permits to find the force-extension response for the bistable freely jointed chain as follows:

$$\langle r\rangle = N\ell\frac{\mathcal{L}(y) + \chi^2\phi\mathcal{L}(\chi y)\frac{\sinh(\chi y)}{\sinh y}}{1+\chi\phi\frac{\sinh(\chi y)}{\sinh y}}, \tag{3.28}$$

where $\mathcal{L}(y) = \coth y - \frac{1}{y}$ is the Langevin function. The average value of the spin variables can be naturally defined as $\langle s\rangle = \frac{1}{N}\left\langle\sum_{i=1}^N s_i\right\rangle$, and therefore it is not difficult to prove that $\langle s\rangle = -k_BT\frac{\partial \log Z_G}{N\partial\Delta E}$. A second important result can be therefore written as

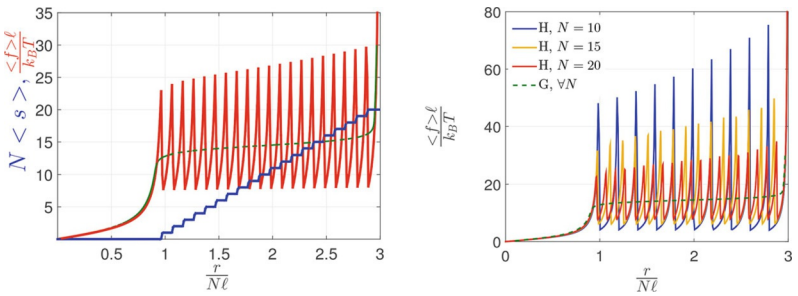

Fig. 3.7 Left panel: average dimensionless force (red line) and average spin variable (blue line) versus normalized extension for the bistable freely jointed chain under Helmholtz conditions. We adopted the parameters $\Delta E = 30 k_B T$, $\chi = 3$, and $N = 20$ (at $T = 300$ K). We also plotted for comparison the force-extension Gibbs response (dashed green line). Right panel: force-extension response under Helmholtz (H) conditions for $N = 10, 15, 20$ and under Gibbs (G) condition to show the equivalence of the ensembles in the thermodynamic limit. We adopted the parameters $\Delta E = 30 k_B T$, and $\chi = 3$

$$\langle s \rangle = \frac{\chi \phi \frac{\sinh(\chi y)}{\sinh y}}{1 + \chi \phi \frac{\sinh(\chi y)}{\sinh y}}. \tag{3.29}$$

Equations (3.28) and (3.29) completely characterize the behavior of the BFJC model under isotensional condition. An application of Eqs. (3.28) and (3.29) is shown in Fig. 3.6, right panel, where the average normalized extension and the average value of the spin variables are represented versus the dimensionless force. The force-extension curve shows a collective behavior due to the synchronized unfolding of all the chain units at the threshold value of the dimensionless force $\frac{f^* \ell}{k_B T} = \frac{\Delta E}{(\chi - 1) k_B T}$. The spin variable curve confirms this behavior by exhibiting a clear transition from 0 to 1 at the same threshold value of the force. It means that all spins switch at the same time proving the synchronized character generated by the isotensional condition. It is interesting to remark that the force-extension curve is similar to the one of DNA and dextran described in the previous section.

3.6.2 The Helmholtz Ensemble for BFJC Model

Now, we consider the chain of bistable elements with the two end-terminals tethered at points $\mathbf{r}_0 = \mathbf{0}$ and $\mathbf{r}_N = \mathbf{r}$ (see Fig. 3.5b). It means that we are working under isometric condition and therefore within the Helmholtz ensemble of the statistical mechanics. In this case, the total potential energy of the system can be written as

$$U_{tot}^{H}(\mathbf{q}, \mathbf{s}; \mathbf{r}_N) = \sum_{i=1}^{N} U(\mathbf{r}_i - \mathbf{r}_{i-1}, s_i), \tag{3.30}$$

where $\mathbf{r}_N = \mathbf{r}$ is the fixed extremity of the chain, $\mathbf{q} = (\mathbf{r}_1, \ldots, \mathbf{r}_{N-1})$ is the vector containing all positions $\mathbf{r}_1, \ldots, \mathbf{r}_{N-1}$, and $\mathbf{s} = (s_1, \ldots, s_N)$ is the vector of all spin variables. The potential energy $U(\mathbf{r}, s)$ of a single unit used in Eq. (3.30) is given in Eq. (3.22). The Helmholtz partition function for this system can be written as

$$Z_H(\mathbf{r}_N) = \sum_{s_1 \in \{0,1\}} \cdots \sum_{s_N \in \{0,1\}} \int_{\Re^{3(N-1)}} e^{-\frac{U_{tot}^H(\mathbf{q},\mathbf{s};\mathbf{r}_N)}{k_B T}} \mathrm{d}\mathbf{q}. \tag{3.31}$$

The comparison of Eqs. (3.24) and (3.31) allows us to state that the relation between the two partition functions Z_G and Z_H is described through a three-dimensional bilateral Laplace transform, as follows:

$$Z_G(\mathbf{f}) = \int_{\Re^3} Z_H(\mathbf{r}) \exp\left(\frac{\mathbf{r} \cdot \mathbf{f}}{k_B T}\right) \mathrm{d}\mathbf{r}. \tag{3.32}$$

Moreover, since the problem is spherically symmetric, we easily get the following simpler relationship:

$$Z_H(r) = c \int_{-\infty}^{+\infty} Z_G(i\eta) \frac{\eta}{r} \sin\left(\frac{\eta r}{k_B T}\right) \mathrm{d}\eta, \tag{3.33}$$

where c is an unimportant constant and $Z_G(i\eta)$ represents the analytic continuation of the Gibbs partition function over the imaginary axis. By substituting Eq. (3.26), we get the important integral expression

$$Z_H(r) = c \int_{-\infty}^{+\infty} \left[\frac{\sin y}{y} + \chi\phi \frac{\sin(\chi y)}{y}\right]^N \frac{y}{r} \sin\left(\frac{ry}{\ell}\right) \mathrm{d}y. \tag{3.34}$$

If the studied system is not bistable (with $\Delta E \to \infty$ or, equivalently, with $\phi \to 0$), the partition function can be simplified to

$$Z_H(r) = c \int_{-\infty}^{+\infty} \left(\frac{\sin y}{y}\right)^N \frac{y}{r} \sin\left(\frac{ry}{\ell}\right) \mathrm{d}y, \tag{3.35}$$

a result that has been largely studied by Rayleigh (1919), Polya (1913), Treloar (1946), and Wang et al. (1952), to analyze the behavior of chains and chains

networks. For the bistable case, by means of an integration based on the complex variables techniques, we get the following result (Giordano 2017):

$$Z_H(r) = \frac{\pi c}{2^{(N-1)}(N-2)!r} \sum_{k=0}^{N} \sum_{p=0}^{N-k} \sum_{q=0}^{k} \binom{N}{k} \binom{N-k}{p} \binom{k}{q} \times (-1)^{p+q} (\chi\phi)^k (-\Lambda)^{N-2} \mathbf{1}(\Lambda), \tag{3.36}$$

written in terms of the Heaviside step function $\mathbf{1}(x)$, defined as $\mathbf{1}(x) = 1$ if $x \geq 0$ and $\mathbf{1}(x) = 0$ if $x < 0$. Here we defined $\Lambda = k - N + 2p - \chi k + 2\chi q - \frac{r}{\ell}$. In this isometric case, the partition function cannot be written in terms of a power with exponent N because of the effective interaction among the elements induced by the Helmholtz boundary condition. The knowledge of the partition function allows us to obtain the force-extension response through the expression

$$\langle f \rangle = -k_B T \frac{\partial \log Z_H}{\partial r} \tag{3.37}$$

and the average value of the spin variables, as follows:

$$\langle s \rangle = \left\langle \frac{1}{N} \sum_{i=1}^{N} s_i \right\rangle = -\frac{1}{N} k_B T \frac{\partial \log Z_H}{\partial \Delta E}. \tag{3.38}$$

We show an example of application of Eqs. (3.37) and (3.38) in Fig. 3.7, left panel. The typical sawtooth-like curve is observed in the force-extension response, corresponding to a sequential nonsynchronized process. This is explained by the individual successive unfolding of the domains, one by one, as also confirmed by the average value of the spin variable, which exhibits a series of steps corresponding to each unfolding process. Moreover, in Fig. 3.7, right panel, the force-extension curve in the Helmholtz ensemble is shown for different values of $N = 10, 15$, and 20. It is important to remark that when the number N of elements increases, the Helmholtz response converges to the Gibbs one, by progressively reducing the pick-to-pick distance in the sawtooth pattern. The equivalence of the ensembles in the thermodynamic limit is therefore confirmed for the BFJC model, as recently demonstrated for a large class of non-confined polymer chains (Manca et al. 2014a; Winkler 2010).

To conclude, we described an application of the spin variables method in both the Gibbs and the Helmholtz ensembles, allowing to consider a fluctuating chain in the three-dimensional space. The obtained results allow us to give a direct interpretation of the synchronized and sequential responses of the folding/unfolding processes observed in experimental measurements. We therefore elaborated a methodology able to provide a unified modeling for such apparently contrasting experimental situations. It is important to observe that these results have been obtained for finite values of N, thus belonging to the so-called small systems thermodynamics.

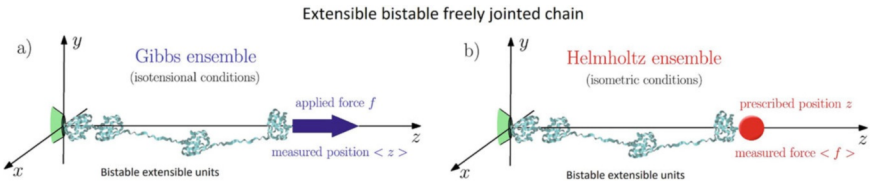

Fig. 3.8 Scheme of the statistical Gibbs (**a**) and Helmholtz (**b**) ensembles, corresponding to the isotensional and isometric conditions applied to an extensible bistable freely jointed chain with N domains. While in the Gibbs ensemble (**a**) we apply the force f and we measure the average position $\langle z \rangle$, in the Helmholtz ensemble (**b**) we impose the position z and we measure the average force $\langle f \rangle$

3.7 Extensible Bistable Freely Jointed Chain Model

An important generalization of the bistable freely jointed chain concerns the extensibility of the bonds between the chain units. The classical FJC model, and its bistable version BFJC previously discussed, considers rigid segments of fixed length. In this section, we develop the theory for the EBFJC model determining the analytic solution for the partition functions of chains made of bistable units, taking account of extensibility, within both the Gibbs and the Helmholtz ensembles (see Fig. 3.8) (Benedito et al. 2018a). The finite elastic constant of the bonds between the units plays a major role in defining the force-extension response in both isotensional and isometric ensembles. In particular, within the Helmholtz ensemble, the peak-to-peak force of the sawtooth-like curve strongly depends on the intrinsic elastic constant of the units. This point is important for interpreting the results of the force spectroscopy measurements on proteins. From the mathematical point of view, the most difficult issue concerns the calculation of the Helmholtz partition function. Eventually, its closed-form expression has been found in terms of the Hermite polynomials, suitably generalized to negative indices.

3.7.1 The Gibbs Ensemble for the EBFJC Model

We take into consideration a two-state freely jointed chain composed of N domains under isotensional condition (see Fig. 3.8a). Here, instead of considering the units with an infinite elastic stiffness, like in Sect. 3.6, we try to consider a finite elasticity for the bistable units. The potential energy function of each unit is represented in Fig. 3.6, left panel, where the two wells correspond to the folded and unfolded configurations. As before, the spin variable approach consists in considering two quadratic curves, approximating the wells of this system and introducing a spin variable for each unit, useful to identify the potential well explored during the system evolution. A refined approximation of Eq. (3.25), developed by Benedito et al. (2018a), leads to the partition function

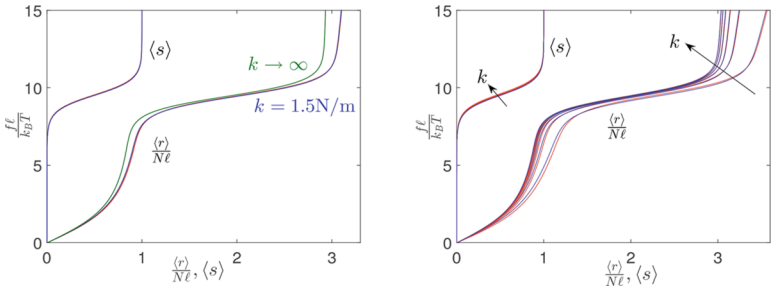

Fig. 3.9 Left panel: force-extension response and average spin for a system with extensibility ($k = 1.5$ N/m) and a system without extensibility ($k \to \infty$). The calculation for the system with extensibility is based on the exact result in Eq. (3.25) (red curves) and on the approximation in Eq. (3.39) (blue curves). On the other hand, the system without extensibility has been studied through Eq. (3.26). Right panel: force-extension response and average spin for a system with variable extensibility $k = 0.4$, 0.8, 1.2, 1.6, 2.0 and 2.4 N/m. The calculation of the force-extension response and the average spin is based on the exact result in Eq. (3.25) (red curves) and on the approximation in Eq. (3.39) (blue curves). In both panels, we adopted the parameters $N = 5$, $\ell = 0.5 \times 10^{-9}$ m, $T = 300$K, $\chi = 3$, $\Delta E = 20 k_B T = 8.28 \times 10^{-20}$ J

$$Z_G(f) = \left[\frac{\sinh y}{y} + \phi\chi \frac{\sinh(\chi y)}{y} \right]^N \exp\left(\frac{N\alpha y^2}{2} \right), \tag{3.39}$$

where $y = \frac{\ell f}{k_B T}$ is the dimensionless force, and $\alpha = \frac{k}{2k_B T}$ represents the ratio between enthalpic contributions and thermal effects. The exponential term depending on α is responsible for the elasticity of the chain. The same result without bistability (i.e., with $\phi = 0$) has been discussed in recent literature (Radiom et al. 2017; Balabaev et al. 2009; Buche et al. 2022). Moreover, the case with bistability but without extensibility of the units is considered in Sect. 3.6. The knowledge of the partition function allows the calculation of the force-extension relation in the form

$$\langle r \rangle = N\ell \left[\frac{\mathcal{L}(y) + \chi^2 \phi \mathcal{L}(\chi y) \frac{\sinh(\chi y)}{\sinh y}}{1 + \chi\phi \frac{\sinh(\chi y)}{\sinh y}} + \alpha y \right], \tag{3.40}$$

where $\mathcal{L}(y) = \coth y - \frac{1}{y}$ is the Langevin function. On the other hand, we get the average value of the spin variables as

$$\langle s \rangle = \frac{\chi\phi \frac{\sinh \chi y}{\sinh y}}{1 + \chi\phi \frac{\sinh \chi y}{\sinh y}}, \tag{3.41}$$

which does not depend on α. An example of application of this theory is given in Fig. 3.9, left panel, where we compare a system with extensibility described by the exact Eq. (3.25) or by the approximated Eq. (3.39) and another system

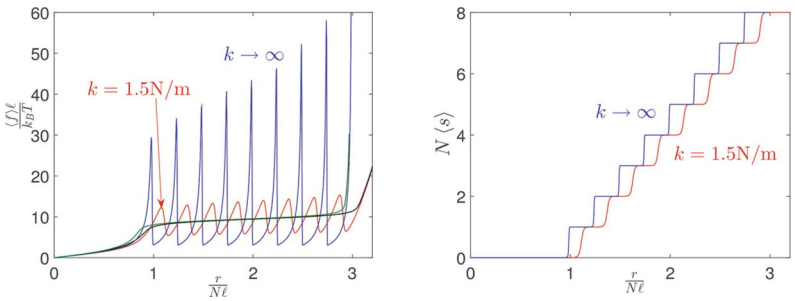

Fig. 3.10 Force-extension response (left panel) and average spin (right panel) for a system with extensibility ($k = 1.5\,\text{N/m}$) and a system without extensibility ($k \to \infty$). In the left panel, we also added the Gibbs force-extension responses for both cases. We adopted the parameters $N = 8$, $\ell = 0.5 \times 10^{-9}\,\text{m}$, $T = 300\text{K}$, $\chi = 3$, $\Delta E = 20 k_B T = 8.28 \times 10^{-20}\,\text{J}$, and $\mu = 0$

without extensibility described by Eq. (3.26). First of all, we remark the very good agreement between Eqs. (3.25) and (3.39) for the system with extensibility (red and blues curves, respectively, in Fig. 3.9). This proves the acceptability of the proposed approximation. Moreover, it is interesting to note the different asymptotic behaviors of systems with finite and infinite elastic constants. While the stiff system exhibits a vertical asymptote for large forces, the elastic one shows an asymptote with a slope representing the effective stiffness of the chain. In the force-extension curve, we observe a force plateau corresponding to $f^* = \frac{\Delta E}{(\chi - 1)\ell}$. Similarly, in the spin behavior, we identify a transition from 0 to 1 corresponding to the same force f^*. As before, we can explain these curves by means of a synchronized process, which generates the transition of all units at the same value of force f^*. A larger variation of the elastic constant is shown in Fig. 3.9, right panel, where the force-extension curve and the spin variables are plotted for several values of $k = 0.4, 0.8, 1.2, 1.6, 2.0$ and $2.4\,\text{N/m}$. Also in this case, we underline the good agreement between exact and approximated results, with a small deviation appearing only for the softer chains.

3.7.2 The Helmholtz Ensemble for the EBFJC Model

We consider now the isometric condition represented by the Helmholtz ensemble of the statistical mechanics (see Fig. 3.8b). In this case, the first unit of the chain is tethered at the origin of the reference frame and the last unit is tethered at a given point $\mathbf{r}$ of the space. By means of the Laplace transform between the Gibbs and Helmholtz partition functions previously discussed, we get the important integral expression

$$Z_H(r) = \int_{-\infty}^{+\infty} \left\{ \frac{\sin y}{y} + \chi\phi \frac{\sin(\chi y)}{y} \right\}^N \exp\left(-N\frac{\alpha y^2}{2}\right) \frac{y}{r} \sin\left(\frac{ry}{\ell}\right) \mathrm{d}y. \tag{3.42}$$

The analysis of such an integral for $\alpha = 0$ (i.e., without elasticity) has been performed in recent literature (Giordano 2017), and in Sect. 3.6. Previous investigations considered the case with $\alpha = 0$ and $\phi = 0$, thus dealing with the classical FJC model under isometric condition (Rayleigh 1919; Polya 1913; Treloar 1946; Wang et al. 1952). However, the presence of a finite elasticity of the units, quantified by the parameter $\alpha \neq 0$, completely modifies the approach to be used to obtain a closed-form expression for $Z_H(r)$. A detailed analysis of the problem has been performed by Benedito et al. (2018a), where the following closed-form expression of the Helmholtz partition function is derived

$$
\begin{aligned}
Z_H(r) = -\frac{1}{2r} \sum_{k=0}^{N} \sum_{p=0}^{N-k} \sum_{q=0}^{k} \binom{N}{k} \binom{N-k}{p} \binom{k}{q} (-1)^{p+q} \\
\times (\chi\phi)^k \left[\sqrt{\pi} \left(\frac{N\alpha}{2} \right)^{\frac{N-2}{2}} e^{-\frac{\Lambda^2}{2N\alpha}} H_{-N+1} \left(\frac{\Lambda}{\sqrt{2N\alpha}} \right) \right. \\
\left. + \mathbf{1}(\Lambda) \sum_{h=0}^{\left[\frac{N}{2}-1\right]} \frac{(-1)^{N-1} \pi \left(\frac{\Lambda}{2}\right)^{N-2}}{h!(N-2-2h)!} \left(\frac{N\alpha}{2\Lambda^2} \right)^h \right],
\end{aligned}
\tag{3.43}
$$

where $[x]$ represents the floor function giving the greatest integer that is less than or equal to x and Λ depends on k, p, and q through the relation $\Lambda = k - N + 2p - \chi k + 2\chi q - \frac{r}{\ell}$. Here, $\mathbf{1}(x)$ represents the Heaviside step function, defined as $\mathbf{1}(x) = 1$ if $x \geq 0$ and $\mathbf{1}(x) = 0$ if $x < 0$. Moreover, $H_{-n}(z)$ are the Hermite elements with negative indices, which are known recursively (Hu et al. 1995). This result allows us to determine the complete response of the two-state freely jointed chain with extensible units.

We show an example of application of this theory in Fig. 3.10, where we compare an elastic system described by Eq. (3.43) with a stiff one described by Eq. (3.36). In the left panel, we show the force-extension curve for the stiff system with $k \to \infty$ and for the elastic one with $k = 1.5$ N/m. Moreover, to better compare the responses, we added the Gibbs force-extension responses for both cases. In the right panel, the average value of the spin variables is also represented for the stiff and the soft systems. These results prove a sequential behavior characterized by a progressive unfolding of units in response to the increasing overall length. This behavior corresponds to a series of peaks in the force-extension curves and to a staircase function for the spin variable.

In Fig. 3.11, one can find the force-extension response (left panel) and the average spin variable (right panel) for a system with variable extensibility $k = 0.4, 0.8, 1.2, 1.6, 2.0$, and 2.4 N/m. We can observe the progressive increase of the peak-to-peak force of each unfolding transition with increasing values of the elastic constant. At the same time, the transition is sharper for stiffer systems, as clearly visible in the average spin curves. It means that for force spectroscopy

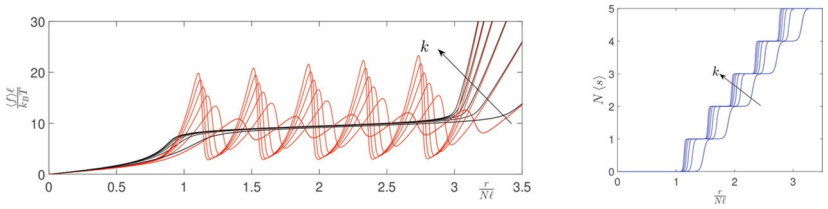

Fig. 3.11 Force-extension response (left panel) and average spin variable (right panel) for a system with variable extensibility $k = 0.4, 0.8, 1.2, 1.6, 2.0$ and 2.4 N/m. We added the Gibbs force-extension responses (black curves) to facilitate the comparison. We adopted the parameters $N = 5$, $\ell = 0.5 \times 10^{-9}$ m, $T = 300$K, $\chi = 3$, $\Delta E = 20 k_B T = 8.28 \times 10^{-20}$ J, and $\mu = 0$

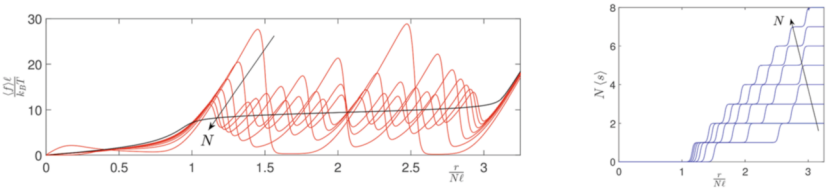

Fig. 3.12 Force-extension response (left panel) and average spin variable (right panel) for a system with a variable number of units $N = 2, 3, 4, 5, 6, 7$, and 8. We added the Gibbs force-extension responses (black curves) to facilitate the comparison. We adopted the parameters $k = 1$ N/m, $\ell = 0.5 \times 10^{-9}$ m, $T = 300$K, $\chi = 3$, $\Delta E = 20 k_B T = 8.28 \times 10^{-20}$ J, and $\mu = 0$

experiments, stiff macromolecules can be rather used than soft macromolecules to study cooperativity and other conformational properties.

Finally, we show in Fig. 3.12 the behavior of the system as a function of the number of units of the chain. This is an important analysis since it concerns the validity of the ensembles equivalence in the thermodynamic limit. In Fig. 3.12, one can find the results for N from 2 to 8 for a system with an elastic constant $k = 1$ N/m. It is interesting to remark that for an increasing value of N, the peak-to-peak force is progressively reduced, confirming the convergence of the Helmholtz ensemble to the Gibbs ensemble for $N \to \infty$. This is perfectly coherent with known results concerning the ensembles equivalence in the thermodynamic limit (Winkler 2010; Manca et al. 2014a).

To conclude, we can affirm that also the EBFJC model is able to show two different responses corresponding to the Gibbs and Helmholtz conditions, explaining the different classes of force-extension curves observed experimentally. Of course, we have shown here a qualitative explanation of these two types of behavior. It would be possible to refine the models with more specific ingredients (heterogeneity, dynamics, interactions between units, etc.) in order to show more quantitative comparisons as well, but we leave these aspects to the more specialized literature on the subject.

4 Phase Transformations in Solid Materials

We develop here a model to describe the temperature-dependent behavior of a one-dimensional nonlocal non-convex system (while the nonlocality describes the interaction among units, the non-convexity represents their multistable character). The paradigmatic system under investigation is composed of a sequence of units, which exhibit a bistable behavior described by a two-state potential energy and which are in interaction with each other. The proposed model is able to represent the phase transformations in materials and in particular in nanowires. This is a problem largely investigated within the micromechanics community (Truskinovsky et al. 1996; Shaw et al. 1997; Abeyaratne et al. 1996; Duval et al. 2011; Alessi et al. 2015; Song 2020). The two states of the bistable behavior represent in this case the two microstructures allowed to the solid material, corresponding, for example, to two different crystalline structures or amorphous configurations. This enables the study of pseudo-elasticity and shape memory effects in solid systems such as whiskers, nanowires, or nanocomposites. In this physical system the creation of a surface between two different phases, i.e., the nucleation of a new phase, is costly from the energetic point of view, and, therefore, with respect to previous models, we have to introduce an interaction between the units which favors two adjacent units in the same phase. Indeed, for these systems, we can adopt the Ising interaction scheme which reproduces the energy cost of creating an interface between the two different states of matter. This is therefore at the origin of the nucleation (generation of a new phase), propagation (motion of the interface between the phases), and coalescence (deletion of the original phase) phenomena. The complete solution of this problem obtained by taking into account N independent spins corresponding to the N units of the system has been presented by Cannizzo et al. (2022). Here, we present a simplified solution where only one interface or domain wall between the two phases is admitted. It represents systems where the interface energy is sufficiently large, as typical in many solid systems with two crystalline or amorphous phases.

We take into consideration a discrete chain of N two-state elements, each described by a bistable potential energy with a stable folded state and a metastable unfolded state (see Fig. 3.13a). The two potential wells can be characterized by the elastic constant $k(S_i)$, the equilibrium length $\ell_0(S_i)$, and the basal energy $v(S_i)$, where S_i is a discrete variable (or spin variable), assuming values in $\{-1, +1\}$, used to distinguish one well from the other. We state here that $S_i = +1$ corresponds to unfolded elements, whereas $S_i = -1$ corresponds to folded ones. In our case, we can therefore write that $\ell_0(-1) = \ell$, $v(-1) = 0$, $k(-1) = k_0$, $\ell_0(+1) = \chi\ell$, $v(+1) = \Delta E$, and $k(+1) = h_0$, where χ is the ratio between the unfolded and folded equilibrium lengths and ΔE is the energy jump between the states. We remark that we use here the values $\{+1, -1\}$ for the spins instead of $\{0, 1\}$ in order to implement the Ising scheme.

With the help of Fig. 3.13a, we can say that the bistable energy potential can be represented by two quadratic potentials (dashed lines) approximating the real wells of the units (continuous line). The introduction of the discrete variables also allows the direct implementation of an interaction between adjacent elements of the chain

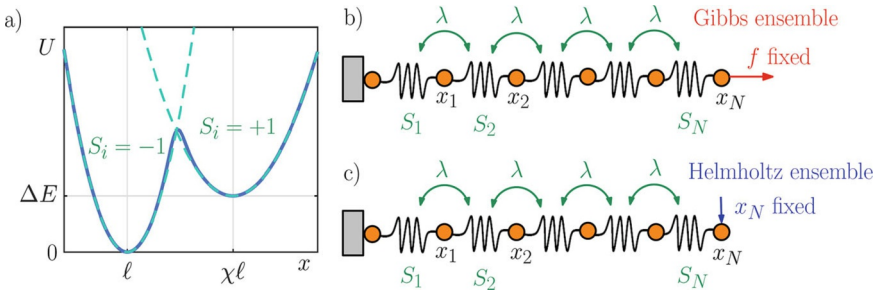

Fig. 3.13 Scheme of the investigated system. (**a**) Bistable potential energy $U(x)$ of each unit of the chain under study, where $x = x_i - x_{i-1}$ is the unit extension. The folded well corresponds to $S_i = -1$ and is characterized by $\ell_0(-1) = \ell$, $v(-1) = 0$, $k(-1) = k_0$. Meanwhile, the unfolded well, identified by $S_i = +1$, is defined through $\ell_0(+1) = \chi\ell$, $v(+1) = \Delta E$, $k(+1) = h_0$. (**b**) Isotensional configuration (Gibbs ensemble) of the nonlocal non-convex chain. (**c**) Isometric configuration (Helmholtz ensemble) of the nonlocal non-convex chain

that can be described by a classical Ising Hamiltonian. Hence, we will consider the overall Hamiltonian of the system written as

$$H = \sum_{i=1}^{N} \left\{ v(S_i) + \frac{1}{2} k(S_i) \left[x_i - x_{i-1} - \ell_0(S_i) \right]^2 \right\} - \lambda \sum_{i=1}^{N-1} S_i S_{i+1}, \tag{3.44}$$

where the first sum represents the energy of the series of non-convex bistable elements and the second sum the nonlocal interactions modeled by the Ising scheme, which is controlled by the parameter λ. The variables x_i define the continuous positions of the material points interacting through the bistable potentials and the Ising scheme. We remark that $\lambda > 0$ tries to force two adjacent elements to be in the same state either folded or unfolded (ferromagnetic-like interaction), whereas $\lambda < 0$ tries to force two adjacent elements to be in different states folded and unfolded (antiferromagnetic-like interaction). The approach used to deal with this general system is discussed by Cannizzo et al. (2022). To simplify the analysis, we develop here the theory for the nonlocal non-convex chain of bistable units under the assumption of strong ferromagnetic behavior, namely $\lambda \gg K_B T$. When this hypothesis is verified, we can consider only one interface or domain wall between two regions of the chain where the units are unfolded and folded, respectively (see Fig. 3.14). It means that this interface can move along the chain in response to the mechanical action and the temperature. This simplification is quite important since this allows us to find explicit expressions for both the Gibbs and Helmholtz ensembles, which can also be handled to perform the analysis of the thermodynamic limit. In particular, it is possible to prove the equivalence between the Gibbs and Helmholtz ensembles for $N \to \infty$. To be more precise, we can say that imposing a strong ferromagnetic behavior allows us to consider a chain composed by $N-\xi$ units in the folded state and the remaining ξ units in the unfolded, metastable, state. Here, ξ is a discrete variable assuming values in the set $\{0, 1, 2, \ldots, N\}$, representing the

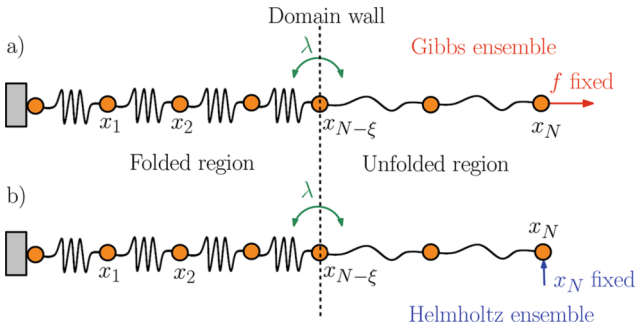

Fig. 3.14 Scheme of the zipper model. (**a**) Isotensional configuration (Gibbs ensemble) of the nonlocal non-convex chain with only one domain wall. (**b**) Isometric configuration (Helmholtz ensemble) of the nonlocal non-convex chain with only one domain wall

position, in terms of chain units, of the moving domain wall between folded and unfolded regions (see Fig. 3.14). Since the variable ξ can vary with temperature and external mechanical actions, this scheme can be called zipper model. This scheme has been used in other different statistical mechanics contexts (Gibbs et al. 1959; Crothers et al. 1965; Kittel 1969; Nishinari et al. 1990).

We can start from the same Hamiltonian defined in Eq. (3.44), and we can apply the necessary simplifications as follows. To begin with, the zipper assumption modifies the Ising sum in Eq. (3.44). In general, the sum $\sum_{i=1}^{N-1} S_i S_{i+1}$ is composed of $N-1$ addends that can be enumerated as follows: There are I addends with value -1 and $N-1-I$ addends with value $+1$, where I represents the number of changes in the spin sequence $S_1, \ldots, S_N$. Hence, we have that $\sum_{i=1}^{N-1} S_i S_{i+1} = (N-1-I) - I = N-1-2I$. In our zipper model, we must assume that $I(\xi) = 0$ if $\xi \in \{0, N\}$ (no interface) and $I(\xi) = 1$ if $1 \leq \xi \leq N-1$ (only one interface). Based on these considerations, the zipper Hamiltonian becomes

$$H_Z = \sum_{i=1}^{N} \left\{ v(i) + \frac{1}{2} k(i) \left[x_i - x_{i-1} - \ell_0(i) \right]^2 \right\} - \lambda (N - 1 - 2I(\xi)), \tag{3.45}$$

where we must assume that (i) if $i \leq N - \xi$ (folded units), then we have $v(i) = 0$, $k(i) = k_0$, $\ell_0(i) = \ell$, and (ii) if $i \geq N - \xi + 1$ (unfolded units), then $v(i) = \Delta E$, $k(i) = h_0$, $\ell_0(i) = \chi \ell$. We can also write the zipper Hamiltonian by separating the sum in Eq. (3.45) between folded and unfolded elements, obtaining

$$\begin{aligned} H_Z = & \sum_{i=1}^{N-\xi} \left\{ \frac{1}{2} k_0 \left[(x_i - x_{i-1}) - \ell \right]^2 \right\} \\ & + \sum_{i=N-\xi+1}^{N} \left\{ \Delta E + \frac{1}{2} h_0 \left[(x_i - x_{i-1}) - \chi \ell \right]^2 \right\} - \lambda \left[N - 1 - 2I(\xi) \right]. \end{aligned} \tag{3.46}$$

From now on, the discrete variable ξ belongs to the phase space of the system together with the continuous positions x_i.

4.1 Zipper Model Within the Gibbs Ensemble

Now we can use the zipper Hamiltonian for the evaluation of the partition function in the Gibbs ensemble (see Fig. 3.14a), defined as

$$Z_G(f) = \sum_{\xi=0}^{N} \int_{\mathbb{R}^N} \exp\left[-\frac{H_Z - f x_N}{K_B T}\right] \mathrm{d}x_1 \dots \mathrm{d}x_N. \tag{3.47}$$

If we develop this expression, we obtain after straightforward calculations

$$\begin{aligned} Z_G(f) = \sqrt{(2\pi K_B T)^N} \exp\left(\frac{(N-1)\lambda}{K_B T}\right) \sum_{\xi=0}^{N} \frac{1}{\sqrt{k_0^{N-\xi} h_0^{\xi}}} \\ \times \exp\left(-\frac{2\lambda}{K_B T} I(\xi) - \frac{\Delta E}{K_B T}\xi\right) \\ \times \exp\left(\frac{\ell f}{K_B T}[N + (\chi - 1)\xi] + \frac{f^2}{2K_B T}\left[\frac{N-\xi}{k_0} + \frac{\xi}{h_0}\right]\right). \end{aligned} \tag{3.48}$$

The knowledge of the Gibbs partition function allows us to calculate the average $\langle x \rangle$ of the chain extension (i.e., the average value of the last position x_N), the average number $\langle u \rangle$ of unfolded units, and the average number $\langle i \rangle$ of interfaces between folded and unfolded units as function of the applied force f, i.e., during a traction experiment. It is not difficult to realize that these three quantities can be expressed in the following way:

$$\langle x \rangle = K_B T \frac{\partial \log Z_G}{\partial f} = -\frac{\partial \mathcal{G}}{\partial f}, \tag{3.49}$$

$$\langle u \rangle = -K_B T \frac{\partial \log Z_G}{\partial \Delta E} = \frac{\partial \mathcal{G}}{\partial \Delta E}, \tag{3.50}$$

$$\langle i \rangle = \frac{N-1}{2} - \frac{K_B T}{2} \frac{\partial \log Z_G}{\partial \lambda} = \frac{N-1}{2} + \frac{1}{2}\frac{\partial \mathcal{G}}{\partial \lambda}, \tag{3.51}$$

where we introduced the Gibbs free energy of the system $\mathcal{G} = -K_B T \log Z_G$ (see Sect. 2). We can find an example of application of these results in Fig. 3.15. The first row of Fig. 3.15 shows $\langle x \rangle$, $\langle u \rangle$, and $\langle i \rangle$ versus the applied force f for the zipper model under isotensional condition with a variable Ising coefficient λ, and the second row shows $\langle x \rangle$, $\langle u \rangle$, and $\langle i \rangle$ versus f for the same zipper model with

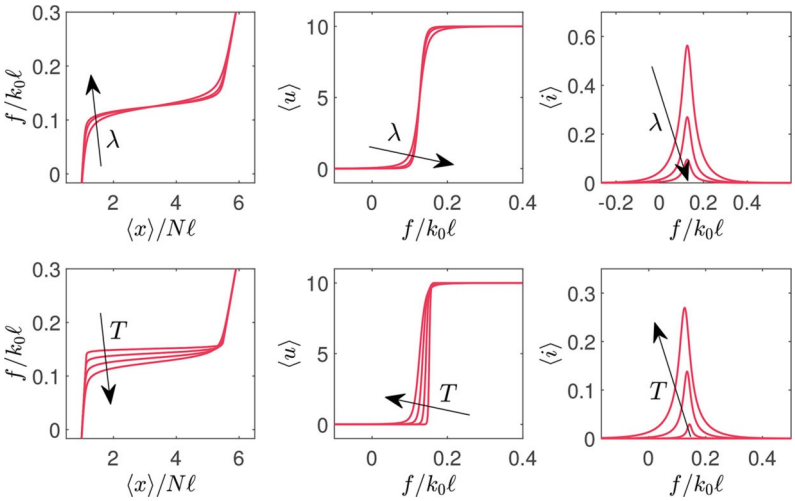

Fig. 3.15 Behavior of the zipper model within the Gibbs ensemble. In the first row $\langle x\rangle$, $\langle u\rangle$, and $\langle i\rangle$ are plotted versus f with a variable Ising coefficient $\lambda = \{5, 10, 15\}$ and a fixed temperature $K_B T = 10$. In the second row $\langle x\rangle$, $\langle u\rangle$, and $\langle i\rangle$ are plotted versus f with a variable temperature $K_B T = \{2, 4, 6, 8\}$ and a fixed Ising coefficient $\lambda = 5$. We adopted the parameters $N = 10$, $k_0 = 30$, $h_0 = 10$, $v(-1) = 0$, $v(+1) = \Delta E = 20$, $\ell = 1$, $\chi = 5$. All quantities are in arbitrary units

a variable temperature T. Concerning the force-extension relation and the plot of the average number of the unfolded units, these results confirm the synchronized behavior typical of the Gibbs ensemble, where all the units unfold cooperatively. We can also observe, as expected, that the effects obtained by increasing the temperature are exactly opposite to those observed by increasing the Ising coefficient. It is important to observe that, when $k_0 > h_0$, the force plateau seen in the force-extension curve decreases with temperature (while it increases with temperature when $k_0 < h_0$). As far as the average number of interfaces is concerned, we observe that a larger cooperativity reduces this value, as expected. Moreover, the number $\langle i\rangle$ of interfaces is an increasing function of the temperature.

It is interesting to determine analytically the force-extension relation for the zipper chain under isotensional condition. It means that we can calculate $\langle x\rangle$ through Eq. (3.49), where we use the partition function found in Eq. (3.48). The long but straightforward calculation of the derivative $\frac{\partial Z_G}{\partial f}$ delivers the force-extension relation in the form

$$\frac{\langle x\rangle}{N\ell} = \frac{\left[\left(1+\frac{f}{\ell k_0}\right)+\left(\chi+\frac{f}{\ell h_0}\right)e^{N\delta}\right]\left(1-\mathrm{x}^2\right)+\mathrm{x}^2\Sigma_1}{\left(1+e^{N\delta}\right)\left(1-\mathrm{x}^2\right)+\mathrm{x}^2\Sigma_2}, \tag{3.52}$$

where δ is defined as

$$\delta = \frac{1}{2}\ln\left(\frac{k_0}{h_0}\right) - \frac{\Delta E}{K_B T} + \frac{\ell f(\chi-1)}{K_B T} + \frac{f^2}{2K_B T}\left(\frac{1}{h_0} - \frac{1}{k_0}\right), \tag{3.53}$$

and where we introduced

$$\Sigma_1 = \left(1 + \frac{f}{\ell k_0}\right)\frac{1-e^{\delta(N+1)}}{1-e^{\delta}} \tag{3.54}$$
$$+\left[\chi - 1 + \frac{f}{\ell}\left(\frac{1}{h_0} - \frac{1}{k_0}\right)\right]\frac{1}{N}\frac{e^{\delta}}{(1-e^{\delta})^2}\left[1-(N+1)e^{N\delta} + Ne^{\delta(N+1)}\right],$$

$$\Sigma_2 = \frac{1-e^{\delta(N+1)}}{1-e^{\delta}}. \tag{3.55}$$

This result holds for nonlocal non-convex chains when $\lambda \gg K_B T$. This form of the force-extension relation is perfectly suited to study the thermodynamic limit, which is valid for $N \to \infty$ and $\lambda \gg K_B T$. We observe that the value of $\lim_{N\to\infty}\langle x\rangle/(N\ell)$ depends on the sign of δ, and we perform therefore the following analysis. If $\delta < 0$, then we get $\lim_{N\to\infty}\frac{\langle x\rangle}{N\ell} = 1 + \frac{f}{\ell k_0}$, which represents the elastic branch of the response observed when all units are folded. Conversely, if $\delta > 0$, we have $\lim_{N\to\infty}\frac{\langle x\rangle}{N\ell} = \chi + \frac{f}{\ell h_0}$, which represents the elastic branch of the response observed when all units are unfolded. Of course, the two elastic branches obtained here for $\delta < 0$ and $\delta > 0$ are separated by a force plateau corresponding to the equation $\delta = 0$, whose temperature dependent solution represents the Maxwell force f_M, obtained as

$$f_M(T) = \frac{-\ell(\chi-1) + \sqrt{\ell^2(\chi-1)^2 - 2\left(\frac{1}{h_0} - \frac{1}{k_0}\right)\left(\frac{K_B T}{2}\ln\frac{k_0}{h_0} - \Delta E\right)}}{\frac{1}{h_0} - \frac{1}{k_0}}. \tag{3.56}$$

A remarkable result is that the Maxwell force depends on the temperature T, as one can see in Fig. 3.15 also for $N = 10$ (Cannizzo et al. 2022). This is due to the fact that the two wells have different elastic constant $k_0 \neq h_0$. Indeed, when $k_0 = h_0$, we retrieve the expression $f = \Delta E/[\ell(\chi-1)]$, well known in the previous literature (Giordano 2017; Bell 1978; Bell et al. 1984; Manca et al. 2013b).

4.2 *Zipper Model Within the Helmholtz Ensemble*

We now can determine the partition function of the zipper model within the Helmholtz ensemble (see Fig. 3.14b). We eventually obtain

$$Z_H(x_N) = e^{\frac{\lambda}{K_B T}(N-1)} \sqrt{(2\pi K_B T)^{N-1}} \sum_{\xi=0}^{N} \exp\left(-\frac{2\lambda}{K_B T} I(\xi) - \frac{\Delta E}{K_B T}\xi\right) \times \frac{1}{\sqrt{k_0^{N-\xi} h_0^{\xi}}} \sqrt{\frac{1}{\left(\frac{N-\xi}{k_0} + \frac{\xi}{h_0}\right)}} \exp\left(-\frac{\{x_N - \ell[N + (\chi - 1)\xi]\}^2}{2K_B T\left(\frac{N-\xi}{k_0} + \frac{\xi}{h_0}\right)}\right). \tag{3.57}$$

This result, as for the Gibbs partition function seen before, allows us to determine the average value $\langle f \rangle$ of the force (i.e., the force-extension relation), the average value $\langle u \rangle$ of the number of unfolded units, and the average value $\langle i \rangle$ of the number of interfaces between folded and unfolded units. In fact, it is not difficult to prove these expressions

$$\langle f \rangle = -K_B T \frac{\partial \log Z_H}{\partial x_N} = \frac{\partial \mathcal{F}}{\partial x_N}, \tag{3.58}$$

$$\langle u \rangle = -K_B T \frac{\partial \log Z_H}{\partial \Delta E} = \frac{\partial \mathcal{F}}{\partial \Delta E}, \tag{3.59}$$

$$\langle i \rangle = \frac{N-1}{2} - \frac{K_B T}{2} \frac{\partial \log Z_H}{\partial \lambda} = \frac{N-1}{2} + \frac{1}{2} \frac{\partial \mathcal{F}}{\partial \lambda}, \tag{3.60}$$

where we introduced the Helmholtz free energy of the system $\mathcal{F} = -K_B T \log Z_H$ (see Sect. 2). An example of application of these results can be found in Fig. 3.16, where we show $\langle f \rangle$, $\langle u \rangle$, and $\langle i \rangle$ as function of the prescribed extension (we use x instead of x_N for notational simplicity) for different values of the Ising coefficient λ and the temperature T. More precisely, the first row of Fig. 3.16 shows $\langle f \rangle$, $\langle u \rangle$, and $\langle i \rangle$ versus x for the zipper model under isometric condition with a variable Ising coefficient λ, and the second row shows $\langle f \rangle$, $\langle u \rangle$, and $\langle i \rangle$ versus x for the same zipper model with a variable temperature T. Concerning the force-extension relation and the plot of the average number of the unfolded units, these results confirm the nonsynchronized or sequential behavior of the Helmholtz ensemble, where the units unfold one at a time in response to the increasing prescribed extension. We can also observe, similarly to the Gibbs ensemble, that the effects obtained by increasing the temperature are exactly opposite to those observed by increasing the Ising coefficient. Remarkably, if $\lambda \gg K_B T$, the unfolding of the first unit shows a larger upward force peak since the units are favored to stay in the initial folded state. This upward force peak represents the nucleation stress necessary to generate a new phase (the unfolded one), which is energetically costly because of the Ising interaction. For the same reason, based on cooperativity, the unfolding of the last unit is characterized by a downward force peak. This downward force peak represents the coalescence of the folded phase to the unfolded one. One of the important points of the zipper model is that we can analyze the amplitude of the first peak analytically as discussed below. This is very useful to easily compare its

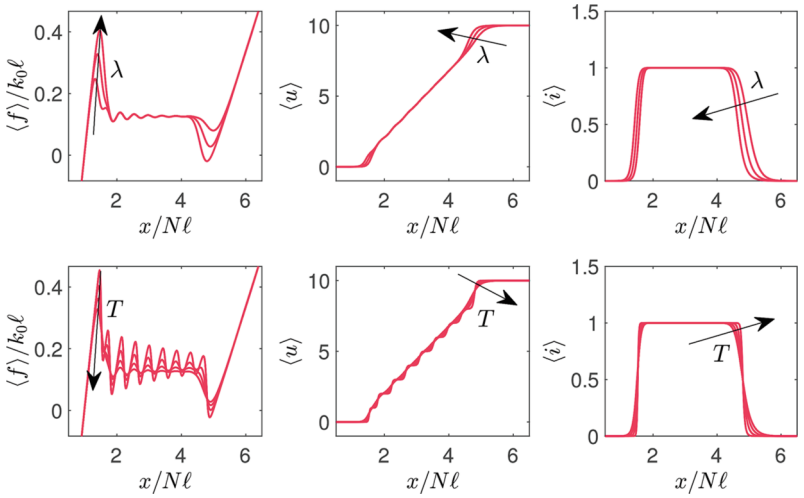

Fig. 3.16 Behavior of the zipper model within the Helmholtz ensemble. In the first row $\langle f\rangle/(k_0\ell)$, $\langle u\rangle$, and $\langle i\rangle$ are plotted versus $x/(N\ell)$ with a variable Ising coefficient $\lambda = \{5, 10, 15\}$ and a fixed temperature $K_BT = 10$. In the second row $\langle f\rangle/(k_0\ell)$, $\langle u\rangle$, and $\langle i\rangle$ are plotted versus $x/(N\ell)$ with a variable temperature $K_BT = \{2, 4, 6, 8\}$ and a fixed Ising coefficient $\lambda = 5$. We adopted the parameters $N = 10$, $k_0 = 30$, $h_0 = 10$, $v(-1) = 0$, $v(+1) = \Delta E = 20$, $\ell = 1$, $\chi = 5$. All quantities are in arbitrary units

value with experiments and numerical simulations. As far as the average number of interfaces is concerned, it is important to observe that it remains constantly at the value one, which is the assumption of the zipper model. This quantity assumes the value zero only when $\xi = 0$ or $\xi = N$, i.e., for very small or very large values of the applied extension x.

We study the thermodynamic limit based on the partition function obtained in Eq. (3.57), concerning the zipper model under isometric condition, i.e., within the Helmholtz ensemble. We can obtain three important results: (i) a simplified expression of the force-extension relation under isometric condition valid for large values of N and for $\lambda \gg K_BT$, (ii) an explicit expression for the amplitude of the first force peak, representing the nucleation of unfolded units, and (iii) a rigorous demonstration of the equivalence of the Gibbs and Helmholtz ensembles for the zipper model. To simplify the discussion we start by defining the adimensional extension $z = \frac{x}{\ell N}$ prescribed for the chain in the Helmholtz ensemble. Long but straightforward calculations lead to the following force-extension response for $1 + \frac{f_M}{\ell k_0} < z < \chi + \frac{f_M}{\ell h_0}$:

$$\langle f\rangle = \frac{C\left[\sqrt{\frac{k_0\ell^2}{2NK_BT}}e^{\mathcal{L}N}(z-1)k_0\ell + \sqrt{\frac{h_0\ell^2}{2NK_BT}}e^{\mathcal{R}N}(z-\chi)h_0\ell\right] + f_M}{C\left[\sqrt{\frac{k_0\ell^2}{2NK_BT}}e^{\mathcal{L}N} + \sqrt{\frac{h_0\ell^2}{2NK_BT}}e^{\mathcal{R}N}\right] + 1}, \tag{3.61}$$

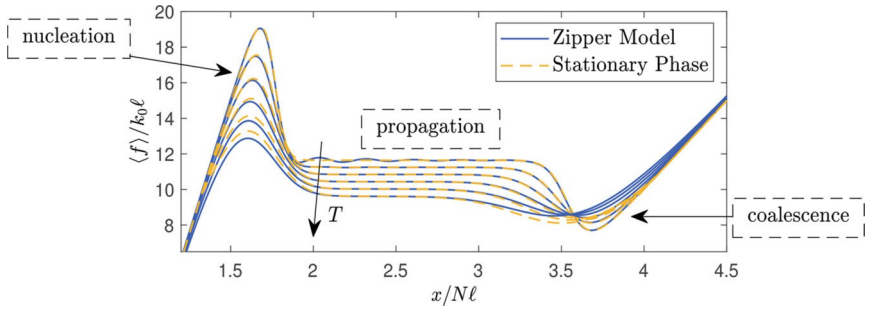

Fig. 3.17 Comparison between the isometric force-extension response of the exact zipper model, obtained by the partition function in Eq. (3.57), and the result of the stationary phase method, stated in Eq. (3.61). We considered different values of the temperature $K_B T = \{4, 6, 8, 10, 12.14\}$ and the parameters $N = 10$, $k_0 = 30$, $h_0 = 10$, $v(-1) = 0$, $v(+1) = \Delta E = 30$, $\ell = 1$, $\chi = 3$, $\lambda = 10$. All quantities are in arbitrary units

where

$$\mathcal{L} = -\frac{1}{2}\frac{\ell^2 k_0}{K_B T}\left(z - 1 - \frac{f_M}{\ell k_0}\right)^2 < 0, \tag{3.62}$$

$$\mathcal{R} = -\frac{1}{2}\frac{\ell^2 h_0}{K_B T}\left(z - \chi - \frac{f_M}{\ell h_0}\right)^2 < 0, \tag{3.63}$$

$$C = \frac{2 - \mathrm{x}^2}{2\sqrt{\pi}\,\mathrm{x}^2}\left[\chi - 1 + \frac{f_M}{\ell}\left(\frac{1}{h_0} - \frac{1}{k_0}\right)\right]. \tag{3.64}$$

The explicit force-extension relation in Eq. (3.61) is particularly important since it represents a simple mathematical form containing all the physical features of the Helmholtz response, including the first nucleation peak and the last coalescence peak. Moreover, this result directly proves that $\lim_{N\to\infty}\langle f \rangle = f_M$ (valid for $1 + \frac{f_M}{\ell k_0} < z < \chi + \frac{f_M}{\ell h_0}$), where f_M is the Maxwell force. It means that in the thermodynamic limit ($N \to \infty$), the force plateau found within the Gibbs ensemble is also reproduced within the Helmholtz ensemble (equivalence of the ensembles in the thermodynamic limit) (Cannizzo et al. 2022).

In Fig. 3.17, we can find the comparison between the isometric force-extension curves obtained through the exact zipper model, whose partition function is stated in Eq. (3.57), and through the stationary phase method, as given in Eq. (3.61). We can observe that the agreement is good also for a rather limited number of units of the chain ($N = 10$ in Fig. 3.17). Moreover, we remark that the stationary phase is able to perfectly reproduce the amplitude of the first peak, representing the nucleation of the new unfolded phase, and that of the last peak, corresponding to the coalescence of the folded region to the unfolded one. We also note the force plateau (describing the domain wall propagation at force f_M), significantly depending on the temperature of the system.

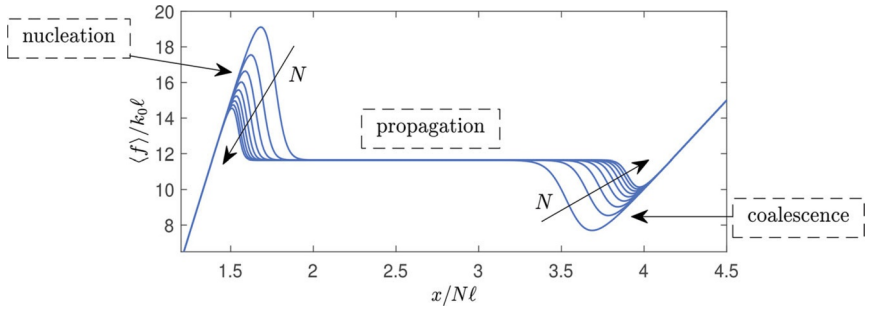

Fig. 3.18 Evolution of the isometric force-extension curve, stated in Eq. (3.61) and obtained by the stationary phase method, with an increasing number N of units. We adopted the parameters $k_0 = 30$, $h_0 = 10$, $v(-1) = 0$, $v(+1) = \Delta E = 30$, $\ell = 1$, $\chi = 3$, $\lambda = 10$, $K_B T = 4$, $N = \{10, 15, 20, \ldots, 50\}$. All quantities are in arbitrary units

In Fig. 3.18, we can see the convergence of the Helmholtz response, as given in Eq. (3.61), for increasing values of N, toward the Gibbs response characterized by a plateau without peaks. This plot provides therefore graphical evidence of the equivalence between the Gibbs and the Helmholtz ensembles. Moreover, we can observe that the characteristic peaks of the isometric response do not appear in the stationary phase approximation except for the first and last, which represent the initial nucleation of the unfolded phase and the final coalescence of the folded phase to the unfolded one, respectively. This means that the force peaks of the intermediate transitions (clearly visible in Fig. 3.16) decrease with increasing N at a much faster rate than the first and last peaks. It can be said that these two peaks resist more when increasing N. This strictly explains why in experiments and simulations on phase transformations in nanowires or other nanostructures it is possible to see only the first nucleation peak (the last peak is more difficult to be observed because the specimen may break or because high levels of deformation are not reached).

Given the importance of the first nucleation force peak, we have found an explicit expression of its magnitude, as follows (Cannizzo et al. 2022):

$$f_P - f_M = \frac{k_0 \ell}{\sqrt{a_0 N}} \frac{\mathrm{W}_0\left(\frac{C}{2}\sqrt{\frac{a_0}{eN}}\right)}{\sqrt{\frac{1}{2} + \mathrm{W}_0\left(\frac{C}{2}\sqrt{\frac{a_0}{eN}}\right)}}, \tag{3.65}$$

where $a_0 = \frac{k_0 \ell^2}{2K_B T}$, C is defined in Eq. (3.64), and we introduced the force peak value f_P. Importantly, through Eq. (3.65), we have the explicit dependence of the peak force on the temperature T and on the number of chain units N.

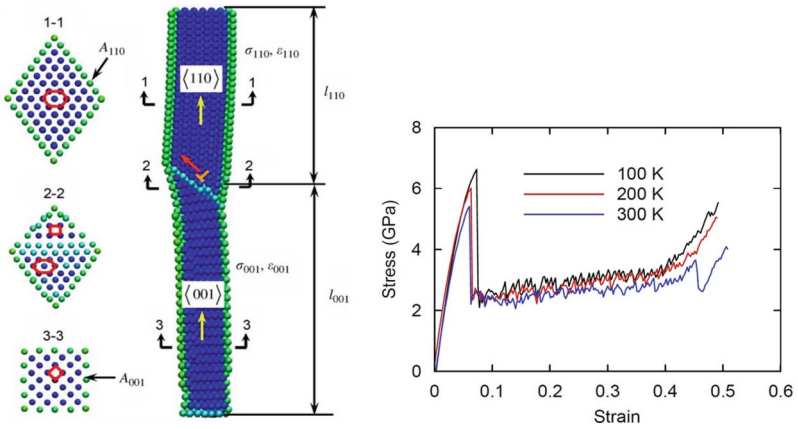

Fig. 3.19 Left panel: cross-sections of a Cu nanowire. Two different crystalline structures can be identified, and they are separated by a domain wall, which is moving in response to the applied strain. Right panel: temperature effect on the stress–strain curves of the Cu nanowire obtained from MD simulations. Both figures are reproduced with permission from Liang et al. (2007)

4.3 Applications to the Tensile Behavior of Nanowires

Recent researches revealed that single-crystalline metal nanowires with nanometric cross-section can exhibit a pseudo-elastic behavior characterized by very large elongations (up to 50% of the original length) (Liang et al. 2007, 2006; Guo et al. 2009; Ma et al. 2013). This behavior, which is exceptional compared to all other shape memory alloys, can be explained by a reversible lattice reorientation process. It means that the deformation mechanism is characterized by a twin boundary propagation between two differently oriented face-centered cubic (FCC) crystalline structures. This behavior is typical of Cu and Ni, where we can identify the following two configurations: the original one named $<110>/\{111\}$ with axis $<110>$ and surfaces $\{111\}$ and the deformed one named $<001>/\{100\}$ with axis $<001>$ and surfaces $\{100\}$, as shown by Liang et al. (2007) (see Fig. 3.19, left panel). Because of the nanometric dimensions of the cross-section geometry, the surface-to-volume ratio is very large, and surface energies dominate the strain energy difference between the two different nanowire configurations.

Our model can be adapted to this system by simply introducing the physical quantities pertinent to continuous structures. We define s as the small area on the cross-section pertaining to a single longitudinal chain of atoms in the nanowire crystal structure. It means that the total area S of the nanowire cross-section is given by $S = Ms$, where M is the average number of atoms in the cross-section. Similarly, ℓ is roughly the lattice constant of the crystal structure and, therefore, $L = N\ell$ is the total nanowire length, being N the number of atoms in the longitudinal direction. It is clear that SL is the total volume of the system, MN is the total number of atoms, and $s\ell$ is the average volume pertaining to one atom. Of course, we have

that $s \simeq \ell^2$ and $s\ell \simeq \ell^3$. It is important to remark that Eq. (3.56), giving the Maxwell force for a chain, and Eq. (3.61), giving the force-extension response in the stationary phase approximation, have been obtained for a single chain of units (here atoms), and therefore the continuous parameters must be introduced as follows. We define $E_f = k_0\ell/s$ [GPa] and $E_u = h_0\chi\ell/s$ [GPa] as the Young moduli of the original and deformed configurations, respectively. In so doing, k_0 and h_0 must be seen as the elastic constants of the two crystals in the harmonic limit. Moreover, the jump energy between the two configurations can be written as $\Delta E = \Delta e s \ell$, where Δe [J/m^3] is the energy density difference between the two crystal states. In addition, the Ising energy can be rewritten as $\lambda = \Lambda s$, where Λ [J/m^2] is the superficial energy density of the twin boundary separating original and deformed crystals. We remark that the parameters Δe and Λ may depend on the total area S when elastic surface effects are relevant, as in the case of metallic nanowires. Of course, the longitudinal stress is defined by $\sigma = \langle f \rangle / s$, with $\langle f \rangle$ given in Eq. (3.61) if we consider the stationary phase approximation. Also, the strain is defined as $\varepsilon = \frac{x - N\ell}{N\ell}$, and therefore we have $\varepsilon = z - 1$ or, equivalently, $z = \varepsilon + 1$. These specifications allow us to use Eq. (3.61), or other previous results, to describe the tensile behavior of one-dimensional continuous structures. For instance, $\delta = 0$ can be rewritten as follows:

$$\frac{1}{2}\ln\left(\frac{E_f}{E_u}\chi\right) + \frac{s\ell}{K_B T}\left[\sigma_M(\chi - 1) + \frac{1}{2}\sigma_M^2\left(\frac{\chi}{E_u} - \frac{1}{E_f}\right) - \Delta e\right] = 0, \tag{3.66}$$

to define the stress Maxwell σ_M. Interestingly, since this equation depends directly on the atomic volume $s\ell$, we can further confirm that the discrete theory previously developed must be applied to a single longitudinal chain of atoms belonging to the entire crystalline nanowire. Similarly, the nucleation stress can be defined as follows:

$$\sigma_P - \sigma_M = \sqrt{\frac{2K_B T E_f}{s\ell N}}\frac{\mathrm{W}_0(\eta)}{\sqrt{\frac{1}{2} + \mathrm{W}_0(\eta)}}, \tag{3.67}$$

where η is defined below:

$$\eta = \frac{2e^{\frac{2\Lambda s}{K_B T}} - 1}{2}\left[\chi - 1 + \sigma_M\left(\frac{\chi}{E_u} - \frac{1}{E_f}\right)\right]\sqrt{\frac{s\ell E_f}{2eNK_B T}}. \tag{3.68}$$

A series of molecular dynamics simulations have been performed to numerically obtain the stress–strain behavior of Cu nanowires at different temperatures and under quasi-static tensile deformation (Liang et al. 2007), which is compatible with our equilibrium statistical mechanics approach (see Fig. 3.19). The simulations are based on the embedded-atom-method interatomic potential for Cu, and the uniaxial displacement-controlled loading strategy is applied coherently with our Helmholtz ensemble. The stress–strain behaviors of a Cu nanowire (1.96 nm $\times$

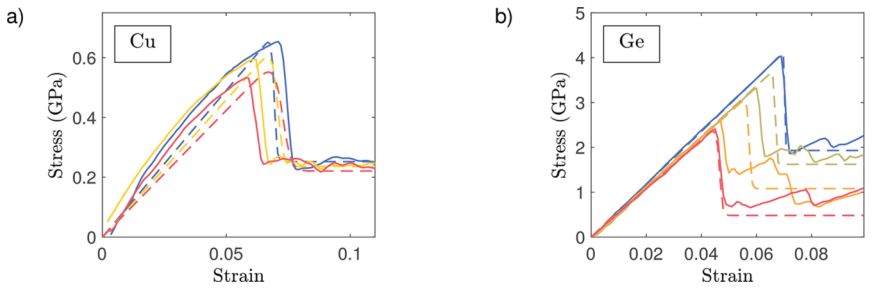

Fig. 3.20 Comparison of the stress–strain curves obtained with molecular dynamic simulations (solid lines) and through our theoretical approach (dashed lines) for Cu nanowires (1.96 nm × 1.96 nm) in panel (**a**) and Ge nanowires (radius of 1.8 Å) in panel (**b**). In panel (**a**) we used the temperatures T=100 K (blue lines), T=200 K (yellow lines), and T=300 K (red lines). In panel (**b**) we used the temperatures T=100 K (blue lines), T=200 K (green lines), T=300 K (yellow lines), and T=400 K (red lines)

1.96 nm) at temperatures of 100, 200, and 300 K have been therefore obtained and are compared with our model in Fig. 3.20a. The theoretical results are based on the stationary phase approximation stated in Eq. (3.61). As one can see, the model is able to reproduce the magnitude of both the nucleation stress and the Maxwell stress plateau. We adopted the parameters $N = 206$, $\ell = 0.14$ nm, $s = \ell^2$, $\chi = 4.4$, coherently with data taken from Liang et al. (2007). Moreover, we used a folded Young modulus slightly temperature dependent given by $E_f = 122$ GPa for T=100 K, $E_f = 114$ GPa for T=200 K, and $E_f = 105$ GPa for T=300 K. For the unfolded Young modulus we used $E_u = 10$ GPa for T=100 K, $E_u = 11$ GPa for T=200 K, and $E_u = 12$ GPa for T=300 K. By introducing the parameterizations $\Delta e = \gamma \frac{K_B T_0}{s\ell}$ and $\Lambda = \delta \frac{K_B T_0}{s}$ with $T_0 = 300$ K, we obtained the adimensional values $\gamma = 7.7$ and $\delta = 6.8$. Since δ is sufficiently larger than 1, the use of the zipper model, simplified by the stationary phase method, is justified.

We now turn to the study of a second example. Semiconductor nanowires have been recently studied since their properties are sometimes more interesting than those of the bulk counterpart (Yang et al. 2016). For this reason, the thermomechanical properties of ultrathin germanium nanowires have been investigated by means of molecular dynamics simulations (Yang et al. 2016). We consider here the results concerning the helix Ge nanowire with radius of 1.8 Å, for which the stress–strain curve has been obtained for temperatures of 100, 200, 300, and 400 K (Yang et al. 2016). The simulations for germanium were based on the Stillinger–Weber potential, coupled with the Nosé–Hoover thermostat to impose the system temperature. The comparison of molecular dynamics results with our model is shown in Fig. 3.20b. Again, nucleation stresses and Maxwell stresses are in fairly good agreement. The helical structure is perfectly ordered initially, as shown in Fig. 1 from Yang et al. (2016), and exhibits a transition to an amorphous structure, as shown in Fig. 5 from Yang et al. (2016), following a plastic process that begins with a peak of stress, namely the nucleation stress. After the yielding strain, the unfolded

region evolves into the one-atom chain structure. In our theoretical formulation, we adopted the parameters $N = 5562$, $\ell = 0.208$ nm, $s = \ell^2$, $\chi = 3.36$, coherently with data from Yang et al. (2016). Moreover, we used a folded Young modulus slightly temperature dependent given by $E_f = 588$ GPa for $T = 100$ K, $E_f = 561$ GPa for $T = 200$ K, $E_f = 552$ GPa for $T = 300$ K, and $E_f = 540$ GPa for $T = 400$ K. For the unfolded Young modulus we used $E_u = 23$ GPa for $T = 100$ K, $E_u = 43$ GPa for $T = 200$ K, $E_u = 63$ GPa for $T = 300$ K, and $E_u = 83$ GPa for $T = 400$ K. By introducing the parameterizations $\Delta e = \gamma \frac{K_B T_0}{s\ell}$ and $\Lambda = \delta \frac{K_B T_0}{s}$ with $T_0 = 300$ K, we obtained the adimensional values $\gamma = 2.3$ and $\delta = 25.3$. As before, $\delta \gg 1$ justifies the use of the zipper model, simplified by the stationary phase method.

In the two examples discussed, we considered systems where two possible states or configurations are present. In the first example they correspond to two different crystal structures and in the second example to a regular helical structure and an irregular amorphous structure. It is interesting to note that the model based on statistical mechanics that we have developed is able, at least approximately, to represent the behavior of such systems. The important thing to underline is that in our model there is no crystallographic or morphological information of the three-dimensional structures but only some elastic and energetic properties of the system. For this reason the model is able to summarize the physics of these systems without being able to describe the microstructural details. Of course, if it is necessary to take into account crystallographic details, structural anisotropies, twin-boundary geometries, and other morphological features, then it is necessary to turn to another class of models that are specifically adapted to the problem at hand, such as, e.g., the model by Liang et al. (2007) for the pseudo-elasticity of metallic nanowires.

5 Adhesion/Deadhesion Processes: Application to Hairpins Unzipping

We discuss here the modeling of the adhesion/deadhesion process of a film or a layer deposited on a substrate. We schematize this process by considering a one-dimensional elastic chain of elements embedded in an on-site potential reproducing the behavior of breakable links. We approach the problem by considering the effect of thermal fluctuations, which play a central role in the decohesion behavior of biological materials. Therefore, we apply the equilibrium statistical mechanics and the spin variables method by considering the scheme in Fig. 3.1 (second panel). This scheme, as discussed in the Introduction section, can be used to study the adhesion of cells on substrates or tissues, the temperature controlled hairpins unzipping, or the mechanical/thermal denaturation of different macromolecules of biological origin (Florio et al. 2020).

We introduce the adopted geometry, as shown in Fig. 3.21. The horizontal springs of the one-dimensional lattice (elastic constant k) are purely harmonic with potential

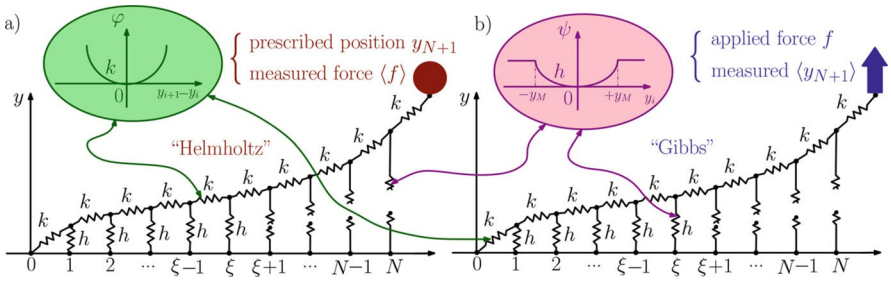

Fig. 3.21 Energy landscapes of the harmonic (horizontal) shear springs in panel (**a**) and breakable (vertical) links in panel (**b**). Different loading conditions are considered: assigned end displacement (Helmholtz ensemble, hard device) on the left and assigned force (Gibbs ensemble, soft device) on the right

energy $\varphi = \frac{1}{2}k\,(y_{i+1} - y_i)^2$ (Fig. 3.21a), while the vertical ones (elastic constant h) can be broken or unbroken depending on their extension y_i (Fig. 3.21b). When $|y_i| < y_M$, they behave as regular springs (intact state), and they break for $|y_i| > y_M$ (broken state). Therefore, an unbroken or intact spring leads to a contribution to the potential energy equal to $\psi = \frac{1}{2}hy_i^2$ (when $|y_i| < y_M$) and a broken one a contribution equal to $\psi = \frac{1}{2}hy_M^2$ (when $|y_i| > y_M$). As before, two different loading conditions are considered. In the first case (Fig. 3.21a), the process is controlled by the prescribed position $y_{N+1} = y_d$ of the last element of the chain (isometric condition within the Helmholtz ensemble). In the second case (Fig. 3.21b), the process is controlled by the applied force f (isotensional condition within the Gibbs ensemble). The most important point, on which is grounded our approach, is that each vertical element is characterized by two different states (broken and unbroken configurations). Therefore, we associate each unit with a spin variable, and the energy potential of each vertical spring can be written as

$$\psi = \frac{1}{4}(1 + s_i)hy_i^2 + \frac{1}{4}(1 - s_i)hy_M^2, \tag{3.69}$$

where $s_i = +1$ corresponds to the unbroken state and $s_i = -1$ corresponds to the broken state, $i = 1, \ldots, N$. With this assumptions we have a phase space composed of the N continuous variables y_i and the N discrete variables s_i. The switching of the variable s_i and their statistics at thermodynamic equilibrium are directly controlled by the statistical ensemble (Helmholtz and Gibbs in our case) imposed to the system.

In order to simplify the statistical mechanics analysis of this system, we assume to have $N - \xi$ broken elements on the right of the chain and ξ unbroken elements on the left of the chain. In other words we are supposed to have a single moving interface or domain wall between the attached region and the detached region. As before, this hypothesis coincides with the so-called zipper model (Gibbs et al. 1959; Crothers et al. 1965; Kittel 1969; Nishinari et al. 1990). Under these hypotheses, we use a single discrete variable ξ belonging to the phase space of the system and

taking its values in the set $\{0, 1, 2, \ldots, N\}$. We separately analyze the cohesion–decohesion process in Helmholtz and Gibbs ensembles, thus providing a complete picture of the effect of temperature and mechanical load on this physical system.

5.1 Hard Device Adhesion/Deadhesion: Helmholtz Ensemble

Consider first the case of a prescribed extension $y_{N+1} = y_d$ of the last element of the chain, as represented in Fig. 3.21a (isometric condition). The variables belonging to the phase space are the extensions y_i of the vertical springs ($i = 1, \ldots, N$) and the number ξ of unbroken links. The total potential energy is

$$\Phi = \sum_{i=0}^{N} \frac{1}{2} k \left(y_{i+1} - y_i\right)^2 + \sum_{i=1}^{\xi} \frac{1}{2} h y_i^2 + \sum_{i=1+\xi}^{N} \frac{1}{2} h y_M^2, \tag{3.70}$$

where $y_0 = 0$ and $y_{N+1} = y_d$ with isometric condition. It is worth noticing that the last term in Φ is not an irrelevant additive constant since it depends implicitly on ξ, which is a variable of the phase space of the system. The energy function Φ can be rearranged by means of the following matrix definition:

$$\mathcal{A}(\xi) = \begin{bmatrix} \mathcal{A}_{11} & \mathcal{A}_{12} \\ \mathcal{A}_{21} & \mathcal{A}_{22} \end{bmatrix} \in \mathcal{M}_{N,N}, \tag{3.71}$$

which is based on these four submatrices

$$\mathcal{A}_{11} = \begin{bmatrix} 2+\eta & -1 & 0 & \cdots \\ -1 & 2+\eta & -1 & \cdots \\ 0 & -1 & 2+\eta & \cdots \\ \vdots & \vdots & \vdots & \ddots \end{bmatrix} \in \mathcal{M}_{\xi,\xi}, \mathcal{A}_{22} = \begin{bmatrix} 2 & -1 & 0 & \cdots \\ -1 & 2 & -1 & \cdots \\ 0 & -1 & 2 & \cdots \\ \vdots & \vdots & \vdots & \ddots \end{bmatrix} \in \mathcal{M}_{N-\xi,N-\xi},$$

$$\mathcal{A}_{12} = \begin{bmatrix} 0 & \cdots & 0 & 0 \\ 0 & \cdots & 0 & 0 \\ 0 & \iddots & \vdots & \vdots \\ -1 & 0 & 0 & 0 \end{bmatrix} \in \mathcal{M}_{N,N-\xi}, \mathcal{A}_{21} = \begin{bmatrix} 0 & 0 & 0 & -1 \\ \vdots & \vdots & \iddots & 0 \\ 0 & 0 & \cdots & 0 \\ 0 & 0 & \cdots & 0 \end{bmatrix} \in \mathcal{M}_{N-\xi,N}, \tag{3.72}$$

where $\eta = \frac{h}{k}$ represents the ratio between the elastic constants of vertical and horizontal elastic elements. Moreover, we introduce the vectors $\boldsymbol{v} = (0, 0, 0, \ldots, 0, 1) \in \mathbb{R}^N$ and $\boldsymbol{y} = (y_1, y_2, y_3, \ldots, y_N) \in \mathbb{R}^N$. The energy function can then be rewritten as follows:

$$\Phi\left(\boldsymbol{y}, \xi; y_d\right) = \frac{1}{2} k \mathcal{A}(\xi) \boldsymbol{y} \cdot \boldsymbol{y} - k y_d \boldsymbol{v} \cdot \boldsymbol{y} + \frac{1}{2} k y_d^2 + \frac{1}{2} k \eta (N - \xi) y_M^2, \tag{3.73}$$

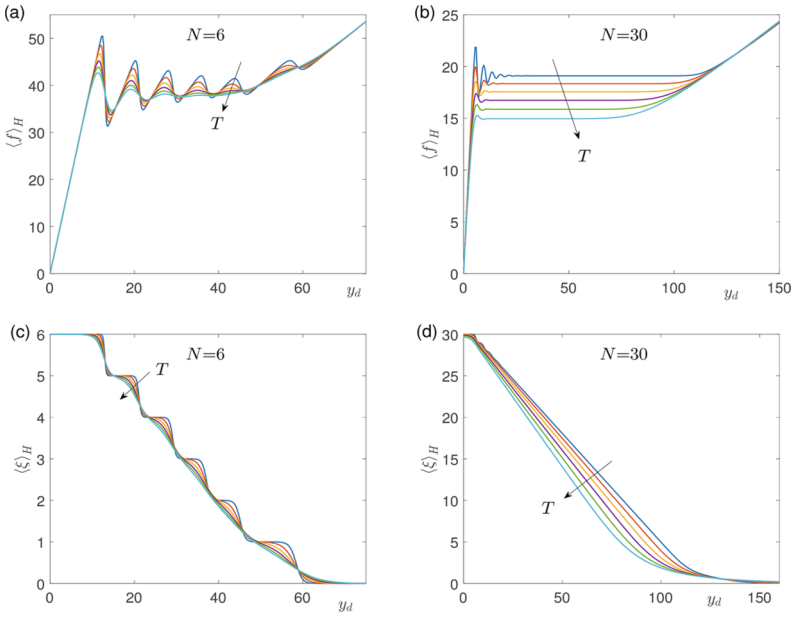

Fig. 3.22 Average force $\langle f \rangle_H$ in top panels (**a**) and (**b**), and average number of unbroken elements $\langle \xi \rangle_H$ in bottom panels (**c**) and (**d**), versus y_d for a decohesion process (y_d increasing) under isometric conditions (Helmholtz ensemble). We adopted the parameters $N = 6$ and $y_M = 4$ for panels (**a**) and (**c**) and $N = 30$ and $y_M = 2$ for panels (**b**) and (**d**). Other parameters are common: $k = 5$, $h = 20$, and six values of $\beta^{-1} = k_B T = 4, 7.2, 10.4, 13.6, 16.8$, and 20 (in arbitrary units)

where $\boldsymbol{y}$ and ξ are the main variables belonging to the phase space of the system. This expression of Φ is useful in the following Gaussian integration for the partition function since it is constituted by the sum of a quadratic form and a linear form in $\boldsymbol{y}$, with an additional term independent of $\boldsymbol{y}$.

The partition function of the system analyzed within the Helmholtz ensemble can therefore be written as

$$Z_H(\beta, y_d) = \sum_{\xi=0}^{N} \int_{\mathbb{R}^N} e^{-\beta \Phi(\boldsymbol{y}, \xi; y_d)} d\boldsymbol{y}, \tag{3.74}$$

where $\beta = (k_B T)^{-1}$, k_B is the Boltzmann constant and T the absolute temperature. When Eq. (3.73) is substituted in Eq. (3.74), we get (Florio et al. 2020)

$$Z_H(\beta, y_d) = \left(\frac{2\pi}{\beta k}\right)^{N/2} e^{-N\beta \frac{k y_M^2}{2} \eta} \sum_{\xi=0}^{N} \Gamma_\xi(\beta, y_d), \tag{3.75}$$

where

$$\Gamma_\xi(\beta, y_d) = \frac{e^{\beta \frac{ky_M^2}{2} \eta \xi}}{\sqrt{\det \mathcal{A}(\xi)}} e^{-\beta \frac{ky_d^2}{2} \left\{1 - \mathcal{A}_{NN}^{-1}(\xi)\right\}}. \tag{3.76}$$

The knowledge of the partition function allows us to determine the expectation value of the force conjugated to the assigned displacement y_d (Weiner 2002)

$$\langle f \rangle_H = -\frac{1}{\beta} \frac{\partial \ln Z_H}{\partial y_d} = \left(1 - \frac{\sum_{\xi=0}^{N} \mathcal{A}_{NN}^{-1}(\xi)\, \Gamma_\xi(\beta, y_d)}{\sum_{\xi=0}^{N} \Gamma_\xi(\beta, y_d)}\right) k\, y_d. \tag{3.77}$$

Another important quantity to describe the decohesion process is the average value $\langle \xi \rangle_H$ of unbroken vertical springs. It can be directly evaluated through the expression

$$\langle \xi \rangle_H = \frac{1}{Z_H} \sum_{\xi=0}^{N} \int_{\mathbb{R}^N} \xi e^{-\beta \Phi(\boldsymbol{y}, \xi; y_d)} d\boldsymbol{y} = \frac{\sum_{\xi=0}^{N} \xi\, \Gamma_\xi(\beta, y_d)}{\sum_{\xi=0}^{N} \Gamma_\xi(\beta, y_d)}. \tag{3.78}$$

These explicit formulas give the quantities $\det \mathcal{A}(\xi)$ and $1 - \mathcal{A}_{NN}^{-1}(\xi)$ (Florio et al. 2020)

$$\det \mathcal{A}(\xi) = (N - \xi + 1)\gamma(\xi + 1) - (N - \xi)\gamma(\xi), \tag{3.79}$$

$$1 - [\mathcal{A}(\xi)]_{NN}^{-1} = \frac{\gamma(\xi + 1) - \gamma(\xi)}{(N - \xi + 1)\gamma(\xi + 1) - (N - \xi)\gamma(\xi)}, \tag{3.80}$$

where the function $\gamma(z)$ is defined as follows:

$$\gamma(z) = \frac{1}{\sqrt{\Delta}} \left(\frac{2 + \eta + \sqrt{\Delta}}{2}\right)^z - \frac{1}{\sqrt{\Delta}} \left(\frac{2 + \eta - \sqrt{\Delta}}{2}\right)^z, \tag{3.81}$$

with $\Delta = \eta^2 + 4\eta$.

In Fig. 3.22 we illustrate the obtained behavior for a system under isometric loading for a "short" chain with only $N = 6$ elements and for a "long" chain with $N = 30$ elements. The case with $N = 6$, in left panels (a) and (c) of Fig. 3.22, shows the importance of discreteness, exhibiting distinct rupture occurrences in the decreasing steps of the quantity $\langle \xi \rangle_H$, and in the peaks of the force-displacement ($\langle f \rangle_H$, y_d) curves along the whole decohesion process. As expected, for large values of the temperature T the curves are smoother, and it is more difficult to recognize the single ruptures. The case with a larger number of elements ($N = 30$) is represented in the right panels (b) and (d) of Fig. 3.22. We observe that the system is initially characterized by some force oscillations corresponding to the first debonding effects, but the force curves rapidly converge to a constant force plateau.

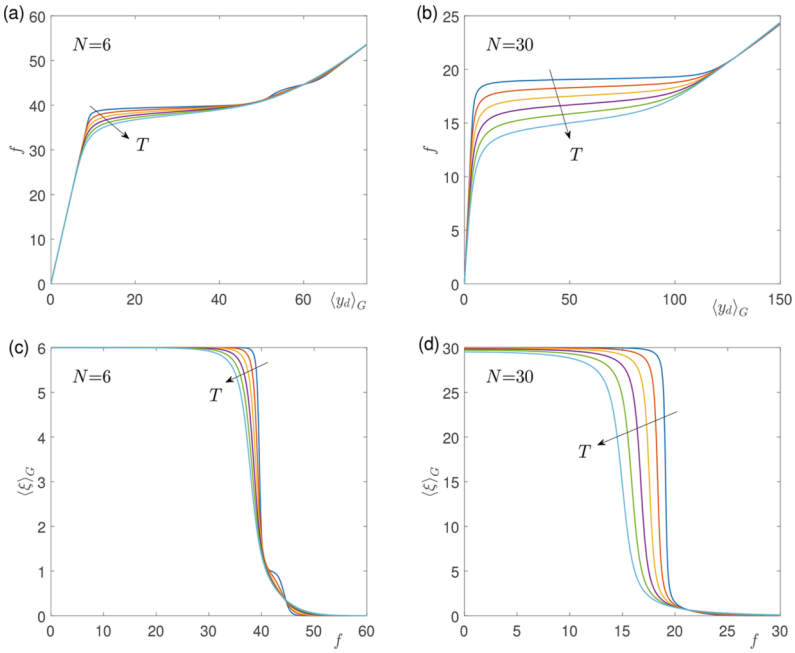

Fig. 3.23 Average position $\langle y_d \rangle_G$ in top panels (**a**) and (**b**), and average number of unbroken elements $\langle \xi \rangle_G$ in bottom panels (**c**) and (**d**), versus f for a decohesion process (f increasing) under isotensional conditions (Gibbs ensemble). We adopted the parameters $N = 6$ and $y_M = 4$ for panels (**a**) and (**c**) and $N = 30$ and $y_M = 2$ for panels (**b**) and (**d**). Other parameters are common: $k = 5$, $h = 20$, and six values of $\beta^{-1} = k_B T = 4, 7.2, 10.4, 13.6, 16.8$, and 20 (in arbitrary units)

The increase of temperature strongly reduces also this initial discreteness effect. The main interesting feature is the observation of the temperature dependent unfolding plateau, with a detachment force threshold sensibly decreasing as the temperature grows.

5.2 Soft Device Adhesion/Deadhesion: Gibbs Ensemble

We consider now the case when the film is detached by a fixed force f as in Fig. 3.21b (isotensional condition). In this case, we introduce the Gibbs ensemble of the statistical mechanics. The total energy of the system can now be written as $\Phi - f y_{N+1}$, where Φ is the energy function introduced within the Helmholtz ensemble in Eq. (3.73). Hence, the Gibbs partition function can be written as

$$Z_G(f) = \int_{\mathbb{R}^{N+1}} \sum_{\xi=0}^{N} e^{-\beta\Phi(\boldsymbol{y},\xi;y_{N+1})} e^{\beta f y_{N+1}} d\boldsymbol{y} dy_{N+1}$$
$$= \int_{-\infty}^{+\infty} Z_H(y_{N+1})\, e^{\beta f y_{N+1}} dy_{N+1}. \tag{3.82}$$

Of course this corresponds to the Laplace transform of the Helmholtz partition function (Weiner 2002). By using Eqs. (3.75) and (3.76), we get (Florio et al. 2020)

$$Z_G(f) = \left(\frac{2\pi}{\beta k}\right)^{\frac{N+1}{2}} e^{-N\frac{\beta k y_M^2}{2}\eta} \sum_{\xi=0}^{N} \Omega_\xi(\beta, f), \tag{3.83}$$

where

$$\Omega_\xi(\beta, f) = \frac{e^{\beta\frac{k y_M^2}{2}\eta\xi} e^{\beta\frac{f^2}{2k}\left\{1-\mathcal{A}_{NN}^{-1}(\xi)\right\}^{-1}}}{\sqrt{\det\mathcal{A}(\xi)\left\{1-\mathcal{A}_{NN}^{-1}(\xi)\right\}}}. \tag{3.84}$$

The expected value of the extension $\langle y_d\rangle = \langle y_{N+1}\rangle$ of the last element can be evaluated as (Weiner 2002)

$$\langle y_d\rangle_G = \frac{1}{\beta}\frac{\partial \ln Z_G}{\partial f} = \frac{\sum_{\xi=0}^{N}\left\{1-\mathcal{A}_{NN}^{-1}(\xi)\right\}^{-1}\Omega_\xi(\beta, f)}{\sum_{\xi=0}^{N}\Omega_\xi(\beta, f)}\frac{f}{k}. \tag{3.85}$$

Similarly, we can also determine the average number of unbroken links

$$\langle\xi\rangle_G = \frac{1}{Z_G}\int_{\mathbb{R}^{N+1}} \sum_{\xi=0}^{N} \xi e^{-\beta\Phi(\boldsymbol{y},\xi;y_{N+1})} e^{\beta f y_{N+1}} d\boldsymbol{y} dy_{N+1}$$
$$= \frac{\sum_{\xi=0}^{N}\xi\,\Omega_\xi(\beta, f)}{\sum_{\xi=0}^{N}\Omega_\xi(\beta, f)}. \tag{3.86}$$

The obtained results for the isotensional loading are illustrated in Fig. 3.23 for the same chains considered in Fig. 3.22, where the case of isometric loading was described. Important differences between the Helmholtz and the Gibbs responses can be recognized. In particular, the analysis of the evolution of $\langle\xi\rangle_G$ within the Gibbs ensemble shows that the detachment process corresponds to a cooperative breaking of the vertical elements. This result can be compared with the sequential unfolding behavior, observed with an extension controlled decohesion, obtained with the hard device. Another important difference concerns the shape of the force-extension curves measured within the two statistical ensembles. While the

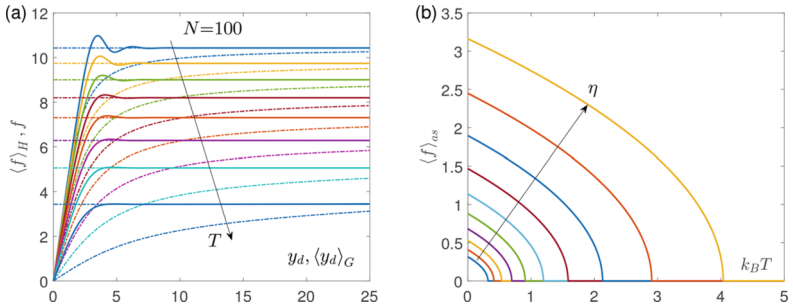

Fig. 3.24 Panel (**a**): comparison between the Helmholtz force-extension curves ($\langle f \rangle_H$ versus y_d, solid lines) and the Gibbs force-extension curves (f versus $\langle y_d \rangle_G$, dashed lines) proving the nonequivalence of the two statistical ensembles in the thermodynamic limit. The results are obtained for a discrete system with $N = 100$ based on Eqs. (3.77) and (3.85). Panel (**b**): critical behavior of the asymptotic force within the Helmholtz ensemble. We plotted $\langle f \rangle_{as}$ versus $k_B T = \beta^{-1}$ (see Eq. (3.87)) for different values of the ratio $\eta = h/k$ between the elastic constants of the vertical and horizontal elements. Here $k = 1$, $y_M = 1$ (in arbitrary units), and we plotted ten curves with $1/10 \leq \eta \leq 10$

isometric case leads to a series of peaks corresponding to the rupture occurrences, the isotensional case is characterized by a monotone force-extension curve. Also this feature can be explained by the quite simultaneous rupture of all the elements observed within the Gibbs ensemble. Finally, the temperature dependent force plateau corresponding to the detachment can be observed in both Helmholtz and Gibbs ensembles.

5.3 *Thermodynamic Limit*

In this section, we study the behavior of the system, under both isometric and isotensional conditions, for a large chain length (ideally, $N \to \infty$), and we obtain explicit analytic results to describe the system behavior in the thermodynamic limit.

A refined mathematical analysis of the problem leads to the following value of the asymptotic detachment force for both statistical ensembles (Florio et al. 2020):

$$\langle f \rangle_{as} = \lim_{y_d \to \infty} \langle f \rangle_H = \sqrt{kh}\, y_M \sqrt{1 - \frac{T}{T_c}}, \tag{3.87}$$

where we introduced the critical temperature

$$T_c = \frac{h y_M^2}{k_B \ln \frac{2+\eta+\sqrt{\eta^2+4\eta}}{2}}. \tag{3.88}$$

This formula describes the asymptotic value of the force plateau (large value of N and of the extension of the last element of the chain) in terms of the temperature and the material parameters of the system. Therefore, it is the main important result describing the adhesion/deadhesion process.

The result is illustrated in Fig. 3.24a, where the force displacement relation is plotted for different values of the temperature. In particular, we compare the force-displacement response of a discrete system with $N = 100$ elements given by Eq. (3.77) (Helmholtz, colored continuous curves) with the result of Eq. (3.85) (Gibbs, colored dashed curves). Moreover, in Fig. 3.24a, we also reported the asymptotic value of the decohesion force provided by Eq. (3.87) (horizontal straight lines). In any case, the asymptotic result given in Eq. (3.87) is in perfect agreement with the numerical result obtained with a discrete system analyzed through Eq. (3.77) or Eq. (3.85). Although the asymptotic behavior is the same, the difference between the curves in the two ensembles proves the nonequivalence of the Gibbs and Helmholtz condition for the adhesion processes. Moreover, Fig. 3.24 explains the variation of the plateau force with the temperature in terms of a phase transition occurring at the critical temperature T_c. Indeed, in Fig. 3.24b, we plot the obtained temperature dependent value of the asymptotic unfolding force for different values of the nondimensional parameter η. We note that the force approaches zero at the critical temperature T_c and that T_c is an increasing function of the ratio η. We therefore conclude that for $T \to T_c$ we have a phase transition corresponding to the rupture of all the vertical elements of the chain, i.e., to the complete detachment of the chain from the substrate. For this reason, the critical temperature can also be referred to as the denaturation temperature of the system, as frequently adopted in the biological context (Peyrard et al. 1989; Theodorakopoulos et al. 2004; Grinza et al. 2004). The decreasing trend of the peeling force with the temperature is the same for both statistical ensembles. However, these ensembles are nonequivalent in the thermodynamic limit since they show a different force-extension curve. In particular, the force-extension curve for the Helmholtz case is characterized by a force peak followed by some oscillations before reaching the asymptotic force value. On the contrary, the force-extension curve for the Gibbs case is always monotonically increasing from zero to the asymptotic force value.

5.4 Application to Nucleic Acid Hairpins

Recently, the mechanical unfolding of nucleic acid hairpins has been experimentally and numerically investigated in order to determine the phase diagram in the force-temperature plane (Hyeon et al. 2005; Mishra et al. 2011). Hairpins are closed loops composed of nucleobases of DNA or RNA as shown in Fig. 3.25. The force spectroscopy techniques are applied to measure the force necessary to open the hairpin structures. Since the geometry of the hairpins experiments is very similar to the one adopted in the previous investigation concerning adhesion/deadhesion processes, and because of the generality of our results, we can show here the

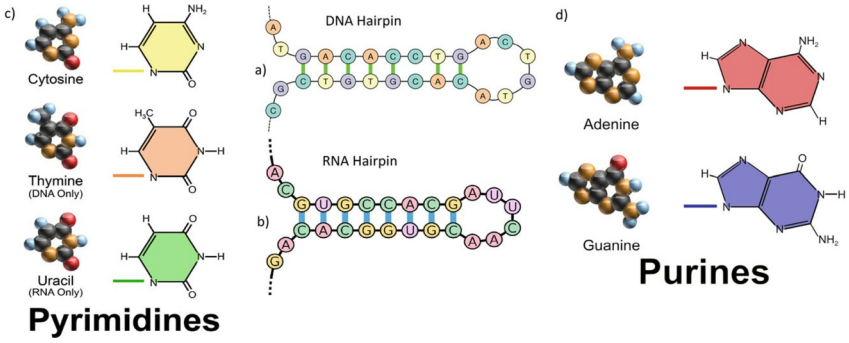

Fig. 3.25 Hairpin structures. (**a**) DNA hairpin example composed of C, T, A, and G bases. (**b**) RNA hairpin example composed of C, U, A, and G bases. (**c**) Pyrimidine nucleobases cytosine (C), thymine (T), and uracil (U) consist of simple ring molecules. (**d**) Purine nucleobases adenine (A) and guanine (G) consist of fused-ring molecules. The images are adapted from Wikipedia under CC BY 3.0 license

comparison between experimental and theoretical findings. In particular, the theory previously developed can be applied to give a theoretical interpretation of the experimental results obtained through the unfolding of RNA and DNA hairpins by optical–thermal tweezers (Stephenson et al. 2014; De Lorenzo et al. 2015). Concerning RNA, the unfolding of a 20-base-pair tetraloop hairpin was studied under different ionic conditions and at temperatures ranging from 22 °C to 42 °C (Stephenson et al. 2014). Aluminum heating plates with thermoelectric coolers have been used to heat the system, and the temperature has been measured by a thin thermocouple. At each temperature, single hairpin molecules have been held at constant force (Gibbs ensemble), and the transition force has been measured versus the controlled temperature of the experiment (see Fig. 3.26, top right panel). The experimental data are also plotted in Fig. 3.26 (bottom panel, red down-pointing triangles) together with the theoretical curve obtained through Eqs. (3.87) and (3.88), with $k = 0.6\,\mathrm{N/m}$, $h = 86.3\,\mathrm{N/m}$, and $y_M = 7.77\,\mathrm{pm}$. Concerning DNA, a 6.8 kbp hairpin obtained from λ-DNA has been used in a temperature-jump optical trap for single-molecule manipulation (De Lorenzo et al. 2015). In this case the temperature is controlled by a heating laser with a wavelength highly absorbed by water in order to have a quite broad range of temperatures between 5 °C and 50 °C (see Fig. 3.26, top left panel). The resulting transition force is also plotted in Fig. 3.26 (bottom panel, blue up-pointing triangles) against the theoretical curve obtained, as before, through Eqs. (3.87) and (3.88), and now with $k = 1\,\mathrm{N/m}$, $h = 5.34\,\mathrm{N/m}$, and $y_M = 19.5\,\mathrm{pm}$. In Fig. 3.26, bottom panel, we also added a green square symbol corresponding to the measured denaturation temperature of DNA (here also assumed for RNA) (Wang et al. 2014; Wallace et al. 1979). We remark however that the denaturation temperature is rather sensible to the solvent conditions and the base composition of the nucleic acids (Marmur et al. 1962). The value $k = 1\,\mathrm{N/m}$ for DNA has been imposed since a Young modulus of 300 MPa has been

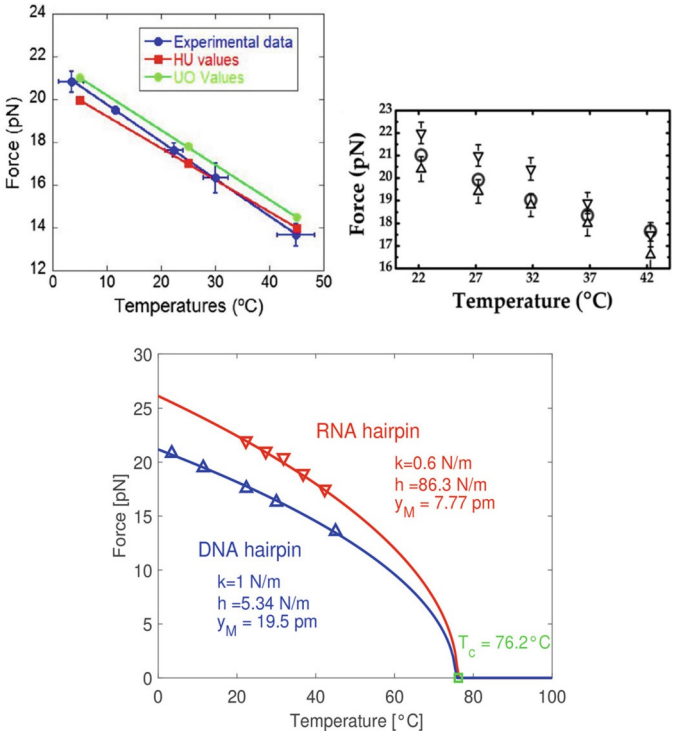

Fig. 3.26 Top left panel: DNA hairpin unfolding experimental data, reproduced with permission (De Lorenzo et al. 2015). The experimental data (blue points) are compared with two theoretical predictions, HU and UO, described by De Lorenzo et al. (2015). Top right panel: RNA hairpin unfolding experimental data, reproduced with permission (Stephenson et al. 2014). The down-pointing triangles correspond to the unfolding, the up-pointing triangles to the refolding, and the circles to the equilibrium force (at which the unfolding and refolding rate constants are equal). Bottom panel: comparison between experimental results for the unzipping of RNA and DNA hairpins. Red down-pointing triangles: RNA hairpins (Stephenson et al. 2014), and blue up-pointing triangles: DNA hairpins (De Lorenzo et al. 2015). Both sets of results are shown in the first two panels, and our theoretical predictions are here represented by continuous lines. The green square symbol corresponds to a measurement of the denaturation temperature (Wang et al. 2014; Wallace et al. 1979)

estimated for the linear elasticity of DNA (Marko et al. 2003). Indeed, by assuming a Young modulus $E = 300\,\text{MPa}$, a DNA radius $r = 1\,\text{nm}$, and a distance between base pairs $\ell = 0.34\,\text{nm}$, we easily obtained $k = \pi r^2 E/\ell \simeq 1\,\text{N/m}$. Concerning the RNA stretching modulus, we adopted the value $k = 0.6\,\text{N/m}$ since calculations and experiments indicate that the stretch modulus of dsDNA is nearly twofold larger than that of dsRNA (Bao et al. 2017; Marin-Gonzalez et al. 2017). The different mechanical behaviors of DNA and RNA are thoroughly explained in the recent literature (Bao et al. 2017; Marin-Gonzalez et al. 2017). The other parameters (h and y_M) have been fitted to obtain a good agreement between experimental and

theoretical results for both RNA and DNA hairpins. It is interesting to note that the curves are able to jointly represent both the experimental data with the applied force at different temperatures (Stephenson et al. 2014; De Lorenzo et al. 2015) and the measurements concerning the denaturation temperature (Wang et al. 2014; Wallace et al. 1979). Moreover, the obtained values of h are larger than k, coherently with other DNA models based on the Morse potential (Peyrard 2004). To conclude, also the values of the extension threshold y_M are reasonable being lesser than the distance between base pairs $\ell = 0.34$ nm, which is a characteristic length for nucleic acids.

6 Adhesion/Deadhesion Processes with Softening Mechanism: Application to Fracture

In this section, we generalize the previous adhesion/deadhesion problem by introducing an intermediate state between the intact and broken states of the vertical elements. We suppose that before the complete breaking there is a phase of softening where the vertical elements assume a reduced elastic stiffness with respect to its intact value (Cannizzo et al. 2021). This model is particularly useful to represent the behavior of materials in terms of fracture strength. It is in fact important to underline that the process of deadhesion is very similar to the process of fracture: In both cases there is a sequence of links which break progressively in response to the external mechanical action and the temperature. Of course, assuming that the two processes can be modeled by means of the same scheme is an approximation and more in-depth studies are in progress. Anyway, we suppose here that we can also use deadhesion geometry for the fracture problem. An important problem in material science, and in particular in mechanics of materials, is the determination of the properties of structures at elevated temperature. One of the most important quantities is represented by the fracture strength, whose high-temperature behavior is crucial for construction and building materials for obvious reasons of stability and security. On the one hand, some investigation has been performed on the development of models capable of describing the temperature dependent fracture strength of materials (Nemat-Nasser et al. 1999; Li et al. 2016; Neuenschwander et al. 2017a). On the other hand, in several experiments the strength versus temperature response has been measured for many materials including metals, ceramics, and thermoplastic polymers (Neuenschwander et al. 2017b; Cheng et al. 2020; Huang et al. 2020). The proposed approach represents therefore a conceptual step forward in the understanding of the strength–temperature relationship. As anticipated, the temperature dependent deadhesion model is applied to describe the fracture propagation in the sample under mechanical load. In particular, our model is able to describe the strength behavior in some specific cases where a given transition occurs during the increasing of the deformation (represented by the softening mechanism). Importantly, the model is able to reproduce the high-temperature

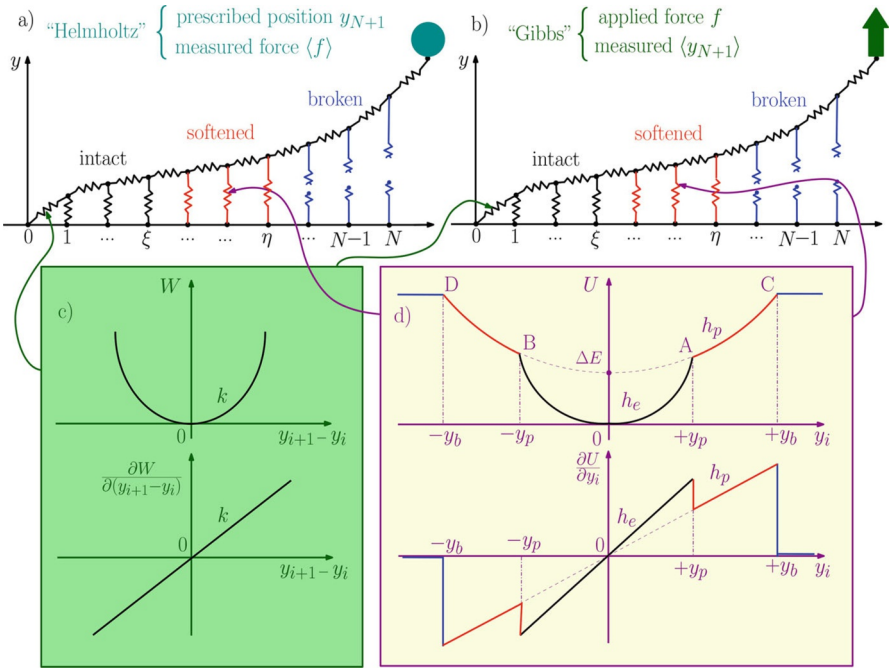

Fig. 3.27 Scheme of the cohesion–decohesion process within both the Helmholtz (**a**) and the Gibbs (**b**) ensembles. While in the first case we prescribe the position y_{N+1} and we measure the average force $\langle f \rangle$, in the second case we apply a force f and we measure the average position $\langle y_{N+1} \rangle$. In both cases, we consider a linear elastic behavior for the horizontal springs (**c**) and a breakable response with softening mechanism (**d**) for the vertical elements. The energy potentials W and U correspond to the horizontal and the vertical springs, respectively

behavior of the strength in sapphire whiskers and some high-entropy and medium-entropy alloys. In the case of the sapphire whiskers (Brenner 1962), the softening transition is represented by the damaging evolution from brittle fracture propagation at low temperature to the nucleation of dislocations before crack propagation at more elevated temperature. On the other hand, for medium-entropy and high-entropy alloys (Miracle et al. 2017; Gali et al. 2013), the softening transition can be identified by a different structure and mobility of dislocations with different strains and temperatures. Of course, in order to model the softening correctly, we would have to consider an arbitrary number of weakened states between the intact and completely broken states, but this would be extremely complicated mathematically.

We consider the cohesion–decohesion process in the system represented in Fig. 3.27 (panels a and b), where we can identify the longitudinal springs, which are linear, with potential energy $W(z) = \frac{1}{2}kz^2$ for any $z \in \mathbb{R}$ (see panel c), and the transverse springs, which can be intact, partially broken, or completely broken (see panel d), depending on their extension. These breakable elements can be described by the potential energy (Cannizzo et al. 2021)

$$U(y) = \begin{cases} \frac{1}{2}h_e y^2 & |y| < y_p, \\ \frac{1}{2}h_p y^2 + \Delta E & y_p < |y| < y_b, \\ \frac{1}{2}h_p y_b^2 + \Delta E & |y| > y_b. \end{cases} \tag{3.89}$$

The behavior of the breakable elements represents a generalization of a simpler case (without the softening mechanism) recently introduced in the literature (Florio et al. 2020). The values $\pm y_p$ of the extension correspond to the softening points A and B of the breakable spring, where the elastic constant switches from h_e to $h_p < h_e$. The force jump at $y = \pm y_p$ is given by $\sqrt{2\Delta E(h_e - h_p)}$ and can be noticed in panel d of Fig. 3.27. We simply calculate that

$$y_p = \sqrt{\frac{2\Delta E}{h_e - h_p}}, \tag{3.90}$$

and we must always impose the inequality $y_b > y_p$, or equivalently, $y_b > \sqrt{\frac{2\Delta E}{h_e - h_p}}$, where $\pm y_b$ are the extensions at the breaking points C and D of the transverse elements. It means that the elements are intact if $|y| < y_p$, partially broken if $y_p < |y| < y_b$, and completely broken when $|y| > y_b$. In the following, we assume that a first group of ξ elements of the chain are intact ($i = 1, \ldots, \xi$), a second group of $\eta - \xi$ elements are partially broken ($i = \xi + 1, \ldots, \eta$), and a third group of $N - \eta$ elements are completely broken ($i = \eta + 1, \ldots, N$). In other terms, it means that we consider two domain walls, the first between intact and partially broken elements and the second between partially broken and completely broken elements (see Fig. 3.27). These walls can move in response to the mechanical action applied to the system and are also influenced by the thermal fluctuations.

We describe the main results we can find within the Helmholtz ensemble. We can introduce the elastic constant ratios $\alpha = h_e/k$, $\beta = h_p/k$. In order to further simplify the analysis of the system, we can now introduce the adimensional applied extension $\mathcal{Y} = y_{N+1}/y_b$, the adimensional average force $\langle \mathcal{F} \rangle = \frac{\langle f \rangle}{k y_b}$, and the energy ratios $\delta = \frac{k y_b^2}{2K_B T} > 0$, $\varphi = \frac{\Delta E}{K_B T} > 0$. The following quantities are useful to show the system behavior:

$$\Delta = \alpha^2 + 4\alpha, \quad \alpha_0 = \frac{2 + \alpha + \sqrt{\Delta}}{2}, \Sigma = \beta^2 + 4\beta, \quad \beta_0 = \frac{2 + \beta + \sqrt{\Sigma}}{2}. \tag{3.91}$$

Also, the temperature

$$T_0 = \frac{2\Delta E}{K_B \log \frac{\alpha_0}{\beta_0}} \tag{3.92}$$

must be considered, since it corresponds to an important transition in the system behavior.

By using these definitions, it is possible to prove that the curve $\langle \mathcal{F} \rangle$ versus $\mathcal{Y}$ is characterized by an asymptotic force $\langle \mathcal{F} \rangle_{as}$ for large values of $\mathcal{Y}$. This asymptotic value represents the strength of the system, and it can be calculated as follows for any temperature $T < T_0$ or $T > T_0$. The asymptotic values follow (Cannizzo et al. 2021)

$$T < T_0 \Rightarrow \langle \mathcal{F} \rangle_{as} = \sqrt{\frac{\beta\delta - \frac{1}{2}\log\alpha_0 + \varphi}{\delta}} = \sqrt{\frac{2\Delta E}{k y_b^2} + \frac{h_p}{k}}\sqrt{1 - \frac{T}{T_b}}, \quad (3.93)$$

where

$$T_b = \frac{2\Delta E + h_p y_b^2}{K_B \log\alpha_0} = \frac{2\Delta E + h_p y_b^2}{K_B \log\frac{2+\alpha+\sqrt{\alpha^2+4\alpha}}{2}}, \quad (3.94)$$

and

$$T > T_0 \Rightarrow \langle \mathcal{F} \rangle_{as} = \sqrt{\frac{\beta\delta - \frac{1}{2}\log\beta_0}{\delta}} = \sqrt{\frac{h_p}{k}}\sqrt{1 - \frac{T}{T_c}}, \quad (3.95)$$

where

$$T_c = \frac{h_p y_b^2}{K_B \log\beta_0} = \frac{h_p y_b^2}{K_B \log\frac{2+\beta+\sqrt{\beta^2+4\beta}}{2}}. \quad (3.96)$$

The temperatures T_b and T_c represent two critical temperatures of the system, as widely discussed below. In a few words, we can say that when we are close to these critical temperatures, the system undergoes a phase transition corresponding to the complete breaking of all the elements.

An important point concerns the emergence of two different cases depending on the parameters of the system. Indeed, it can be easily verified that for small values of the breaking extension y_b, we have $T_c < T_b < T_0$, and for larger value of y_b, we have $T_0 < T_b < T_c$. More precisely, we can state that

$$\frac{\beta}{\alpha - \beta} < \frac{h_p y_b^2}{2\Delta E} < \frac{\log\beta_0}{\log\alpha_0 - \log\beta_0} \Rightarrow T_c < T_b < T_0, \quad (3.97)$$

$$\frac{h_p y_b^2}{2\Delta E} > \frac{\log\beta_0}{\log\alpha_0 - \log\beta_0} \Rightarrow T_0 < T_b < T_c. \quad (3.98)$$

We remark that the first limitation $\frac{\beta}{\alpha-\beta} < \frac{h_p y_b^2}{2\Delta E}$ corresponds to the existence of the softening region, i.e., to $y_b > y_p$. On the other hand, the second ratio $\frac{\log\beta_0}{\log\alpha_0 - \log\beta_0}$ is at the origin of a real transition in the system behavior. It follows that, for small

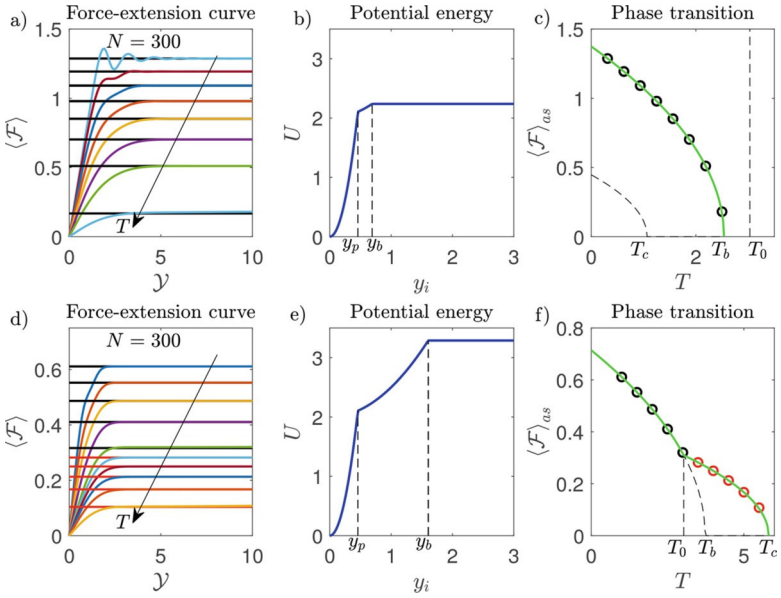

Fig. 3.28 Behavior of the asymptotic force versus the temperature for a small (panels **a**, **b**, and **c**) and a large (panels **d**, **e**, and **f**) value of the breaking extension y_b. Panels a and d: comparison between the solution of the problem with $N = 300$ (colored curves) and Eqs. (3.93) (black straight lines) and (3.95) (red straight lines). In panel a, we used eight values of T between 0 and T_b, and in panel d, we used ten values of T between 0 and T_c. Panels b and e: potential energy of the adopted breakable elements with different y_b ($y_b = 1.5y_p$ in panel **b** and $y_b = 3.5y_p$ in panel **e**). Panels c and f: asymptotic force versus temperature (the green lines corresponds to Eqs. (3.93) and (3.95) and the circles to the colored curves of panels a and d for $\mathcal{Y} = 10$). The adopted parameters follow: $h_e = 20$, $h_p = 1$, $\Delta E = 2$, $k = 5$, and $K_B = 1$ (all in arbitrary units)

values of y_b, only Eq. (3.93) describes the behavior of the asymptotic force versus the temperature of the system. Differently, for larger value of y_b, both Eqs. (3.93) and (3.95) represent the force-temperature curve, with a transition for $T = T_0$. In this case, we have to examine continuity of $\langle \mathcal{F} \rangle_{as}$ for $T = T_0$: It can be easily proved that $\sqrt{\frac{2\Delta E}{k y_b^2} + \frac{h_p}{k}}\sqrt{1 - \frac{T_0}{T_b}} = \sqrt{\frac{h_p}{k}}\sqrt{1 - \frac{T_0}{T_c}}$, where T_0 is defined in Eq. (3.92) and T_b and T_c are defined in Eqs. (3.94) and (3.96), respectively. This demonstrates that the asymptotic force is a continuous function of the temperature (for large value of y_b).

This complex scenario is illustrated in Fig. 3.28, where the solution of the problem with a large value of N is compared with Eqs. (3.93) and (3.95). When $\frac{\beta}{\alpha - \beta} < \frac{h_p y_b^2}{2\Delta E} < \frac{\log \beta_0}{\log \alpha_0 - \log \beta_0}$, the phase transition corresponds to the critical temperature T_b. Conversely, when $\frac{h_p y_b^2}{2\Delta E} > \frac{\log \beta_0}{\log \alpha_0 - \log \beta_0}$, the phase transition occurs at the critical temperature T_c (after a behavioral continuous transition at T_0, as previously explained). From panels c and f of Fig. 3.28, we deduce that the force

needed to obtain the complete detachment of the system monotonically decreases to zero for increasing values of the temperature. This process terminates at $T = T_b$ in panel c and at $T = T_c$ in panel f. It means that the thermal fluctuations are able to promote the fracture of the breakable elements and that the critical temperatures T_b and T_c are sufficient to completely break the system even without an applied mechanical action.

The transition at T_0 in Fig. 3.28, panel f, can be explained by determining the behavior of the average number of partially broken elements $\langle \eta - \xi \rangle$ versus the temperature (Cannizzo et al. 2021). We can obtain that $\langle \eta - \xi \rangle \to \infty$ for $T \to T_0$, proving that all elements are (at least) partially broken for temperatures larger than T_0. Therefore, we have the first transition at T_0 where all the elements are partially broken and a second transition at T_c where all the elements are completely broken. This is coherent with the result stating that $\langle N - \eta \rangle \to \infty$ for $T \to T_c$ for any value of the extension $\mathcal{Y}$.

We do not discuss here the behavior of the system under the Gibbs condition. Anyway, we can affirm that the two ensembles are not equivalent in the thermodynamic limit, but the asymptotic decohesion forces given by Eqs. (3.93) and (3.95) are the same (similarly to what has been observed for the system without the softening mechanism) (Florio et al. 2020; Cannizzo et al. 2021). The curves observed in Fig. 3.28 (panels c and f) are useful to describe the strength of some materials as function of the temperature as discussed in the next section.

6.1 Comparison with Experimental Results

In this section, we use the obtained results to give an interpretation of some experiments conducted to determine the tensile behavior of different materials at elevated temperature, under an applied mechanical load.

The first case concerns filamentary crystals or whiskers of sapphire (Al_2O_3) with a diameter between 8 and 40 μm (Brenner 1962). In these structures, the damage can be generated by the propagation of a fracture that, at the microscopic scale, can be modeled by our dechoesion theory, discussed in the previous section. Indeed, the fracture propagation can be viewed as a sequence of ruptures, representing the breaking of the chemical bonds along a direction of the crystal structure. In particular, our model will be used to analyze the effect of the temperature on this damaging process. The whiskers being essentially free of dislocations, at least without applied stress and for low temperature, the magnitude of their strengths should be an indication of the stresses required for either crack propagation or dislocation nucleation. The temperature dependence of these stresses has been measured by Brenner (1962). The experimental average fracture strength and the experimental maximum fracture stress as a function of temperature are reported in panels (a) and (b) of Fig. 3.29, respectively (Brenner 1962). The transition at around $T = 1550\,^{\circ}\mathrm{C}$ in the stress decrease suggests a change in the mechanism of failure leading to the complete fracture. Brenner (1962) has proposed the following

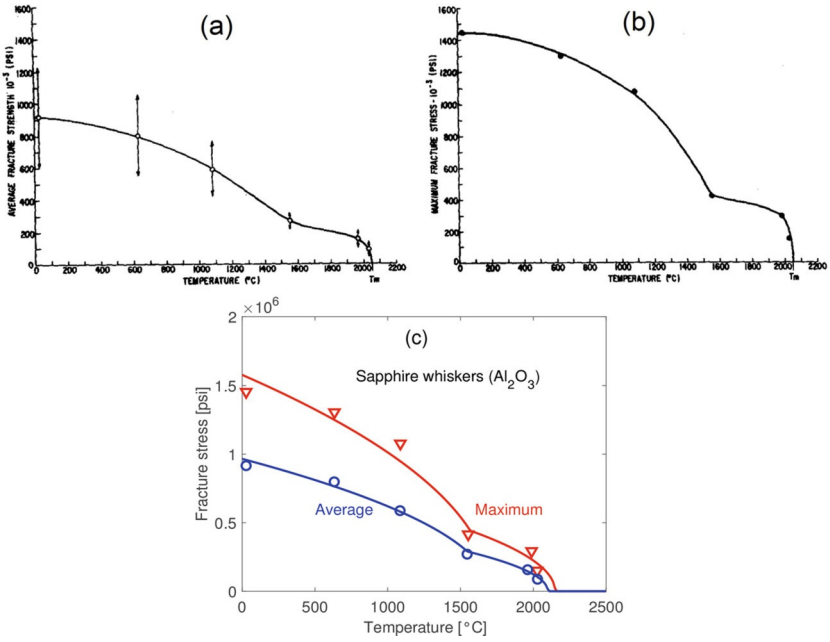

Fig. 3.29 Mechanical behavior of sapphire whiskers at elevated temperatures. The experimental average fracture strength (panel **a**) and the experimental maximum fracture stress (panel **b**), as a function of temperature, are reproduced with permission from Brenner (1962). Panel (**c**): comparison between theoretical and experimental average and maximum strengths based on Eqs. (3.93) and (3.95)

scenario. First of all, it is supposed that some defects are distributed within the whiskers (formed during the crystal growth), and they are able to intensify the applied stress through Griffith- and/or Eshelby-like mechanisms. At a given level of applied stress, the locally intensified stress around the defects can generate propagation of the crack or nucleation of dislocations. Brenner (1962) provides evidence that at the lower temperatures, the enhanced stress causes crack propagation without dislocation nucleation, while at elevated temperatures, dislocations are generated before the fracture propagation. In the latter case, the population of dislocations is able to reduce the elastic stiffness of the material. In our model, the generation of dislocations can be therefore represented by the softening mechanism described by the transition of the stiffness of the vertical springs between h_e and h_p, shown in Fig. 3.27. It is interesting to observe that the theoretical behavior of the strength shows a transitional behavior at T_0, as shown in Fig. 3.28, panel f. The temperature T_0 is therefore around 1550 °C for the sapphire whiskers. The decohesion forces given by Eqs. (3.93) and (3.95) are able to represent the experimental results on the strength of the sapphire whiskers, as shown in panel (c) of Fig. 3.29. The quite good agreement between theory and experiments can be noticed.

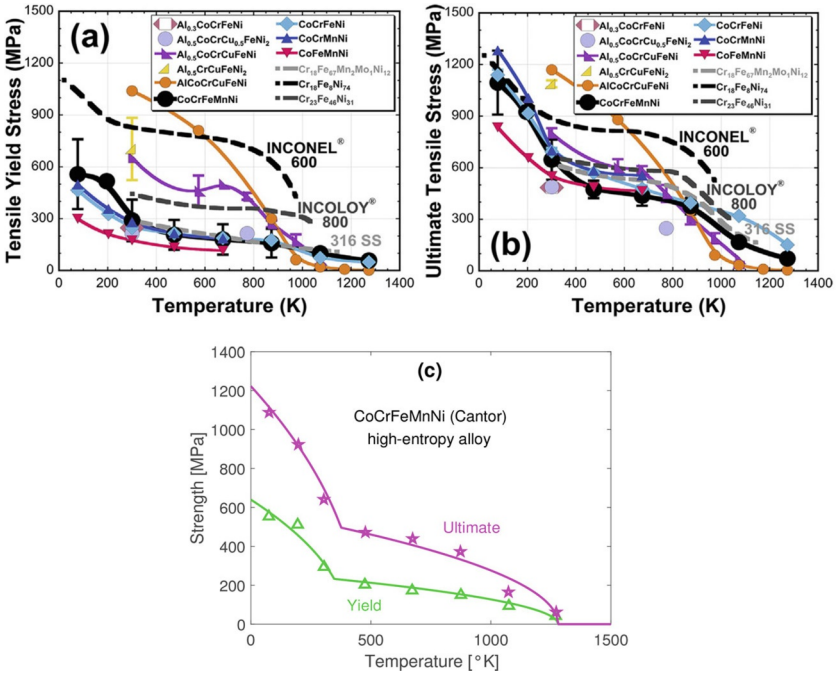

Fig. 3.30 Mechanical behavior of high-entropy and medium-entropy alloys over a large temperature range. The experimental tensile yield stress (panel **a**) and the experimental ultimate tensile stress (panel **b**), as a function of temperature, are reproduced with permission from Miracle et al. (2017). Panel (**c**): comparison between theoretical and experimental results for the quinary CrMnFeCoNi alloy (also named Cantor alloy), based on Eqs. (3.93) and (3.95)

Another class of materials where our theory can be applied is represented by high-entropy alloys. These systems are typically composed of five or more elements with equal (or relatively equal) stoichiometric coefficients. These materials are named high-entropy alloys since the mixing entropy is maximized if the components are present in equal proportions, and it is an increasing function of the number of components. Consequently, when these systems are composed of two to four components, then they are typically named medium-entropy alloys. From a historical point of view, the idea of creating alloys has been used to generate desirable properties in a given artificial material. High-entropy alloys represent a new strategy introduced to exploit a multidimensional compositional space in order to induce exceptional properties to these recent exotic materials. Today, only a small region of this multidimensional space has been explored, and many other alloys can be discovered in the future (George et al. 2019). In Fig. 3.30, one can find the experimental data concerning the tensile yield stress (panel a) and the ultimate tensile stress (panel b) of several high-entropy alloys and medium-entropy alloys (Miracle et al. 2017). The mechanisms at the origin of the mechanical response in these systems are very complex. The distribution of defects plays

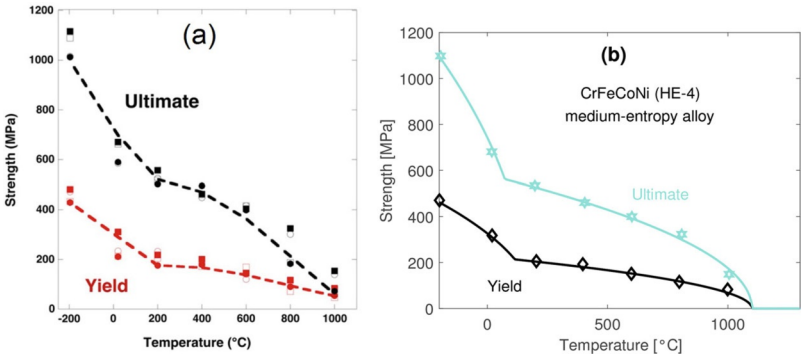

Fig. 3.31 Mechanical behavior of the medium-entropy alloy CrFeCoNi over a large temperature range. The experimental tensile yield stress and ultimate tensile stress (panel **a**), as a function of temperature, are reproduced with permission from Gali et al. (2013). Panel (**b**): comparison between theoretical and experimental results for the CrFeCoNi alloy (also named HE-4), based on Eqs. (3.93) and (3.95)

a crucial role in defining the mechanical properties. At the atomic scale typical defects include vacancies, dislocations, and grain boundaries. At larger scale, other defects are represented by pores, precipitates, cracks, and residual stresses. The static and dynamic interplay of these microstructures is able to determine the overall mechanical response of the whole material. In spite of this complexity, the yield and ultimate strengths, shown in panels (a) and (b) of Fig. 3.30, decrease continuously over the full range of temperatures. More specifically, a first region characterized by a steep drop is followed by a second region where the decrease is slower. As before, the transition between these regions can be interpreted as a change in the underlying damaging physical mechanism.

As a paradigmatic example, we consider the quinary CrMnFeCoNi alloy (also named Cantor alloy), which is one of the first high-entropy alloys investigated (Cantor et al. 2004). This structure crystallizes as a single-phase FCC solid. The strength of this alloy exhibits a strong drop for temperatures below 350 °K and a weaker temperature dependence at elevated temperatures up to around 1270 °K. There is therefore a behavioral transition at the temperature $T_0 = 350\,°\mathrm{K}$. From the microstructural point of view, this can be explained as follows. For small deformation the CoCrFeMnNi alloy exhibits the development of planar dislocation glide, which is typical for FCC metals (Otto et al. 2013). For larger strain, dislocations lose their planar character and organize into cell structures (Otto et al. 2013). This modification induces a larger ductility and a lower stiffness of the overall material. Finally, this process is represented in our model by the softening of the vertical breakable springs, which change their elastic coefficients from h_e to h_p, as shown in Fig. 3.27. In panel (c) of Fig. 3.30, we draw a comparison between the experimental and theoretical results for both the yield and ultimate stress of the quinary CrMnFeCoNi alloy. As before, we remark that the model is able to capture the transition in the behavior of the strength as function of the temperature. Another

example is given in Fig. 3.31, where we take into consideration the mechanical properties of the medium-entropy alloy CrFeCoNi (also named HE-4). In panel (a) of Fig. 3.31 experimental ultimate and yield stresses are reported (Gali et al. 2013). As before, a transition can be observed for a temperature around 200 °C. Also in this case, this transition can be interpreted by a different structure and mobility of the dislocations with different strains and temperatures (Gali et al. 2013). The comparison with the theoretical results is drawn in panel (b) of Fig. 3.31, where a good agreement can be underlined.

We described the application of the softening mechanism to the strength behavior of sapphire whiskers and of high-entropy and medium-entropy alloys. For these material systems, we provided evidence that the theory is able to describe the behavior of both yield and ultimate stress as function of the temperature.

7 Conclusion

We described some biophysical and materials science phenomena governed by internal micro-instabilities, and we introduced some related models based on the combination of micromechanics and statistical mechanics. This combination generates models able to take into consideration both the effect of the thermal fluctuations and the externally applied mechanical actions. These approaches are useful for both systems exhibiting bistability or multistability and for systems characterized by breaking or fracture phenomena including deadhesion and decohesion. The main idea is that of reducing the complexity of the models in order to emphasize common essential features of most real systems and phenomena characterized by micro-instabilities. This approach allows us to develop models of wide applicability, ranging from biophysics to material science, which are independent of the actual molecular architecture of the investigated system. Moreover, the proposed modeling activity is useful for interpreting experimental results by original mathematical approaches that can inspire further generalizations of continuum mechanics with a more comprehensive understanding of thermal phenomena. One of the most promising devices of our approach is the spin variable method, which permits to consider the different states allowed to the units or elements of the system. For example, for a bistable unit the spin variable corresponds to a bit identifying the two possible states of the unit itself. Similarly, in breakable systems, a unit can be in the broken or unbroken state that can be described by a discrete variable with two possible values. More in general, a vector of spin variables can completely represent the state of a system composed of an arbitrary number of bistable or breakable units. These discrete variables belong to the phase space of the system described by the classical statistical mechanics. Hence, when we determine the partition function of the system, we have to integrate the classical continuous Hamiltonian variables and to sum over the discrete values of the spin variables. The knowledge of the partition function enables us to evaluate all the macroscopic thermodynamic quantities of interest to better understand the system behavior. This procedure can

be applied to different statistical ensembles, namely corresponding to the Helmholtz (isometric) or Gibbs (isotensional) conditions. We can therefore analyze the problem of the equivalence of the ensembles in the thermodynamic limit (for very large systems). We discussed in this review four specific problems: The first concerns the force-extension response of macromolecules observed through the force spectroscopy methodology, the second the phase transformations in solid materials with application to whiskers or nanowires, the third the adhesion or deadhesion process of chain or films with the application to the hairpins unzipping, and finally, the fourth the softening mechanism in the cohesion/decohesion process useful to better understand the temperature dependence of strength for some materials. In the first problem investigated, we proposed an interpretation of the two classes of experimental responses observed through single molecule force spectroscopy methods. Indeed, one can observe force-extension curves with a force plateau (synchronized response) or sawtooth curves with a series of force peaks (sequential response). The method of spin variables allowed to give an interpretation of the two responses based on a unified model, simply used with traction devices having different intrinsic elasticity: soft devices for the plateau-like response (isotensional or Gibbs ensemble) and hard device for the sawtooth-like response (isometric or Helmholtz ensemble). In the second problem, we generalized the bistable models in order to consider the interaction between the units by means of an Ising scheme based on the spin variables. This is particularly important to model the behavior of phase transformations in solid materials where the creation of an interface between different phases is costly from the energetic point of view. The interaction coefficient of the Ising scheme exactly describes the energy associated with the domain walls or grain boundaries separating internal phases. The model solution allows us to perfectly understand the nucleation stress and the temperature dependent plateau observed in the experimental stress–strain response. The third problem concerns the adhesion or deadhesion processes of chains or films, and the proposed solution is able to reveal a critical behavior of the system characterized by a critical temperature corresponding to a phase transition. It means that there exists a temperature able to completely detach the system without mechanical actions. This behavior fully corresponds to the observed temperature dependent hairpin unzipping for both DNA and RNA. The agreement between theory and experiments has been evidenced and discussed. Finally the fourth problem concerns the softening mechanism in the cohesion/decohesion processes. It means that the intact elements of the system may be softened before the full rupture. The introduction of this new feature allows us to describe the plastic phenomena associated with the rupture processes and to give an interpretation to the experimentally observed temperature dependent strength of materials. This point has been explicitly discussed for sapphire whiskers, high-entropy, and medium-entropy alloys.

A rather important feature of systems with rupture phenomena is the presence of a phase transition at a well-defined critical temperature. This means that thermal fluctuations have the ability to promote ruptures in the system, favoring the exploration of the phase space corresponding to the broken state (horizontal part of the potential energy). When the temperature reaches its critical value, all bonds

break regardless of the mechanical forces applied to the system (phase transition). This corresponds well with experimental observations obtained with DNA, RNA, and a variety of ceramic and semiconductor nanowires. What is interesting is that our spin variable-based method is able to provide exact mathematical solutions that completely describe these phase transitions and corresponding critical temperatures.

To conclude, we want to underline the fact that the combination of micromechanics with statistical mechanics is able to give further insights about the behavior and the internal mechanisms of complex phenomena in real materials. Of course, the models presented can be improved from several points of view in order to better represent further features of real structures. For example, we have not discussed the time-behavior of these processes (which must be described by the out-of-equilibrium statistical mechanics), the possible heterogeneity of these systems, we always studied one-dimensional structures when more realistic systems are two- or three-dimensional, we have not implemented the real molecular architecture of the investigated materials, and we often adopted a coarse-grained vision in order to simplify the model development. In any case, the interesting results obtained with the preliminary simple models motivate further research in order to implement all these improvements and extensions.

Acknowledgments Stefano Giordano has been supported by “Central Lille” and “Région Hauts-de-France" under projects MePoFib (multiscale approaches for the mechanics of DNA, polymers, and fibers), MiBaMs (modeling micro-instabilities in biophysics and materials science), and StaMeNa (statistical mechanics for macromolecular structures of nanotechnology). He would also like to thank Giuseppe Puglisi and Giuseppe Florio for stimulating discussions on these topics and scientific collaborations.

References

Abeyaratne R, Chu C, James RD (1996) Kinetics of materials with wiggly energies: theory and application to the evolution of twinning microstructures in a Cu-Al-Ni shape memory alloy. Philosophical Magazine A 73(2):457–497. https://doi.org/10.1080/01418619608244394

Alessi R, Bernardini D (2015) Analysis of localization phenomena in Shape Memory Alloys bars by a variational approach. International Journal of Solids and Structures 73–74:113–133. https://doi.org/10.1016/j.ijsolstr.2015.06.021

Amitrano D, Grasso J-R, Hantz D (1999) From diffuse to localised damage through elastic interaction. Geophysical Research Letters 26(14):2109–2112. https://doi.org/10.1029/1999GL900388

Ashkin A (1970a) Atomic-beam deflection by resonance-radiation pressure. Physical Review Letters 25(19):1321–1324. https://doi.org/10.1103/PhysRevLett.25.1321

Ashkin A (1970b) Acceleration and trapping of particles by radiation pressure. Physical Review Letters 24(4):156–159. https://doi.org/10.1103/PhysRevLett.24.156

Ashkin A, Dziedzic JM, Bjorkholm JE, Chu S (1986) Observation of a single-beam gradient force optical trap for dielectric particles. Optics Letters 11(5):288–290. https://doi.org/10.1364/OL.11.000288

Balabaev NK, Khazanovich TN (2009) Extension of chains composed of freely joined elastic segments. Russian Journal of Physical Chemistry B 3(2):242–246. https://doi.org/10.1134/S1990793109020109

Bao L, Zhang X, Shi Y-Z, Wu Y-Y, Tan Z-J (2017) Understanding the relative flexibility of RNA and DNA duplexes: stretching and twist-stretch coupling. Biophysical Journal 112(6):1094–1104. https://doi.org/10.1016/j.bpj.2017.02.022

Bell GI (1978) Models for the specific adhesion of cells to cells. Science 200(4342):618–627. https://doi.org/10.1126/science.347575

Bell GI, Dembo M, Bongrand P (1984) Cell adhesion. Competition between nonspecific repulsion and specific bonding. Biophysical Journal 45(6):1051–1064. https://doi.org/10.1016/S0006-3495(84)84252-6

Bellino L, Florio G, Puglisi G (2019) The influence of device handles in single-molecule experiments. Soft Matter 15(43):8680–8690. https://doi.org/10.1039/C9SM01376H

Bellino L, Florio G, Giordano S, Puglisi G (2020) On the competition between interface energy and temperature in phase transition phenomena. Applications in Engineering Science 2:100009. https://doi.org/10.1016/j.apples.2020.100009

Benedito M, Giordano S (2018a) Thermodynamics of small systems with conformational transitions: the case of two-state freely jointed chains with extensible units. The Journal of Chemical Physics 149(5):054901. https://doi.org/10.1063/1.5026386

Benedito M, Giordano S (2018b) Isotensional and isometric force-extension response of chains with bistable units and Ising interactions. Physical Review E 98(5):052146. https://doi.org/10.1103/PhysRevE.98.052146

Benedito M, Manca F, Giordano S (2019) Full statistics of conjugated thermodynamic ensembles in chains of bistable units. Inventions 4(1):19. https://doi.org/10.3390/inventions4010019

Benedito M, Giordano S (2020a) Unfolding pathway and its identifiability in heterogeneous chains of bistable units. Physics Letters A 384(5):126124. https://doi.org/10.1016/j.physleta.2019.126124

Benedito M, Manca F, Palla PL, Giordano S (2020b) Rate-dependent force–extension models for single-molecule force spectroscopy experiments. Physical Biology 17(5):056002. https://doi.org/10.1088/1478-3975/ab97a8

Benichou I, Givli S (2013) Structures undergoing discrete phase transformation. Journal of the Mechanics and Physics of Solids 61(1):94–113. https://doi.org/10.1016/j.jmps.2012.08.009

Benichou I, Givli S (2015) Rate dependent response of nanoscale structures having a multiwell energy landscape. Physical Review Letters 114(9):095504. https://doi.org/10.1103/PhysRevLett.114.095504

Benichou I, Zhang Y, Dudko OK, Givli S (2016) The rate dependent response of a bistable chain at finite temperature. Journal of the Mechanics and Physics of Solids 95:44–63. https://doi.org/10.1016/j.jmps.2016.05.001

Binnig G, Quate CF, Gerber Ch (1986) Atomic force microscope. Physical Review Letters 56(9):930–933. https://doi.org/10.1103/PhysRevLett.56.930

Biscari P, Urbano MF, Zanzottera A, Zanzotto G (2016) Intermittency in crystal plasticity informed by lattice symmetry. Journal of Elasticity 123(1):85–96. https://doi.org/10.1007/s10659-015-9548-z

Bleha T, Cifra P (2018) Stretching and compression of DNA by external forces under nanochannel confinement. Soft Matter 14(7):1247–1259. https://doi.org/10.1039/C7SM02413D

Bleha T, Cifra P (2022) Energy/entropy partition of force at DNA stretching. Biopolymers 113(5):e23487. https://doi.org/10.1002/bip.23487

Blumberg Selinger RL, Wang Z-G, Gelbart WM, Ben-Shaul A (1991) Statistical-thermodynamic approach to fracture. Physical Review A 43(8):4396–4400. https://doi.org/10.1103/PhysRevA.43.4396

Bonilla LL, Carpio A, Prados A (2015) Theory of force-extension curves for modular proteins and DNA hairpins. Physical Review E 91(5):052712. https://doi.org/10.1103/PhysRevE.91.052712

Borja da Rocha H, Truskinovsky L (2019) Equilibrium unzipping at finite temperature. Archive of Applied Mechanics 89(3):535–544. https://doi.org/10.1007/s00419-018-1485-4

Borja da Rocha H, Truskinovsky L (2020) Rigidity-controlled crossover: from spinodal to critical failure. Physical Review Letters 124(1):015501. https://doi.org/10.1103/PhysRevLett.124.015501

Bormuth V, Varga V, Howard J, Schäffer E (2009) Protein friction limits diffusive and directed movements of Kinesin Motors on microtubules. Science 325(5942):870–873. https://doi.org/10.1126/science.1174923

Bosaeus N, El-Sagheer AH, Brown T, Smith SB, Åkerman B, Bustamante C, Nordén B (2012) Tension induces a base-paired overstretched DNA conformation. Proceedings of the National Academy of Sciences 109(38):15179–15184. https://doi.org/10.1073/pnas.1213172109

Brenner SS (1962) Mechanical behavior of sapphire whiskers at elevated temperatures. Journal of Applied Physics 33(1):33–39. https://doi.org/10.1063/1.1728523

Buche MR, Silberstein MN (2020) Statistical mechanical constitutive theory of polymer networks: the inextricable links between distribution, behavior, and ensemble. Physical Review E 102(1):012501. https://doi.org/10.1103/PhysRevE.102.012501

Buche MR, Silberstein MN (2021) Chain breaking in the statistical mechanical constitutive theory of polymer networks. Journal of the Mechanics and Physics of Solids 156:104593. https://doi.org/10.1016/j.jmps.2021.104593

Buche MR, Silberstein MN, Grutzik SJ (2022) Freely jointed chain models with extensible links. Physical Review E 106(2):024502. https://doi.org/10.1103/PhysRevE.106.024502

Bustamante C, Marko JF, Siggia ED, Smith S (1994) Entropic elasticity of λ-phage DNA. Science 265(5178):1599–1600. https://doi.org/10.1126/science.8079175

Cannizzo A, Florio G, Puglisi G, Giordano S (2021) Temperature controlled decohesion regimes of an elastic chain adhering to a fixed substrate by softening and breakable bonds. Journal of Physics A: Mathematical and Theoretical 54(44):445001. https://doi.org/10.1088/1751-8121/ac2a07

Cannizzo A, Bellino L, Florio G, Puglisi G, Giordano S (2022) Thermal control of nucleation and propagation transition stresses in discrete lattices with non-local interactions and non-convex energy. The European Physical Journal Plus 137(5):569. https://doi.org/10.1140/epjp/s13360-022-02790-9

Cannizzo A, Giordano S (2023) Thermal effects on fracture and the brittle-to-ductile transition. Physical Review E 107(3):035001. https://doi.org/10.1103/PhysRevE.107.035001

Cantor B, Chang ITH, Knight P, Vincent AJB (2004) Microstructural development in equiatomic multicomponent alloys. Materials Science and Engineering A 375–377:213–218. https://doi.org/10.1016/j.msea.2003.10.257

Caruel M, Allain J-M, Truskinovsky L (2013) Muscle as a metamaterial operating near a critical point. Physical Review Letters 110(24):248103. https://doi.org/10.1103/PhysRevLett.110.248103

Caruel M, Allain J-M, Truskinovsky L (2015) Mechanics of collective unfolding. Journal of the Mechanics and Physics of Solids 76:237–259. https://doi.org/10.1016/j.jmps.2014.11.010

Caruel M, Moireau P, Chapelle D (2019) Stochastic modeling of chemical–mechanical coupling in striated muscles. Biomechanics and Modeling in Mechanobiology 18(3):563–587. https://doi.org/10.1007/s10237-018-1102-z

Caruel M, Truskinovsky L (2016) Statistical mechanics of the Huxley-Simmons model. Physical Review E 93(6):062407. https://doi.org/10.1103/PhysRevE.93.062407

Caruel M, Truskinovsky L (2017) Bi-stability resistant to fluctuations. Journal of the Mechanics and Physics of Solids 109:117–141. https://doi.org/10.1016/j.jmps.2017.08.007

Caruel M, Truskinovsky L (2018) Physics of muscle contraction. Reports on Progress in Physics 81(3):036602. https://doi.org/10.1088/1361-6633/aa7b9e

Cheng T, Qu Z, Li W, Fang D (2020) Fracture strength behaviors of ultra-high-temperature materials. Journal of Applied Mechanics 87(3). https://doi.org/10.1115/1.4045046

Chiou C-H, Lee G-B (2005) A micromachined DNA manipulation platform for the stretching and rotation of a single DNA molecule. Journal of Micromechanics and Microengineering 15(1):109. https://doi.org/10.1088/0960-1317/15/1/017

Cleri F (2008) Microscopic mechanics of biomolecules in living cells. Scientific Modeling and Simulation 15(1):339–362. https://doi.org/10.1007/s10820-008-9104-2

Cocco S, Yan J, Léger J-F, Chatenay D, Marko JF (2004) Overstretching and force-driven strand separation of double-helix DNA. Physical Review E 70(1):011910. https://doi.org/10.1103/PhysRevE.70.011910

Cortet P-P, Ciccotti M, Vanel L (2007) Imaging the stick–slip peeling of an adhesive tape under a constant load. Journal of Statistical Mechanics 2007(03):P03005. https://doi.org/10.1088/1742-5468/2007/03/P03005

Crick FHC, Hughes AFW (1950) The physical properties of cytoplasm: a study by means of the magnetic particle method Part I. Experimental. Experimental Cell Research 1(1):37–80. https://doi.org/10.1016/0014-4827(50)90048-6

Crothers DM, Kallenbach NR, Zimm BH (1965) The melting transition of low-molecular-weight DNA: theory and experiment. Journal of Molecular Biology 11(4):802–820. https://doi.org/10.1016/S0022-2836(65)80037-7

Dalbe M-J, Cortet P-P, Ciccotti M, Vanel L, Santucci S (2015) Multiscale stick-slip dynamics of adhesive tape peeling. Physical Review Letters 115(12):128301. https://doi.org/10.1103/PhysRevLett.115.128301

Das S, Chary S, Yu J, Tamelier J, Turner KL, Israelachvili JN (2013) JKR theory for the stick–slip peeling and adhesion hysteresis of gecko mimetic patterned surfaces with a smooth glass surface. Langmuir 29(48):15006–15012. https://doi.org/10.1021/la403420f

Daub EG, Carlson JM (2010) Friction, fracture, and earthquakes. Annual Review of Condensed Matter Physics 1(1):397–418. https://doi.org/10.1146/annurev-conmatphys-070909-104025

De Lorenzo S, Ribezzi-Crivellari M, Arias-Gonzalez JR, Smith SB, Ritort F (2015) A temperature-jump optical trap for single-molecule manipulation. Biophysical Journal 108(12):2854–2864. https://doi.org/10.1016/j.bpj.2015.05.017

De Tommasi D, Millardi N, Puglisi G, Saccomandi G (2013) An energetic model for macromolecules unfolding in stretching experiments. Journal of the Royal Society Interface 10(88):20130651. https://doi.org/10.1098/rsif.2013.0651

Dimitrov DI, Klushin LI, Skvortsov A, Milchev A, Binder K (2009) The escape transition of a polymer: a unique case of non-equivalence between statistical ensembles. The European Physical Journal E 29(1):9–25. https://doi.org/10.1140/epje/i2008-10442-0

Doi M (1996) Introduction to polymer physics. Oxford University Press, Oxford, New York

Dudko OK (2016) Decoding the mechanical fingerprints of biomolecules. Quarterly Reviews of Biophysics 49:e3. https://doi.org/10.1017/S0033583515000220

Dudko OK, Mathé J, Szabo A, Meller A, Hummer G (2007) Extracting kinetics from single-molecule force spectroscopy: nanopore unzipping of DNA hairpins. Biophysical Journal 92(12):4188–4195. https://doi.org/10.1529/biophysj.106.102855

Dutta S, Benetatos P (2018) Inequivalence of fixed-force and fixed-extension statistical ensembles for a flexible polymer tethered to a planar substrate. Soft Matter 14(33):6857–6866. https://doi.org/10.1039/C8SM01321G

Dutta S, Benetatos P (2019) Statistical ensemble inequivalence for flexible polymers under confinement in various geometries. Soft Matter 16(8):2114–2127. https://doi.org/10.1039/C9SM02246E

Duval A, Haboussi M, Ben Zineb T (2011) Modelling of localization and propagation of phase transformation in superelastic SMA by a gradient nonlocal approach. International Journal of Solids and Structures 48(13):1879–1893. https://doi.org/10.1016/j.ijsolstr.2011.02.019

Efendiev YR, Truskinovsky L (2010) Thermalization of a driven bi-stable FPU chain. Continuum Mechanics and Thermodynamics 22(6):679–698. https://doi.org/10.1007/s00161-010-0166-5

Eghiaian F, Rico F, Colom A, Casuso I, Scheuring S (2014) High-speed atomic force microscopy: imaging and force spectroscopy. FEBS Letters 588(19):3631–3638. https://doi.org/10.1016/j.febslet.2014.06.028

Epstein M, Herzog W (1998) Theoretical models of skeletal muscle: biological and mathematical considerations. Wiley, Chichester, New York

Erdmann T, Schwarz US (2007) Impact of receptor-ligand distance on adhesion cluster stability. The European Physical Journal E 22(2):123–137. https://doi.org/10.1140/epje/e2007-00019-8

Ericksen JL (1975) Equilibrium of bars. Journal of Elasticity 5(3):191–201. https://doi.org/10.1007/BF00126984

Fedelich B, Zanzotto G (1992) Hysteresis in discrete systems of possibly interacting elements with a double-well energy. Journal of Nonlinear Science 2(3):319–342. https://doi.org/10.1007/BF01208928

Fisher TE, Oberhauser AF, Carrion-Vazquez M, Marszalek PE, Fernandez JM (1999) The study of protein mechanics with the atomic force microscope. Trends in Biochemical Sciences 24(10):379–384. https://doi.org/10.1016/S0968-0004(99)01453-X

Florio G, Puglisi G (2019) Unveiling the influence of device stiffness in single macromolecule unfolding. Scientific Reports 9(1):4997. https://doi.org/10.1038/s41598-019-41330-x

Florio G, Puglisi G, Giordano S (2020) Role of temperature in the decohesion of an elastic chain tethered to a substrate by onsite breakable links. Physical Review Research 2(3):033227. https://doi.org/10.1103/PhysRevResearch.2.033227

Folch A (2013) Introduction to BioMEMS. CRC Press, Boca Raton

Frazier MJ, Kochmann DM (2017) Band gap transmission in periodic bistable mechanical systems. Journal of Sound and Vibration 388:315–326. https://doi.org/10.1016/j.jsv.2016.10.041

Gali A, George EP (2013) Tensile properties of high- and medium-entropy alloys. Intermetallics 39:74–78. https://doi.org/10.1016/j.intermet.2013.03.018

Gao J, Luedtke WD, Gourdon D, Ruths M, Israelachvili JN, Landman U (2004) Frictional forces and Amontons' law: from the molecular to the macroscopic scale. The Journal of Physical Chemistry B 108(11):3410–3425. https://doi.org/10.1021/jp0363621

Gao H, Qian J, Chen B (2011) Probing mechanical principles of focal contacts in cell–matrix adhesion with a coupled stochastic–elastic modelling framework. Journal of the Royal Society Interface 8(62):1217–1232. https://doi.org/10.1098/rsif.2011.0157

George EP, Raabe D, Ritchie RO (2019) High-entropy alloys. Nature Reviews Materials 4(8):515–534. https://doi.org/10.1038/s41578-019-0121-4

Gerde E, Marder M (2001) Friction and fracture. Nature 413(6853):285–288. https://doi.org/10.1038/35095018

Gibbs JW (1902) Elementary principles in statistical mechanics. Charles Scribner's Sons, New York

Gibbs JH, DiMarzio EA (1959) Statistical mechanics of helix-coil transitions in biological macromolecules. The Journal of Chemical Physics 30(1):271–282. https://doi.org/10.1063/1.1729886

Gieseler J, Gomez-Solano JR, Magazzù A, Castillo IP, García LP, Gironella-Torrent M, Viader-Godoy X, Ritort F, Pesce G, Arzola AV, Volke-Sepúlveda K, Volpe G (2021) Optical tweezers—from calibration to applications: a tutorial. Advances in Optics and Photonics 13(1):74–241. https://doi.org/10.1364/AOP.394888

Gimbert F, Amitrano D, Weiss J (2013) Crossover from quasi-static to dense flow regime in compressed frictional granular media. EPL 104(4):46001. https://doi.org/10.1209/0295-5075/104/46001

Giordano S (2017) Spin variable approach for the statistical mechanics of folding and unfolding chains. Soft Matter 13(38):6877–6893. https://doi.org/10.1039/C7SM00882A

Giordano S (2018) Helmholtz and Gibbs ensembles, thermodynamic limit and bistability in polymer lattice models. Continuum Mechanics and Thermodynamics 30(3):459–483. https://doi.org/10.1007/s00161-017-0615-5

Giordano S (2022) Statistical mechanics of rate-independent stick-slip on a corrugated surface composed of parabolic wells. Continuum Mechanics and Thermodynamics 34(5):1343–1372. https://doi.org/10.1007/s00161-022-01129-0

Giordano S (2023) Temperature dependent model for the quasistatic stick–slip process on a soft substrate. Soft Matter 19(9):1813. https://doi.org/10.1039/d2sm01262f

Glatting G, Winkler RG, Reineker P (1993) Partition function and force extension relation for a generalized freely jointed chain. Macromolecules 26(22):6085–6091. https://doi.org/10.1021/ma00074a033

Gorbushin N, Mishuris G, Truskinovsky L (2020) Frictionless motion of lattice defects. Physical Review Letters 125(19):195502. https://doi.org/10.1103/PhysRevLett.125.195502

Gräter F, Shen J, Jiang H, Gautel M, Grubmüller H (2005) Mechanically induced Titin kinase activation studied by force-probe molecular dynamics simulations. Biophysical Journal 88(2):790–804. https://doi.org/10.1529/biophysj.104.052423

Grinza P, Mossa A (2004) Topological origin of the phase transition in a model of DNA denaturation. Physical Review Letters 92(15):158102. https://doi.org/10.1103/PhysRevLett.92.158102

Gumbiner BM (1996) Cell adhesion: the molecular basis of tissue architecture and morphogenesis. Cell 84(3):345–357. https://doi.org/10.1016/S0092-8674(00)81279-9

Guo X, Liang W, Zhou M (2009) Mechanism for the pseudoelastic behavior of FCC shape memory nanowires. Experimental Mechanics 49(2):183–190. https://doi.org/10.1007/s11340-008-9173-x

Harne RL, Schoemaker ME, Dussault BE, Wang KW (2014a) Wave heave energy conversion using modular multistability. Applied Energy 130:148–156. https://doi.org/10.1016/j.apenergy.2014.05.038

Harne RL, Schoemaker ME, Wang KW (2014b) Multistable chain for ocean wave vibration energy harvesting: active and passive smart structures and integrated systems 2014. In: Active and passive smart structures and integrated systems. https://doi.org/10.1117/12.2044267

Hill TL (1973) Theory of muscular contraction extended to groups of actin sites. Proceedings of the National Academy of Sciences 70(10):2732–2736. https://doi.org/10.1073/pnas.70.10.2732

Hoffmann T, Dougan L (2012) Single molecule force spectroscopy using polyproteins. Chemical Society Reviews 41(14):4781–4796. https://doi.org/10.1039/C2CS35033E

Hu YZ, Lindstrøm T, Øksendal B, Ubøe J, Zhang TS (1995) Inverse powers of white noise. In: Stochastic analysis, vol 57, pp. 439–456. American Mathematical Society. https://doi.org/10.1090/pspum/057/1335488

Huang P-Y, Guo Z-S, Feng J-M (2020) General model of temperature-dependent modulus and yield strength of thermoplastic polymers. Chinese Journal of Polymer Science 38(4):382–393. https://doi.org/10.1007/s10118-020-2360-7

Hughes ML, Dougan L (2016) The physics of pulling polyproteins: a review of single molecule force spectroscopy using the AFM to study protein unfolding. Reports on Progress in Physics 79(7):076601. https://doi.org/10.1088/0034-4885/79/7/076601

Huxley AF, Simmons RM (1971) Proposed mechanism of force generation in striated muscle. Nature 233(5321):533–538. https://doi.org/10.1038/233533a0

Hwang M, Arrieta AF (2018) Input-independent energy harvesting in bistable lattices from transition waves. Scientific Reports 8(1):3630. https://doi.org/10.1038/s41598-018-22003-7

Hyeon C, Thirumalai D (2005) Mechanical unfolding of RNA hairpins. Proceedings of the National Academy of Sciences 102(19):6789–6794. https://doi.org/10.1073/pnas.0408314102

Ivanov V, Zeng Y, Zocchi G (2004) Statistical mechanics of base stacking and pairing in DNA melting. Physical Review E 70(5):051907. https://doi.org/10.1103/PhysRevE.70.051907

Jorge Do Marco R, Giordano S (2022) Thermodynamics of extra-toughness and hidden-length in polymeric materials with sacrificial bonds. Journal of Applied Mechanics 3(3):935–955. https://doi.org/10.3390/applmech3030053

Karimi K, Amitrano D, Weiss J (2019) From plastic flow to brittle fracture: role of microscopic friction in amorphous solids. Physical Review E 100(1):012908. https://doi.org/10.1103/PhysRevE.100.012908

Katz S, Givli S (2018) Solitary waves in a bistable lattice. Extreme Mechanics Letters 22:106–111. https://doi.org/10.1016/j.eml.2018.06.003

Katz S, Givli S (2019) Solitary waves in a nonintegrable chain with double-well potentials. Physical Review E 100(3):032209. https://doi.org/10.1103/PhysRevE.100.032209

Kittel C (1969) Phase transition of a molecular zipper. American Journal of Physics 37(9):917–920. https://doi.org/10.1119/1.1975930

Kramers HA (1940) Brownian motion in a field of force and the diffusion model of chemical reactions. Physica 7(4):284–304. https://doi.org/10.1016/S0031-8914(40)90098-2

Kresse O, Truskinovsky L (2004) Lattice friction for crystalline defects: from dislocations to cracks. Journal of the Mechanics and Physics of Solids 52(11):2521–2543. https://doi.org/10.1016/j.jmps.2004.04.011

Krylov SYu, Frenken JWM (2014) The physics of atomic-scale friction: basic considerations and open questions. Physica Status Solidi (b) 251(4):711–736. https://doi.org/10.1002/pssb.201350154

Kumar S, Li MS (2010) Biomolecules under mechanical force. Physics Reports 486(1):1–74. https://doi.org/10.1016/j.physrep.2009.11.001

Lee EH, Hsin J, Sotomayor M, Comellas G, Schulten K (2009) Discovery through the computational microscope. Structure 17(10):1295–1306. https://doi.org/10.1016/j.str.2009.09.001

Li W, Zhang X, Kou H, Wang R, Fang D (2016) Theoretical prediction of temperature dependent yield strength for metallic materials. International Journal of Mechanical Sciences 105:273–278. https://doi.org/10.1016/j.ijmecsci.2015.11.017

Liamas E, Connell SD, Ramakrishna SN, Sarkar A (2020) Probing the frictional properties of soft materials at the nanoscale. Nanoscale 12(4):2292–2308. https://doi.org/10.1039/C9NR07084B

Liang W, Srolovitz DJ, Zhou M (2007) A micromechanical continuum model for the tensile behavior of shape memory metal nanowires. Journal of the Mechanics and Physics of Solids 55(8):1729–1761. https://doi.org/10.1016/j.jmps.2007.01.001

Liang W, Zhou M (2006) Atomistic simulations reveal shape memory of FCC metal nanowires. Physical Review B 73(11):115409. https://doi.org/10.1103/PhysRevB.73.115409

Lipfert J, Kerssemakers JWJ, Jager T, Dekker NH (2010) Magnetic torque tweezers: measuring torsional stiffness in DNA and RecA-DNA filaments. Nature Methods 7(12):977–980. https://doi.org/10.1038/nmeth.1520

Lipfert J, Wiggin M, Kerssemakers JWJ, Pedaci F, Dekker NH (2011) Freely orbiting magnetic tweezers to directly monitor changes in the twist of nucleic acids. Nature Communications 2(1):439. https://doi.org/10.1038/ncomms1450

Liphardt J, Onoa B, Smith SB, Tinoco I, Bustamante C (2001) Reversible unfolding of single RNA molecules by mechanical force. Science 292(5517):733–737. https://doi.org/10.1126/science.1058498

Ma F, Xu K-W, Chu PK (2013) Surface-induced structural transformation in nanowires. Materials Science and Engineering R 74(6):173–209. https://doi.org/10.1016/j.mser.2013.05.001

Maddalena F, Percivale D, Puglisi G, Truskinovsky L (2009) Mechanics of reversible unzipping. Continuum Mechanics and Thermodynamics 21(4):251. https://doi.org/10.1007/s00161-009-0108-2

Manca F, Giordano S, Palla PL, Zucca R, Cleri F, Colombo L (2012) Elasticity of flexible and semiflexible polymers with extensible bonds in the Gibbs and Helmholtz ensembles. The Journal of Chemical Physics 136(15):154906. https://doi.org/10.1063/1.4704607

Manca F, Giordano S, Palla PL, Cleri F, Colombo L (2013a) Response to "Comment on 'Elasticity of flexible and semiflexible polymers with extensible bonds in the Gibbs and Helmholtz ensembles"' [J. Chem. Phys. 138, 157101 (2013)]. The Journal of Chemical Physics 138(15):157102. https://doi.org/10.1063/1.4801656

Manca F, Giordano S, Palla PL, Cleri F, Colombo L (2013b) Two-state theory of single-molecule stretching experiments. Physical Review E 87(3):032705. https://doi.org/10.1103/PhysRevE.87.032705

Manca F, Giordano S, Palla PL, Cleri F (2014a) On the equivalence of thermodynamics ensembles for flexible polymer chains. Physica A: Statistical Mechanics and Its Applications 395:154–170. https://doi.org/10.1016/j.physa.2013.10.042

Manca F, Giordano S, Palla PL, Cleri F (2014b) Scaling shift in multicracked fiber bundles. Physical Review Letters 113(25):255501. https://doi.org/10.1103/PhysRevLett.113.255501

Manca F, Giordano S, Palla PL, Cleri F (2015) Stochastic mechanical degradation of multi-cracked fiber bundles with elastic and viscous interactions. The European Physical Journal E 38(5):44. https://doi.org/10.1140/epje/i2015-15044-1

Mandal SS (2020) Force spectroscopy on single molecules of life. ACS Omega 5(20):11271–11278. https://doi.org/10.1021/acsomega.0c00814

Manghi M, Destainville N, Palmeri J (2012) Mesoscopic models for DNA stretching under force: new results and comparison with experiments. The European Physical Journal E 35(10):110. https://doi.org/10.1140/epje/i2012-12110-2

Manini N, Mistura G, Paolicelli G, Tosatti E, Vanossi A (2017) Current trends in the physics of nanoscale friction. Advances in Physics: X 2(3):569–590. https://doi.org/10.1080/23746149.2017.1330123

Manosas M, Camunas-Soler J, Croquette V, Ritort F (2017) Single molecule high-throughput footprinting of small and large DNA ligands. Nature Communications 8(1):304. https://doi.org/10.1038/s41467-017-00379-w

Marin-Gonzalez A, Vilhena JG, Perez R, Moreno-Herrero F (2017) Understanding the mechanical response of double-stranded DNA and RNA under constant stretching forces using all-atom molecular dynamics. Proceedings of the National Academy of Sciences 114(27):7049–7054. https://doi.org/10.1073/pnas.1705642114

Marko JF, Siggia ED (1995) Bending and twisting elasticity of DNA. Macromolecules 27(4):981–988. https://doi.org/10.1021/ma00082a015

Marko JF, Cocco S (2003) The micromechanics of DNA. Physics World 16(3):37. https://doi.org/10.1088/2058-7058/16/3/40

Marmur J, Doty P (1962) Determination of the base composition of deoxyribonucleic acid from its thermal denaturation temperature. Journal of Molecular Biology 5(1):109–118. https://doi.org/10.1016/S0022-2836(62)80066-7

Marone C (1998) The effect of loading rate on static friction and the rate of fault healing during the earthquake cycle. Nature 391(6662):69–72. https://doi.org/10.1038/34157

Mathé J, Visram H, Viasnoff V, Rabin Y, Meller A (2004) Nanopore unzipping of individual DNA hairpin molecules. Biophysical Journal 87(5):3205–3212. https://doi.org/10.1529/biophysj.104.047274

Mielke A, Truskinovsky L (2012) From discrete visco-elasticity to continuum rate-independent plasticity: rigorous results. Archive for Rational Mechanics and Analysis 203(2):577–619. https://doi.org/10.1007/s00205-011-0460-9

Miracle DB, Senkov ON (2017) A critical review of high entropy alloys and related concepts. Acta Materialia 122:448–511. https://doi.org/10.1016/j.actamat.2016.08.081

Mishra G, Giri D, Li MS, Kumar S (2011) Role of loop entropy in the force induced melting of DNA hairpin. The Journal of Chemical Physics 135(3):035102. https://doi.org/10.1063/1.3609970

Mo Y, Turner KT, Szlufarska I (2009) Friction laws at the nanoscale. Nature 457(7233):1116–1119. https://doi.org/10.1038/nature07748

Müller I, Villaggio P (1977) A model for an elastic-plastic body. Archive for Rational Mechanics and Analysis 65:25–46. https://doi.org/10.1007/BF00289355

Nadkarni N, Arrieta AF, Chong C, Kochmann DM, Daraio C (2016) Unidirectional transition waves in bistable lattices. Physical Review Letters 116(24):244501. https://doi.org/10.1103/PhysRevLett.116.244501

Nemat-Nasser S, Guo WG, Cheng JY (1999) Mechanical properties and deformation mechanisms of a commercially pure titanium. Acta Materialia 47(13):3705–3720. https://doi.org/10.1016/S1359-6454(99)00203-7

Neuenschwander M, Scandella C, Knobloch M, Fontana M (2017a) Modeling elevated-temperature mechanical behavior of high and ultra-high strength steels in structural fire design. Mater Design 136:81–102. https://doi.org/10.1016/j.matdes.2017.09.041

Neuenschwander M, Knobloch M, Fontana M (2017b) Elevated temperature mechanical properties of solid section structural steel. Construction and Building Materials 149:186–201. https://doi.org/10.1016/j.conbuildmat.2017.05.124

Neuman KC, Nagy A (2008) Single-molecule force spectroscopy: optical tweezers, magnetic tweezers and atomic force microscopy. Nature Methods 5(6):491–505. https://doi.org/10.1038/nmeth.1218

Nishinari K, Koide S, Williams PA, Phillips GO (1990) A zipper model approach to the thermoreversible gel-sol transition. Journal de Physique France 51(16):1759–1768. https://doi.org/10.1051/jphys:0199000510160175900

Noh G, Benetatos P (2021) Tensile elasticity of a freely jointed chain with reversible hinges. Soft Matter 17(12):3333–3345. https://doi.org/10.1039/D1SM00053E

Nomidis SK, Kriegel F, Vanderlinden W, Lipfert J, Carlon E (2017) Twist-bend coupling and the torsional response of double-stranded DNA. Physical Review Letters 118(21):217801. https://doi.org/10.1103/PhysRevLett.118.217801

Nomidis SK, Skoruppa E, Carlon E, Marko JF (2019) Twist-bend coupling and the statistical mechanics of the twistable wormlike-chain model of DNA: perturbation theory and beyond. Physical Review E 99(3):032414. https://doi.org/10.1103/PhysRevE.99.032414

Oberhauser AF, Marszalek PE, Erickson HP, Fernandez JM (1998) The molecular elasticity of the extracellular matrix protein tenascin. Nature 393(6681):181–185. https://doi.org/10.1038/30270

Otto F, Dlouhý A, Somsen Ch, Bei H, Eggeler G, George EP (2013) The influences of temperature and microstructure on the tensile properties of a CoCrFeMnNi high-entropy alloy. Acta Materialia 61(15):5743–5755. https://doi.org/10.1016/j.actamat.2013.06.018

Palmeri J, Manghi M, Destainville N (2008) Thermal denaturation of fluctuating finite DNA chains: the role of bending rigidity in bubble nucleation. Physical Review E 77(1):011913. https://doi.org/10.1103/PhysRevE.77.011913

Perret G, Lacornerie T, Manca F, Giordano S, Kumemura M, Lafitte N, Jalabert L, Tarhan MC, Lartigau EF, Cleri F, Fujita H, Collard D (2016) Real-time mechanical characterization of DNA degradation under therapeutic X-rays and its theoretical modeling. Microsystems & Nanoengineering 2(1):1–9. https://doi.org/10.1038/micronano.2016.62

Perret G, Lacornerie T, Manca F, Giordano S, Kumemura M, Lafitte N, Jalabert L, Tarhan MC, Lartigau EF, Cleri F, Fujita H, Collard D (2017) Mesure de la dégradation bio-mécanique d'une fibre d'ADN sous l'effet des rayons X thérapeutiques. Medical Sciences (Paris) 33(12):1026–1029. https://doi.org/10.1051/medsci/20173312003

Peyrard M, Bishop AR (1989) Statistical mechanics of a nonlinear model for DNA denaturation. Physical Review Letters 62(23):2755–2758. https://doi.org/10.1103/PhysRevLett.62.2755

Peyrard M (2004) Nonlinear dynamics and statistical physics of DNA. Nonlinearity 17(2):R1. https://doi.org/10.1088/0951-7715/17/2/R01

Polya G (1913) Berechnung eines bestimmten Integrals. Mathematische Annalen 74(2):204–212. https://doi.org/10.1007/BF01456040

Popov VL (2010) Contact mechanics and friction: physical principles and applications. Springer, Berlin, Heidelberg

Prados A, Carpio A, Bonilla LL (2013) Sawtooth patterns in force-extension curves of biomolecules: an equilibrium-statistical-mechanics theory. Physical Review E 88(1):012704. https://doi.org/10.1103/PhysRevE.88.012704

Puglisi G (2006) Hysteresis in multi-stable lattices with non-local interactions. Journal of the Mechanics and Physics of Solids 54(10):2060–2088. https://doi.org/10.1016/j.jmps.2006.04.006

Puglisi G, Truskinovsky L (2005) Thermodynamics of rate-independent plasticity. Journal of the Mechanics and Physics of Solids 53(3):655–679. https://doi.org/10.1016/j.jmps.2004.08.004

Puglisi G, Truskinovsky L (2013) Cohesion-decohesion asymmetry in geckos. Physical Review E 87(3):032714. https://doi.org/10.1103/PhysRevE.87.032714

Punkkinen O, Hansen PL, Miao L, Vattulainen I (2005) DNA overstretching transition: ionic strength effects. Biophysical Journal 89(2):967–978. https://doi.org/10.1529/biophysj.105.063099

Pupo AEB, Falo F, Fiasconaro A (2013) DNA overstretching transition induced by melting in a dynamical mesoscopic model. The Journal of Chemical Physics 139(9):095101. https://doi.org/10.1063/1.4819263

Qian J, Lin J, Xu G-K, Lin Y, Gao H (2017) Thermally assisted peeling of an elastic strip in adhesion with a substrate via molecular bonds. Journal of the Mechanics and Physics of Solids 101:197–208. https://doi.org/10.1016/j.jmps.2017.01.007

Radiom M, Borkovec M (2017) Influence of ligand-receptor interactions on force-extension behavior within the freely jointed chain model. Physical Review E 96(6):062501. https://doi.org/10.1103/PhysRevE.96.062501

Rafsanjani A, Akbarzadeh A, Pasini D (2015) Snapping mechanical metamaterials under tension. Advanced Materials 27(39):5931–5935. https://doi.org/10.1002/adma.201502809

Rai-Choudhury P (2000) MEMS and MOEMS technology and applications. SPIE Press, Bellingham, Washington

Rayleigh Lord (1919) XXXI. On the problem of random vibrations, and of random flights in one, two, or three dimensions. The London, Edinburgh and Dublin Philosophical Magazine and Journal of Science 37(220):321–347. https://doi.org/10.1080/14786440408635894

Ren F, Zu Y, Kumar Rajagopalan K, Wang S (2012) Regulation of DNA conformations and dynamics in flows with hybrid field microfluidics. Biomicrofluidics 6(4):044103. https://doi.org/10.1063/1.4762852

Rico F, Gonzalez L, Casuso I, Puig-Vidal M, Scheuring S (2013) High-speed force spectroscopy unfolds titin at the velocity of molecular dynamics simulations. Science 342(6159):741–743. https://doi.org/10.1126/science.1239764

Rico F, Russek A, González L, Grubmüller H, Scheuring S (2019) Heterogeneous and rate-dependent streptavidin–biotin unbinding revealed by high-speed force spectroscopy and atomistic simulations. Proceedings of the National Academy of Sciences 116(14):6594–6601. https://doi.org/10.1073/pnas.1816909116

Rief M, Oesterhelt F, Heymann B, Gaub HE (1997a) Single molecule force spectroscopy on polysaccharides by atomic force microscopy. Science 275(5304):1295–1297. https://doi.org/10.1126/science.275.5304.1295

Rief M, Gautel M, Oesterhelt F, Fernandez JM, Gaub HE (1997b) Reversible unfolding of individual titin immunoglobulin domains by AFM. Science 276(5315):1109–1112. https://doi.org/10.1126/science.276.5315.1109

Rief M, Fernandez JM, Gaub HE (1998) Elastically coupled two-level systems as a model for biopolymer extensibility. Physical Review Letters 81(21):4764–4767. https://doi.org/10.1103/PhysRevLett.81.4764

Rief M, Pascual J, Saraste M, Gaub HE (1999) Single molecule force spectroscopy of spectrin repeats: low unfolding forces in helix bundles11Edited by W. Baumeister. Journal of Molecular Biology 286(2):553–561. https://doi.org/10.1006/jmbi.1998.2466

Ritort F (2006) Single-molecule experiments in biological physics: methods and applications. Journal of Physics: Condensed Matter 18(32):R531. https://doi.org/10.1088/0953-8984/18/32/R01

Rouzina I, Bloomfield VA (2001a) Force-induced melting of the DNA double helix. 2. Effect of solution conditions. Biophysical Journal 80(2):894–900. https://doi.org/10.1016/S0006-3495(01)76068-7

Rouzina I, Bloomfield VA (2001b) Force-induced melting of the DNA double helix 1. Thermodynamic analysis. Biophysical Journal 80(2):882–893. https://doi.org/10.1016/S0006-3495(01)76067-5

Sahli R, Pallares G, Ducottet C, Ben Ali IE, Al Akhrass S, Guibert M, Scheibert J (2018) Evolution of real contact area under shear and the value of static friction of soft materials. Proceedings of the National Academy of Sciences 115(3):471–476. https://doi.org/10.1073/pnas.1706434115

Scholz CH (1998) Earthquakes and friction laws. Nature 391(6662):37–42. https://doi.org/10.1038/34097

Schwarz US, Safran SA (2013) Physics of adherent cells. Reviews of Modern Physics 85(3):1327–1381. https://doi.org/10.1103/RevModPhys.85.1327

Sens P (2020) Stick–slip model for actin-driven cell protrusions, cell polarization, and crawling. Proceedings of the National Academy of Sciences 117(40):24670–24678. https://doi.org/10.1073/pnas.2011785117

Shaw JA, Kyriakides S (1997) On the nucleation and propagation of phase transformation fronts in a NiTi alloy. Acta Materialia 45(2):683–700. https://doi.org/10.1016/S1359-6454(96)00189-9

Skvortsov AM, Klushin LI, Leermakers F a. M (2007) Negative compressibility and nonequivalence of two statistical ensembles in the escape transition of a polymer chain. The Journal of Chemical Physics 126(2):024905. https://doi.org/10.1063/1.2406075

Skvortsov AM, Klushin LI, Polotsky AA, Binder K (2012) Mechanical desorption of a single chain: unusual aspects of phase coexistence at a first-order transition. Physical Review E 85(3):031803. https://doi.org/10.1103/PhysRevE.85.031803

Smith SB, Finzi L, Bustamante C (1992) Direct mechanical measurements of the elasticity of single DNA molecules by using magnetic beads. Science 258(5085):1122–1126. https://doi.org/10.1126/science.1439819

Smith SB, Cui Y, Bustamante C (1996) Overstretching B-DNA: the elastic response of individual double-stranded and single-stranded DNA molecules. Science 271(5250):795–799. https://doi.org/10.1126/science.271.5250.795

Song Z (2020) Analytical study on phase transition of shape memory alloy wire under uniaxial tension. International Journal of Engineering Science 152:103295. https://doi.org/10.1016/j.ijengsci.2020.103295

Stephenson W, Keller S, Santiago R, Albrecht JE, Asare-Okai PN, Tenenbaum SA, Zuker M, Li PTX (2014) Combining temperature and force to study folding of an RNA hairpin. Physical Chemistry Chemical Physics 16(3):906–917. https://doi.org/10.1039/C3CP52042K

Storm C, Nelson PC (2003) Theory of high-force DNA stretching and overstretching. Physical Review E 67(5):051906. https://doi.org/10.1103/PhysRevE.67.051906

Strick TR, Allemand JF, Bensimon D, Bensimon A, Croquette V (1996) The elasticity of a single supercoiled DNA molecule. Science 271(5257):1835–1837. https://doi.org/10.1126/science.271.5257.1835

Strick TR, Dessinges M-N, Charvin G, Dekker NH, Allemand J-F, Bensimon D, Croquette V (2002) Stretching of macromolecules and proteins. Reports on Progress in Physics 66(1):1. https://doi.org/10.1088/0034-4885/66/1/201

Szlufarska I, Chandross M, Carpick RW (2008) Recent advances in single-asperity nanotribology. Journal of Physics D: Applied Physics 41(12):123001. https://doi.org/10.1088/0022-3727/41/12/123001

Tarhan MC, Lafitte N, Tauran Y, Jalabert L, Kumemura M, Perret G, Kim B, Coleman AW, Fujita H, Collard D (2016) A rapid and practical technique for real-time monitoring of biomolecular interactions using mechanical responses of macromolecules. Scientific Reports 6(1):28001. https://doi.org/10.1038/srep28001

Ternes M, Lutz CP, Hirjibehedin CF, Giessibl FJ, Heinrich AJ (2008) The force needed to move an atom on a surface. Science 319(5866):1066–1069. https://doi.org/10.1126/science.1150288

Theodorakopoulos N, Peyrard M, MacKay RS (2004) Nonlinear structures and thermodynamic instabilities in a one-dimensional lattice system. Physical Review Letters 93(25):258101. https://doi.org/10.1103/PhysRevLett.93.258101

Treloar LRG (1946) The statistical length of long-chain molecules. Transactions of the Faraday Society 42(0):77–82. https://doi.org/10.1039/TF9464200077

Truskinovsky L, Vainchtein A (2004) The origin of nucleation peak in transformational plasticity. Journal of the Mechanics and Physics of Solids 52(6):1421–1446. https://doi.org/10.1016/j.jmps.2003.09.034

Truskinovsky L, Zanzotto G (1996) Ericksen's bar revisited: energy wiggles. Journal of the Mechanics and Physics of Solids 44(8)1371–1408. https://doi.org/10.1016/0022-5096(96)00020-8

Urbakh M, Klafter J, Gourdon D, Israelachvili J (2004) The nonlinear nature of friction. Nature 430(6999):525–528. https://doi.org/10.1038/nature02750

Vakis AI, Yastrebov VA, Scheibert J, Nicola L, Dini D, Minfray C, Almqvist A, Paggi M, Lee S, Limbert G, Molinari JF, Anciaux G, Aghababaei R, Echeverri Restrepo S, Papangelo A, Cammarata A, Nicolini P, Putignano C, Carbone G, Stupkiewicz S, Lengiewicz J, Costagliola G, Bosia F, Guarino R, Pugno NM, Müser MH, Ciavarella M (2018) Modeling and simulation in tribology across scales: an overview. Tribology International 125:169–199. https://doi.org/10.1016/j.triboint.2018.02.005

Valberg PA, Albertini DF (1985) Cytoplasmic motions, rheology, and structure probed by a novel magnetic particle method. Journal of Cell Biology 101(1):130–140. https://doi.org/10.1083/jcb.101.1.130

Valberg PA, Feldman HA (1987) Magnetic particle motions within living cells. Measurement of cytoplasmic viscosity and motile activity. Biophysical Journal 52(4):551–561. https://doi.org/10.1016/S0006-3495(87)83244-7

Valotteau C, Sumbul F, Rico F (2019) High-speed force spectroscopy: microsecond force measurements using ultrashort cantilevers. Biophysical Reviews 11(5):689–699. https://doi.org/10.1007/s12551-019-00585-4

Vanossi A, Manini N, Urbakh M, Zapperi S, Tosatti E (2013) Colloquium: modeling friction: from nanoscale to mesoscale. Reviews of Modern Physics 85(2):529–552. https://doi.org/10.1103/RevModPhys.85.529

Wallace RB, Shaffer J, Murphy RF, Bonner J, Hirose T, Itakura K (1979) Hybridization of synthetic oligodeoxyribonucleotides to phi chi 174 DNA: the effect of single base pair mismatch. Nucleic Acids Research 6(11):3543–3557. https://doi.org/10.1093/nar/6.11.3543

Walther KA, Brujić J, Li H, Fernández JM (2006) Sub-angstrom conformational changes of a single molecule captured by AFM variance analysis. Biophysical Journal 90(10):3806–3812. https://doi.org/10.1529/biophysj.105.076224

Wang J, Kouznetsova TB, Boulatov R, Craig SL (2016) Mechanical gating of a mechanochemical reaction cascade. Nature Communications 7(1):13433. https://doi.org/10.1038/ncomms13433

Wang MC, Guth E (1952) Statistical theory of networks of non-gaussian flexible chains. The Journal of Chemical Physics 20(7):1144–1157. https://doi.org/10.1063/1.1700682

Wang X, Lim HJ, Son A (2014) Characterization of denaturation and renaturation of DNA for DNA hybridization. Environmental Health and Toxicology 29:e2014007. https://doi.org/10.5620/eht.2014.29.e2014007

Watson JD, Crick FHC (1953) Molecular structure of nucleic acids: a structure for deoxyribose nucleic acid. Nature 171(4356):737–738. https://doi.org/10.1038/171737a0

Weiner JH (2002) Statistical mechanics of elasticity. Dover Publications, New York

Wenner JR, Williams MC, Rouzina I, Bloomfield VA (2002) Salt dependence of the elasticity and overstretching transition of single DNA molecules. Biophysical Journal 82(6):3160–3169. https://doi.org/10.1016/S0006-3495(02)75658-0

Winkler RG (2010) Equivalence of statistical ensembles in stretching single flexible polymers. Soft Matter 6(24):6183–6191. https://doi.org/10.1039/C0SM00488J

Woodside MT, García-García C, Block SM (2008) Folding and unfolding single RNA molecules under tension. Current Opinion in Chemical Biology 12(6):640–646. https://doi.org/10.1016/j.cbpa.2008.08.011

Xia S, Ponson L, Ravichandran G, Bhattacharya K (2012) Toughening and asymmetry in peeling of heterogeneous adhesives. Physical Review Letters 108(19):196101. https://doi.org/10.1103/PhysRevLett.108.196101

Yamahata C, Collard D, Legrand B, Takekawa T, Kumemura M, Hashiguchi G, Fujita H (2008) Silicon nanotweezers with subnanometer resolution for the micromanipulation of biomolecules. Journal of Microelectromechanical Systems 17(3):623–631. https://doi.org/10.1109/JMEMS.2008.922080

Yang P-Y, Ju S-P, Lai Z-M, Hsieh J-Y, Lin J-S (2016) The mechanical properties and thermal stability of ultrathin germanium nanowires. RSC Advances 6(107):105713–105722. https://doi.org/10.1039/C6RA21841E

Zaltron A, Merano M, Mistura G, Sada C, Seno F (2020) Optical tweezers in single-molecule experiments. The European Physical Journal Plus 135(11):896. https://doi.org/10.1140/epjp/s13360-020-00907-6